Civil and Environmental Theses   Civil and Environmental Engineering

11-2019

Strengthening of Concrete Deep Beams with Extreme Discontinuities Using Near-Surface mounted Composites

Moustafa Seifeddin Mansour

Recommended Citation
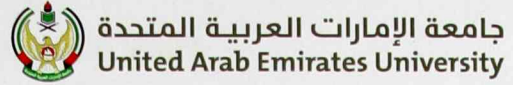
United Arab Emirates University

College of Engineering

Department of Civil and Environmental Engineering

STRENGTHENING OF CONCRETE DEEP BEAMS WITH EXTREME DISCONTINUITIES USING NEAR-SURFACE-MOUNTED COMPOSITES

Moustafa Seifeddin Mansour

This thesis is submitted in partial fulfilment of the requirements for the degree of Master of Science in Civil Engineering

Under the Supervision of Professor Tamer El Maaddawy

November 2019

Declaration of Original Work

I, Moustafa Seifeddin Mansour, the undersigned, a graduate student at the United Arab Emirates University (UAEU), and the author of this thesis entitled *"Strengthening of Concrete Deep Beams with Extreme Discontinuities Using Near-Surface-Mounted Composites"*, hereby, solemnly declare that this thesis is my own original research work that has been done and prepared by me under the supervision of Professor Tamer El Maaddawy, in the College of Engineering at UAEU. This work has not previously been presented or published, or formed the basis for the award of any academic degree, diploma or a similar title at this or any other university. Any materials borrowed from other sources (whether published or unpublished) and relied upon or included in my thesis have been properly cited and acknowledged in accordance with appropriate academic conventions. I further declare that there is no potential conflict of interest with respect to the research, data collection, authorship, presentation and/or publication of this thesis.

Student's Signature: _____   Date: 22/12/2019

Approval of the Master Thesis

This Master Thesis is approved by the following Examining Committee Members:

1) Advisor (Committee Chair): Tamer A. El Maaddawy

   Title: Professor

   Department of Civil and Environmental Engineering

   College of Engineering

   Signature _____   Date 22/12/2019

2) Member: Bilal El-Ariss

   Title: Associate Professor

   Department of Civil and Environmental Engineering

   College of Engineering

   Signature _____   Date DECEMBER 22, 2019

3) Member (External Examiner): Abdeldjelil "DJ" Belarbi

   Title: Professor

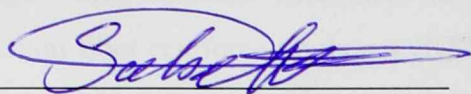   Department of Civil and Environmental Engineering

   Institution: University of Houston, USA

   FOR
   Signature _____   Date DECEMBER 22, 2019

This Master Thesis is accepted by:

Dean of the College of Engineering: Professor Sabah Alkass
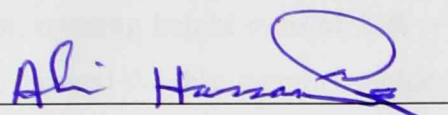
Signature _____ Date _22/12/2019_

Dean of the College of Graduate Studies: Professor Ali Al-Marzouqi

Signature __Ali Hassan__ Date _23/12/2019_

Copy _4_ of _4_

Abstract

Installation of a web opening that fully interrupts the natural load path in concrete deep beams produces regions of extreme discontinuities and reduces the shear strength. This research examined the effectiveness of using near-surface-mounted carbon fiber-reinforced polymer (NSM-CFRP) reinforcement to restore the shear strength of deep beams with extreme discontinuities. The strut-and-tie model (STM) procedures were utilized to develop three different strengthening solutions around the discontinuity regions. A total of eight deep beam specimens (150 x 500 x 2700 mm) with a shear span-to-depth ratio of $a/h = 0.8$ were constructed and tested. One beam was solid. Seven beams had a square opening in the middle of the shear span with an opening height ratio of $h_o/h = 0.2$. Six beams were strengthened with NSM-CFRP around the discontinuity regions. Three-dimensional finite element (FE) models were developed to simulate the nonlinear behavior of the tested specimens. Experimental results were compared to predictions of the FE models and the STM design solutions to examine their accuracy and validity. Installation of the web opening resulted in a 40% reduction in the shear strength. The NSM-CFRP strengthening solutions fully restored the original shear strength, except in two cases where only 93% and 94% of the capacity were restored. The laboratory test results were used to determine the optimal NSM-CFRP strengthening solution. The STM based on provisions of the American Concrete Institute provided realistic and consistent predictions for the nominal strength of the tested specimens with an average predicted-to-measured strength ratio of 1.01±0.09. In contrast, the STM predictions based on provisions of the Canadian Standards Association tended to be conservative with an average predicted-to-measured strength ratio of 0.71±0.29. Predictions of the FE models were sensitive to the mesh size and the concrete constitutive law adopted in the analysis. The inclusion of a bond-slip model between the CFRP and concrete resulted in up to a 5% reduction in the predicted strength. The use of a small mesh size of 15 mm and a "user" concrete constitutive law rather than a "default" law yielded more accurate predictions that were insignificantly different from those obtained from the tests.

Keywords: Deep beams, discontinuity, experimental, NSM-CFRP, numerical, simulation, STM, strengthening.

Title and Abstract (in Arabic)

تقوية الجسور الخرسانية العميقة التي تحتوي على انقطاعات قصوى باستخدام المواد المركبات المثبتة في ممرات قريبة من سطح الخرسانة

الملخص

إن شق فتحات تقطع مسار الحمل الطبيعي بشكل كلي في الجسور الخرسانية العميقة يؤدي إلى تكوين مناطق انقطاعات قصوى وانخفاض قوة القص. يتناول هذا البحث فعالية استخدام المواد المركبات المثبتة في ممرات قريبة من سطح الخرسانة لاستعادة قوة التحمل في الجسور العميقة ذات الانقطاعات القصوى. تم استخدام نظرية الشد والضغط (strut-and-tie model) لتطوير ثلاث تصاميم للتقوية حول مناطق الانقطاعات. تم انشاء واختبار ثماني عينات من الجسور العميقة (2700 x 500 x 150 مم) مع نسبة مسافة القص-الى-العمق تساوي 0.8. واحد من الجسور كان صلبا. اما سبعة من الجسور احتوت على فتحات في منتصف مسافة القص مع نسبة ارتفاع للفتحة تساوي 0.2 من عمق الجسر. ستة من الجسور تم تقويتها بواسطة المواد المركبات المثبتة في ممرات قريبة من سطح الخرسانة متموضعة حول الانقطاعات القصوى. تم تطوير نماذج العناصر المحدودة ثلاثي الأبعاد لمحاكاة السلوك الغير خطي للعينات. تم مقارنة نتائج الاختبارات المعملية مع تنبؤات نماذج العناصر المحدودة ونماذج نظرية الشد والضغط (strut-and-tie model) لاختبار مدى دقة وصلاحية هذه التنبؤات. إن وجود الفتحات أدى الى خفض قوة القص في الجسور بنسبة 40%. نجحت طريقة التقوية في استعادة قوة القص كاملة باستثناء حالتين، حيث تم استعادة 93% و94% فقط من قوة القص. استخدمت نتائج الاختبارات المعملية في تحديد أمثل حل تقوية باستخدام المواد المركبات المثبتة في ممرات قريبة من سطح الخرسانة. التنبؤات الناتجة عن نظرية الشد والضغط (-strut and-tie model) باستخدام الأحكام الأمريكية كانت واقعية ومتناسقة حيث كان متوسط نسبة القوة المتوقعة-إلى-المقاسة يساوي 1.01±0.09. في المقابل، كانت التنبؤات الناتجة عن نظرية الشد والضغط (strut-and-tie model) باستخدام الأحكام الكندية محافظة وكان متوسط نسبة القوة المتوقعة-إلى-المقاسة يساوي 0.71±0.29. أما تنبؤات نماذج العناصر المحدودة كانت حساسة لحجم الشبكة والقانون التأسيسي للخرسانة المستخدمان. تضمين نموذج الربط -الانزلاق(-bond slip model) بين المواد المركبات والخرسانة إلى خفض القوة المتنبئة بنسبة تصل الى 5%. استخدام حجم شبكة صغيرة بمقدار 15 مم وقانون التأسيسي للخرسانة "user" عوضا عن

قانون "default" إلى التوصل لتنبؤات أدق، حيث كانت التنبؤات مختلفة بشكل ضئيل عن نتائج الاختبارات.

مفاهيم البحث الرئيسية: جسور عميقة، انقطاعات، تجارب، المواد المركبات المثبتة في ممرات قريبة من سطح الخرسانة، نمذجة عددية، محاكاة، نظرية الشد والضغط، تقوية.

Acknowledgements

Dedication

To my beloved parents, wife, sisters, and daughters

Table of Contents

List of Tables

List of Figures

List of Abbreviations

ACI	American Concrete Institute
CFRP	Carbon Fiber-Reinforced Polymer
CSA	Canadian Standards Association
D-region	Disturbed Region
EB	Externally-Bonded
FE	Finite Element
FRP	Fiber-Reinforced Polymer
NSM	Near-Surface-Mounted
OPC	Ordinary Portland Cement
RC	Reinforced Concrete
STM	Strut-and-Tie Model
a_b	Smallest Cross-Sectional Dimension of CFRP Strip
A_{cs}	Cross-Sectional Area of the Strut
a/d	Shear Span-to-Effective Depth Ratio
A_{FRP}	Cross-Sectional Area of CFRP Strip
$A_{f,tie}$	Area of CFRP Per Tie
a/h	Shear Span-to-Depth Ratio
A_{nz}	Area of Nodal Zone
b_b	Larger Cross-Sectional Dimension of CFRP Strip
C_E	Environmental Reduction Factor
E_c	Concrete Modulus of Elasticity
EF	Efficiency Factor
E_f	Young's Modulus of CFRP

E_s	Young's Modulus of Steel
f'_c	Cylinder Compressive Strength of Concrete
f_{ct}	Concrete Splitting Strength
f_{cu}	Cube Compressive Strength of Concrete
f_{fe}	Effective Strength of the CFRP
f_{fu}	Ultimate Strength of CFRP
F_i	Internal Force of the Truss Element
F_{ni}	Nominal Strength of the Truss Element
F_{nn}	Nominal Strength of the Node
F_{ns}	Nominal Strength of a Concrete Strut
F_{nt}	Nominal Tensile Strengths of Tie
F_r	Resultant Force on a Node Face
F_t	Design Capacity of Tie
f'_t	Uniaxial Concrete Tensile Strength
f_y	Yield Strength of Steel
h_o/h	Opening Height-to-Beam Depth Ratio
L_{ch}	Characteristic Length
l_c/h	Clear Span-to- Depth Ratio
P_{ACI}	Predicted Load Capacity by ACI 318-14 Provisions
P_{cr}	Cracking Load
P_{CSA}	Predicted Load Capacity by CSA S806 Provisions
P_{Exp}	Experimental Load Capcity
P_{FE}	Predicted Load Capacity by Numerical Model
P_{max}	Ultimate Load
w_n	Width of a Node Face

w_s	Width of Strut
β_n	Nodal Zone Coefficient
β_s	Strut Coefficient
ε_1	Calculated Transverse Tensile Strain in a Cracked Strut
ε_f	Tensile Strain in an Adjoining Tie to the Strut
ε_{fu}	CFRP Ultimate Strain
θ_s	Angle between the Strut and the Adjoining Tie
Δ_{cr}	Midspan Deflection at the Onset of Cracking
Δ_{Exp}	Experimental Midspan Deflection at Failure
Δ_{FE}	Numerical Midspan Deflection at Failure
Δ_{peak}	Midspan Deflection at the Peak Load

Chapter 1: Introduction

1.1 Background

Reinforced Concrete (RC) Deep beams are structural members that are utilized to carry and transfer loads in the structural system. The geometric property of the deep beams is the main criterion to define this type of beams. Deep beams are characterized by their large depth compared to the longitudinal span. As per ACI 318-14 [1], a beam is considered deep beam if it satisfies one of the following conditions: (1) clear span-to-depth ratio (l_c/h) $\leq$ 4, (2) shear span-to-depth ratio (a/h) $\leq$ 2. Figure 1.1 shows an example of a deep beam. The short shear span or clear span makes the deep beams effective in carrying and transferring heavy loads over very long spans, whereas conventional slender beam cannot serve this purpose. Deep beams are generally used as pile caps, folded plates, foundation walls, raft beams, walls of rectangular tanks, hoppers, floor diaphragms and squat walls [2,3]. The load carrying capacity of deep beams is dominant by the shear capacity of the beams. The transfer of the load in deep beams from the loading point to the support in a short shear span develops a strut-like compression element which makes the region critical. The deep beams usually fail in shear, unlike slender beams which fail in flexure at midspan caused by bending moment. The beam theory or Bernoulli theory which considers a linear distribution of stress and strain over the cross section of the beam is not applicable in deep beams. B-region refers to a region where beam theory can be applied. On the other hand, the shear span in the deep beams is referred to disturbed regions (D-regions) where strain distribution is significantly nonlinear [4]. Hence, conventional design methodologies for regular beams are not valid for deep beams.
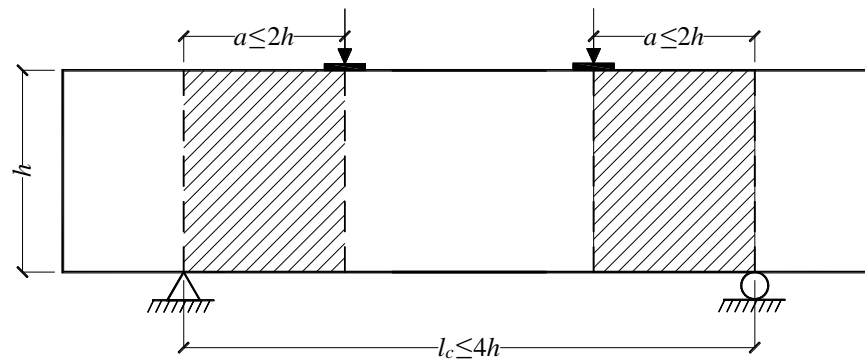
Figure 1.1: Deep beam with D-regions (shaded areas)

The strut-and-tie model (STM) is preferred as a design methodology in D-regions. The STM has been emerged as a code worthy methodology for the design of D-regions such as deep beams in concrete structures [1,5]. The STM is based on the lower-bound theory of plasticity which means that the capacity of the model is always less than the true capacity. In STM, the internal stresses are assumed to transfer through the truss that is developed by the designer. The truss is composed of struts which are compression members and ties which are tension members. These struts and ties represent the internal forces in the structure. The STM is used to determine the amount and distribution of reinforcement in D-regions. Usually, reinforcements in concrete are placed in ties' locations.

Transverse web openings are unavoidable in many cases because they are typically needed to provide accessibility and/or to accommodate essential services such as ventilation and air conditioning ducts. The presence of openings in deep beams results in an extreme geometrical discontinuity that interrupts the natural load path. Installation of web openings in existing concrete deep beams after construction is frequently encountered on practical settings to accommodate changes in

architectural design. In such cases, adequate measures shall be undertaken to strengthen the concerned D-regions and restore the beam capacity.

Fiber-reinforced polymer (FRP) composites are favorable to be used in such cases for external strengthening to its effectiveness in strengthening and corrosion resistance. Externally-bonded (EB) FRP is a commonly used technique to utilize FRP composites in strengthening concrete beams. However, the contribution of EB-FRP in strengthening is sometimes limited to premature debonding [6–9]. Post-installed near-surface-mounted (NSM) composite reinforcement offers opportunities to prevent the FRP debonding mode of failure, and hence, improve the behavior of concrete deep beams with extreme discontinuities. NSM system was found to be more efficient in enhancing the beams' behavior in terms of load and deformation capacities [10]. Nevertheless, the efficiency of NSM composite reinforcement in strengthening RC deep beams with openings has received little attention in previous studies.

1.2 Scope and Objectives

Although strengthening of deep beams with extreme discontinuities are typically encountered in practical settings, no design equations are currently available in conventional codes of practice to solve such a complex problem. This research aims to fill this gap through experimental testing, strut-and-tie modeling, and numerical simulation. The specific objectives are listed below.

- Develop strut-and-tie models to design different NSM-CFRP strengthening solutions of deep beams with extreme discontinuities.

- Conduct laboratory testing to examine the effectiveness of using different NSM-CFRP strengthening solutions to improve the shear resistance of concrete deep beams with extreme discontinuities.

- Examine the accuracy and validity of the STM to predict the load capacity of deep beams strengthened with NSM-CFRP reinforcement around regions of discontinuity.

- Develop numerical simulation models capable of predicting the nonlinear behavior of concrete deep beams strengthened with NSM-CFRP reinforcement around discontinuity regions.

1.3 Thesis Organization

In Chapter 1, a brief overview of the research topic is presented including the characteristics and applications of deep beams, strut-and-tie model as a design method, and proposed strengthening method for deep beams with extreme discontinuity. In addition, the research scope and objectives are presented.

Chapter 2 presents a summary of the reviewed literature related to this research. The chapter summarizes the findings of previous research on the behavior of RC deep beams with openings, the strengthening techniques of RC beams with openings, strut-and-tie model design, and finite element modeling. Research significance is stated at the end of the chapter.

The provisions of ACI 318-14 [1] and CSA S806 [5] for STM are reviewed in Chapter 3. Furthermore, details of the developed of strut-and-tie models are presented.

Chapter 4 shows the details of the experimental program including test matrix, details of specimens, fabrication of specimens, test setup and

instrumentations. Additionally, detailed descriptions of materials properties and strengthening technique are provided.

The experimental results of testing deep beam specimens are presented in Chapter 5. The load-deflection response, failure mode, and strain measurements are reported in this chapter.

Chapter 6 shows STMs predictions of load capacity of the tested specimens. Besides, a comparative analysis is reported.

In Chapter 7, the development of numerical models for the specimens using ATENA 3D is illustrated. Comparative analysis between the numerical and experimental results is presented at the end of the chapter.

A summary of the current research work, limitations, general conclusions, and recommendations for future studies are delivered in Chapter 8.

Chapter 2: Literature Review

2.1 Introduction

This chapter reports a summary of the findings from previous research that are relevant to the thesis topic including: behavior of RC deep beams with openings, external strengthening of RC deep beams and RC slender beams with openings, strut-and-tie model design, and numerical finite element modeling. At the end of this chapter, the significance of this research work is pointed out.

2.2 Characteristics of Deep Beams

Deep beams are used in concrete structures as shear walls, transfer girders, pile caps, or wall footings. A deep beam is defined as its clear span-to-depth ratio $(l_c/h) \leq 4$ and/or shear span-to-depth ratio $(a/h) \leq 2$ [1]. If these conditions are met, then the shear spans of the beam are short and deep. Deep beams are characterized by the nonlinear distribution of longitudinal strain over the depth of the beam, while in regular concrete beams the strain changes linearly throughout the depth [1]. The complexity of stress flow in deep beams generates D-regions, which is a unique feature. Thus, D-regions require special considerations for analysis and design.

2.2.1 The Behavior of RC Beams with Openings

The inclusion of a web opening in a structural RC beam causes an extreme discontinuity in the beam cross-section and generates consequences that lead to a deviation from the original behavior of the beam. The discontinuity concentrates stresses around the opening, which initiates transverse cracks in the beam's web.

This changes the beam's behavior through a reduction in load carrying capacity and stiffness, as reported by previous studies.

Mansur et al. [11] investigated the effect of circular web openings in RC T-beam and how the behavior changed by varying size and location of the openings. The load-deflection curve for beams with openings had a similar linear elastic response to solid beam, until the formation of cracks. Flexural cracks formed first, then were followed by the appearance of diagonal cracks at the opening's edge. Diagonal cracks continued to propagate as the load increased, until one crack widened excessively, and the beam failed. Concrete crushing was noticed at the tip of major diagonal cracks. It was reported that the chords below and above the opening did not carry equal stresses. The bottom chord experienced more shear force. The author concluded that strength reduction in the beam increases as the opening size increases and opening's location approach the support.

Mansur et al. [12] classified the opening's size to small or large according to the structural response of the beam with the existence of the openings. The author used the term small is used when usual beam theory is applicable and beam type behavior is maintained. On the other hand, deviation from the mentioned conditions caused by the opening classifies the opening as a large opening.

Abdalla et al. [13] reported that the load capacity of beams has sharply decreased due to the existence of an opening in the shear zone. The studied beams suffered from wide cracks at the opening's zone along with flexural crack at the midspan. Furthermore, the findings pointed out that the height of rectangular opening had more influence on beams' capacity than the width. Changing the opening's height-to-beam's depth ratio from 0.4 to 0.6 provided a lower shear strength by 25%.

While increasing the opening width and keeping the height constant resulted in minor changes in beam load capacity. The author summarized the formed cracks in the shear zone for RC beam with opening as shown in Figure 2.1 and categorized them as follow:

1. Cracks generated at opening's corners near the loading point and support by framing action of opening's chords.
2. Cracks in the chords formed by flexural stresses caused by the secondary moments in the chords.
3. Cracks in the bottom (tension) chord caused by normal tensile stresses.
4. Diagonal cracks in the chords generated by shear stresses. This type of cracking pattern can prompt complete failure of the beam.
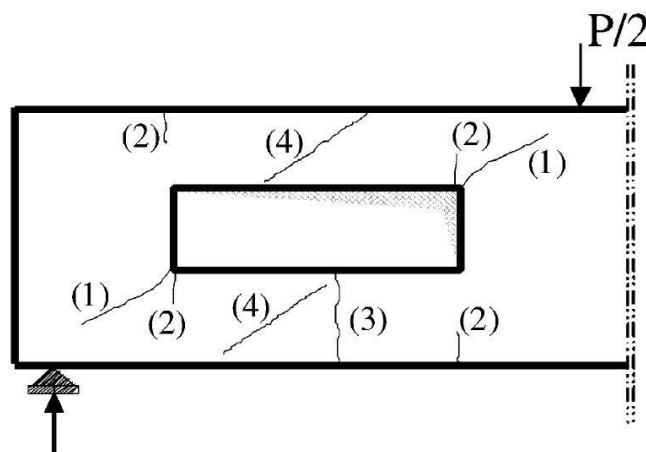
Figure 2.1: Crack patterns around the opening [13]

Kong [14] has related the behavior of RC deep beam with web opening to the following factors:

- Beam span-to-depth ratio
- Beam cross-sectional properties (i.e. rectangular section, Tee-section)
- Amount and location of main longitudinal reinforcement
- Amount, type, and location of web reinforcement
- Properties of concrete and reinforcements

- Shear span-to-depth ratio (*a/h*)
- Type and position of loading
- Size, shape, and location of web opening

Even though the author reported that the deep beam exhibited elastic behavior until the initiation of cracks, the strain varied non-linearly throughout the cross-section. In case of rectangular opening, the first noticeable diagonal cracks were observed at 36% to 55% of the ultimate load. The cracks developed at the support bearing region and opening corners. In case of circular opening, the cracks appeared at a similar range of loading. The cracks initiated in two scenarios: cracks initiated from the bottom-most point of the opening and propagated toward the support, or initiated in the middle of shear zone and moved tangentially to the opening toward the loading point or support. The author recommended circular web opening upon rectangular web opening because the load transition and diagonal cracks are well-defined in case of circular opening. Locating the center of the opening in the middle of the shear zone created the most crucial influence. Avoiding the interruption of load path by the openings, can minimize the negative influence of the openings. For instance, a beam with an opening could be considered as a solid beam if the opening is located outside the shear zone.

Yang et al. [15] studied the influence of web opening and concrete strength on RC deep beams behavior. The studied parameters were: concrete strength, *a/h* ratio and opening size. The experimental program consisted of testing 32 beams by four-point bending. Shear reinforcement was not added in the shear span. The concrete grades were 24, 50, and 80 MPa. Shear span-to-depth ratios (*a/h*) were 0.5, 0.7, 1 and 1.5. Rectangular openings were located at the center of shear spans. The opening's width was chosen as ratio of shear span length (a) (0.25*a*, 0.5*a*, and 0.65*a*),

while the opening's height was a ratio of the beam's depth (h) (0.1*h*, 0.2*h,* and 0.3*h*). The test results showed that the rigidity of the beam was not affected by the concrete strength. However, small values of *a/h* produced more rigid deep beams. It was reported that the opening size had an influence on rigidity after the formation of diagonal cracks. The first diagonal crack was initiated at the top and bottom corners which were closer to the load and support. The beams failed in shear due to the propagation of diagonal cracks. The major failure cracks were always located in the lower load path. This indicated that the lower load path was more critical than the upper load path. Nevertheless, the failure crack was observed in the upper load path in a few specimens. Cracks pattern and failure mode were insignificantly influenced by the strength of concrete. A minimal influence on the beam shear capacity was observed when concrete strength changed. The influence of concrete strength became less as *a/h* ratio decreased.

El Maaddawy and Sherif [16] reported the behavior of RC beams with openings. The cracks initiated at the two opposite corners of opening towards the support and loading point. The cracks then widened as the load increased. The experimental results in this research showed that cracks were observed at a rang of 31% to 51% of the ultimate load. These cracks were observed early when the opening was located at the center of the load path. Minor flexural cracks were observed in some specimens before failure. Increasing opening size from 150 mm to 200 mm (0.3*h* to 0.4*h*) reduced shear strength by 21%. Whereas the load capacity reduced by 51% when the opening size changed from 200 mm to 250 mm (0.4*h* to 05*h*).

Pimanmas [17] found that adding an opening to RC beam changed the failure mode from flexural failure into shear failure. The author generally reported that square openings reduced the strength of RC more than circular openings. The circular and square openings reduced the capacity of solid deep beam by 37.7% and 44.3%, respectively.

Chin et al. [18] reported the behavior of beams with opening located at the midspan. The beam with circular opening failed in flexure with a sudden concrete crushing occurred at the upper chord. A similar failure mode was observed for a beam with square opening. The square opening had a higher influence on beam's loading capacity than circular opening. Comparing the strength of beams with opening with that of the solid beam, the capacity was dropped by 17% and 32% for beams with circular opening and square opening, respectively.

Campione and Minafo [19] reported experimental and analytical evaluation of the effect of circular web opening in RC deep beams with low shear span-to-depth (a/h) ratio. Twenty RC deep beams have been tested experimentally under two-point loading. Beams dimensions were 200 x 480 x 820 mm. The a/h ratio was 0.27. The location of the opening and amount of reinforcements were the main differences between test specimens. All beams with opening contained only one opening located either at the center of shear span or at the center of longitudinal span. The beams were designed to fail in shear. The longitudinal steel reinforcement was similar in most of the beams. The web vertical and horizontal reinforcement varied. Test results showed that the failure mode was dependent on the location of the opening. Load-deflection curves of test specimens showed that if the opening was located in the midspan of concrete deep beam, the behavior will not be affected in terms of load

carrying capacity and stiffness. However, locating the opening in the shear span reduced the shear load capacity by 18% to 30%.

2.3 Strengthening RC Deep Beams

2.3.1 Solid Deep Beams

Strengthening an existing RC beams is a common engineering practice. It is done to repair damaged beams or upgrade the load carrying capacity. Fiber-reinforced polymer (FRP) composites are favorable to be utilized for strengthening due to its' corrosion resistant, cost-effectiveness, and high strength. FRP is widely used to strength RC regular beams. However, limited researches have studied strengthening solid deep beams. Since deep beams fail in shear by inclined shear crack, the strengthening techniques were always applied in the shear spans.

Zhang et al. [2] have studied shear strengthening of RC deep beam by externally-bonded carbon fiber-reinforced polymer (EB-CFRP) laminates. The study investigated the effect of shear span-to-effective depth (a/d) ratio on the behavior of deep beam after strengthening and the efficiency of CFRP. The experimental program consisted of testing 16 beams classified under four groups. Each group varied by a/d ratio and the type of CFRP laminates. No internal web reinforcement was applied. All beams had the same dimensions. However, a/d ratio was changed by changing the number of loading points. The a/d ratio was 1.875 when one point load was applied, while when two point loads were applied the ratio became 1.25. Two types of CFRP strips were applied: Sika CarboDur® Strip bonded on lateral surfaces of beams, and SikaWrap Hex 230c® bonded on lateral surfaces only or as U-shaped wraps. Beams within each group had a different EB-CFRP strengthening

configuration with keeping one beam as control beam without strengthening. Test results showed that reducing *a/d* ratio resulted in an increase in shear capacity of deep beams. EB-CRFP reinforcement enhanced the shear strength of deep beams. The contribution of EB-CFRP was dependent on CFRP type and configuration. The contribution of CFRP strips in strengthening was increased when the strips were aligned either horizontally or at 45° and as *a/d* ratio decreased. In contrast, as *a/d* ratio decreased, the EB-CFRP reinforcement contribution decreased when CFRP strips were vertically aligned. Similarly, the contribution of vertical U-wrap CFRP laminates reduced at a low value of *a/d* ratio. In fact, anchoring U-shaped CFRP wraps have significantly increased the shear capacity of the deep beams. However, the influence of anchorage became more effective as the deep had higher *a/d* ratio. Nevertheless, CFRP laminates delamination has been observed in all strengthened beams.

Islam et al. [20] investigated the application of externally bonded CFRP laminates to upgrade load carrying capacity of RC deep beams. A total of six beams were tested under four-point bending. *a/h* ratio was equal to 0.75. Flexural and shear steel reinforcements were placed in the beam. Extra steel reinforcement cages were added at load and reaction points to prevent premature local failure in these locations. One beam was not strengthened as a control beam. Another beam was U-wrapped by two layers of FRP. Another beam was strengthened by diagonal CFRP strips. For the rest of the beams, CFRP grids were applied. The grids were varied in terms of size of grid bars, orientation of the grid, and bonding method. All strengthening CFRP reinforcements were placed at shear span of deep beams. Load-deflection curves showed approximately linear behavior up to 80% of the ultimate load. Firstly, flexural cracks generated at the midspan. Then, similar cracks that were

closer to the supports formed. After that, diagonal cracks started to appear in the shear spans. As the load was increasing, diagonal cracks were widening and their number was increasing. CFRP strengthening was found active in restraining the growth of diagonal crack width. The results showed that cracks' width in the strengthened beams were on average one-third of those in control beam. All beams failed by shear in the shear span. The CFFR laminates contributed to increase the load capacity by 35% and led to concrete crushing under the wrap. Similar enhancement in the load was recorded for CFRP strips strengthening. The failure occurred after peeling-off of concrete and separation of the strips. Strengthening of deep beam using CFRP grids increased the load by 24% to 43%. It was concluded that normal orientation of grids provided better strengthening. In addition, grooving of concrete surface served better bonding between concrete and CFRP grid which contributed to a better performance of deep beam.

Barros and Dias [10] studied the application of NSM-CFRP reinforcement on RC deep beams to upgrade shear strength. Four series with different beam's depths and longitudinal reinforcement steel ratios were tested under four-point bending. Each series consisted of two beams strengthened by NSM-CFRP oriented at 45° and 90°, in addition to three other beams for a purpose of comparison as follows: a beam without shear reinforcement, a beam reinforced by steel stirrups, and a beam strengthened by strips of wet lay-up CFRP sheets. Even though the depth of beams varied, all test specimens have *a/h* ratio was 2. The test results showed that beams without shear reinforcement failed by shear failure with formation of one shear crack without yielding longitudinal steel bars. Two test specimens of reinforced beams with steel stirrups failed by shear cracking after yielding of flexural steel reinforcement. However, pure shear failure was observed in another two beams of

larger depth. The beams that were strengthened by EB-CFRP strips failed by shear with peel-off of CFRP strips. Specimens with vertically aligned NSM-CFRP failed by shear and then slipping of laminates. Whereas the inclination of laminates to 45° changed the failure mode to flexural failure. The author concluded that using CFRP for strengthening can significantly enhance the shear capacity of RC beams. The NSM strengthening was more effective than EB-CFRP strengthening technique. The inclination of NSM laminates was found to be the most effective method. In general, applying NSM reinforcement on lateral surfaces of deep beams enhanced the behavior of the beam in terms of load carrying capacity and deflection capacity. The average increase in load was 83%. The specimens exhibited ductile behavior when strengthened by NSM-CFRP. Given that, the deflection value reached an average of 307% at 95% of maximum load. The installation of NSM technique was found to be simpler than EB technique.

Bousselham and Chaallal [21] have investigated how the shear strength of RC T-beam changes with different EB-CFRP ratios, web steel ratios and the type of the beam (slender or deep beam). In this research, 12 beam specimens were tested under three-point bending. Half of the specimens were deep beams with *a/h* ratio of 1.2. The second half were slender beams with *a/h* of 2.4. A bidirectional CFRP fabric were EB as U-shaped wraps of one or two layers. Experimental results showed that all beams failed in shear due to concrete crushing in the strut. No occurrence of premature debonding, delamination or fracture of CRFP was reported except in two slender beams. The overall behavior of deep beams was substantially better in term of load carrying capacity. However, the failure in deep beams was brittle while slender beams were more ductile. For deep beams specimens, there was low gain in shear strength when one FRP layer was added. The increment in the load was around

10%. In addition, the contribution of the second FRP layer to shear resistance was very minimal. Moreover, there was no noticeable improvement due to the presence of internal transverse steel reinforcement. On the other hand, the influence of CFRP strips and internal web reinforcement on slender beams were different. There was a significant contribution of CFRP laminates in shear strengthening when there was no internal web reinforcement. Besides, the addition of the second layer of CFRP for slender beams was effective. The enhancement in load carrying capacity jumped from 64% when one layer was used to 90% when two layers were used. The addition of internal transverse web reinforcement for slender beams has greatly enhanced the load carrying capacity. That affected the contribution of EB-CFRP in shear strengthening. The role of CFRP in strengthening was noticeably minimized with existence of internal web reinforcement. Only 13% increase in ultimate load was reported when a double layers of CFRP was used.

Lee et al. [22] examined the behavior of RC T-section deep beams strengthened in shear by EB-CFRP laminates. The parameters of the study included: strengthening length, fiber direction of FRP laminates, and the anchorage of FRP laminates by U-wrapping. A total of 14 RC deep beam specimens were tested under four-point bending. All test specimens had *a/d* ratio of 1.22. No web reinforcement was added to induce shear failure. CFRP sheets were applied on quarter, half and full length of the shear span. The strengthening was done using two layers of CFRP sheet EB on the lateral sides of the beams. U-wrapping of CFRP was applied on one specimen to test the effectiveness of U-wrap anchorage. The failure mode in control specimen was shear-compression failure occurred suddenly in inclined compression strut. All strengthened specimens had shear-compression failure due to partial delamination of CFRP laminates. Only one specimen that was strengthened all over

the shear span by two layers oriented horizontally was failed by shear-compression failure after a rupture of CFRP. The rupture of CFRP indicates the full utilization of EB-CFRP laminates' strength. This resulted in achieving the highest strength gain (66%). The failure in all beams was brittle. The load carrying capacity in all strengthened specimens was increased. However, enhancement in load carrying capacity varied according to the variability in strengthening method in the test specimens. The strengthening length was found to be significant in increasing the shear strength. As more portion of beam was strengthened by EB-CFRP laminates, the shear strengthening became more effective. Also, the fabric direction had a significant influence of strengthening. The influence reflected on the shear capacity and ductility of the deep beams. Applying U-shaped CFRP wraps as an anchorage was effective to increase shear strength, ductility, and initial stiffness.

Panjehpour [23] reported the effect of EB-CFRP strengthening on the deformation of the strut in RC deep beams with different a/d ratios. Two groups of specimens were tested under four-point bending. Each group consisted of six deep beams with a/d ratios of 0.75, 1.00, 1.25, 1.50, 1.75, and 2.00. One group was strengthened by EB-CFRP laminates while the other group was unstrengthened as a control group. One layer of unidirectional CFRP sheet was applied at shear span on lateral faces of the beams. All specimens failed in shear. However, unstrengthened beams failed in shear with CFRP rupture. Hence, the ultimate load capacity has significantly increased. The author reported that the deformation of the inclined strut was greater in transverse direction than longitudinal direction of the strut. This was caused by the existence of diagonal shear crack which widened the strut. High values of transverse strain in strut were measured when a/d ratio was high. CFRP strengthening was functional to restrict strut widening. The contribution of CFRP

laminates to resist strut widening increased as *a/d* value increased. One reason of this is because the cracks had more space to propagate in case of high *a/d* ratio. The restrain of strut widening became more noticeable as the load was increasing. CFRP sheets had a minor effect on strut compressive strain.

Li and Leung [24] investigated the performance of strengthened RC beams by full-wrapping of EB-CFRP strips and how the performance was affected by the change in *a/d* ratio. Experimental testing was done on 12 beams divided into two groups: control group, and strengthened group. The beams were tested under four-point bending until failure. The *a/d* ratio varied for each group of specimens from 1 to 3.5 with 0.5 intervals. All beams had the same cross-section. However, the longitudinal dimension was either 2000 or 2400 mm. The variability in beams length was needed to achieve different *a/d* ratios. Also, the point loads were applied on different positions according to the required shear span length for each beam. That provided unsymmetrical beams over the long direction. So, the EB-CFRP strengthening was applied on one side only. While the other side was heavily reinforced with vertical steel stirrups to prevent failure in that side. The strengthening scheme was done by full-wrapping of a 60 mm wide EB-CFRP strips with 150 mm center to center spacing. Shear failure was the dominant failure mode for all specimens. However, full and partial CFRP rupture accompanied the shear failure in strengthened beams. The achieved ultimate load by each strengthened beam was higher than the ultimate load of the corresponding control beam. The shear capacity slightly decreased as the *a/d* ratio became higher. It was reported that the strengthened beams with low *a/d* ratio (e.g. *a/d*= 1, 1.5) failed gradually. That was attributed to the strong existence of arch action, so the propagation of the inclined shear crack occurred at a relatively slow rate. Whereas, the development of the

inclined shear crack became more rapid as *a/d* value increased. That caused brittle failure with a sharp drop in strength. The contribution of EB-CFRP in shear strength varied between 14.1% and 62.8% according to the value of *a/d* ratio.

Hussain and Pimanmas [6] investigated the effectiveness of EB sprayed fiber-reinforced polymers (SFRP) to strengthen RC deep beams. The testing program in this research consisted of testing 17 RC deep beams under three-point bending. All beams had 100 mm by 300 mm cross section with 900 mm length. The beams were designed to fail in shear prior to flexure. Vertical and horizontal web steel reinforcements were added. The studied parameters were: strengthening material (glass, or carbon SFRP), SFRP thickness (7, 5, 4, or 3 mm), SFRP configuration (side faces, or side faces and bottom face together) and anchoring system. The anchorage of SFRP was used to prevent premature debonding. SFRP was sprayed on control beam without anchorage. In other specimens, slits on lateral surfaces on beams were used to mount the SFRP. The slits were aligned to be perpendicular to the expected shear crack. The used anchorage systems were Through Bolt, Mechanical Expansion Bolt, or Epoxy Bolt. Shear failure was observed in unstrengthened beams with the formation of major inclined shear crack. The failure mode of strengthened specimens was typically shear failure. However, in strengthened specimens without anchoring system and strengthened by SFRP slits, a debonding of SFRP was observed. That induced similar behavior to the control beam in terms of maximum load and deflection in the strengthened specimen without anchorage. Utilizing anchoring systems resulted in an enhancement in load carry capacity. Pull-out of anchorage was observed in some specimens which resulted in less contribution to strength enhancement. While strong anchorage led to a rapture of SFRP and an increase in load capacity. The strength rise was proportional to SFRP

thickness in case of sufficient anchorage applied to prevent delamination. Specimens strengthened by carbon SFRP had a higher load capacity comparing to specimens strengthened by glass SFRP. Adding a layer of SFRP at the bottom side of the beam in addition to lateral sides increased the ultimate load by 20%. The author concluded that the usage of SFRP without anchoring system was not effective. The SFRP rupture was observed in most of the strengthened beams with anchorage This indicates the effectiveness of anchoring systems and full utilization of SFRP strength. So, strengthening deep beam with anchored SFRP is an effective method to upgrade load carrying capacity and enhance ductility. Given that Bolt system was found the most effective anchoring system.

Li and Leung [7] investigated the effect of a/d ratio on shear strength of RC beam and on the contribution of CFRP U-wraps to strengthen the beam. The experimental testing was done on 12 beam specimens. Six of them were strengthened with CFRP. Each beam had a different a/d ratio. The a/d ratios ranged from 1 to 3.5. The second group of beams was control group without strengthening. The beams were tested under four-point bending. A 60 mm wide rips with 150 mm spacing was applied in U-shaped wraps on the beams. Test results showed that ultimate load was reached with the onset of debonding of CFRP in most of the specimens. Whereas a repute in CFRP was observed only in few specimens. CFRP debonding failure was characterized as brittle failure as the beam fails instantly without warning. For deep beam specimens with low a/d ratio, a debonding occurred gradually. As a result, there was no sudden failure in this type of beams. The strips which located close to the support were not damaged as if they intersect the critical shear crack. The strips located near the loading point debonded well before reaching the ultimate load due to short bond length above the developed shear crack. FRP rupture that occurred in a

few specimens was due to sufficient bond length above the shear crack. Regarding the effect of *a/d* ratio on shear capacity of the beam, it was reported that control and strengthened beams showed similar response to *a/d* ratio. A gradual drop in shear strength was reported as the *a/d* ratio increased. The FRP contribution to shear strength was significantly varied according to various *a/d* ratios. The curve of the change in shear strength versus *a/d* showed rough parabolic relationship. The strengthening was most effective (31% increase in strength) when *a/d* was 2. The effectiveness reduced slightly as the ratio became higher. However, an obvious drop in the effectiveness occurred when *a/d* value became less than 2. Only 12.8% and 2.5% upgrade in shear capacity was recorded when *a/d* was equal to 1.5 and 1, respectively.

2.3.2 Deep Beams with Openings

Several research works have studied applying external strengthening techniques on deep beams with openings to restore the behavior and load carrying capacity to solid deep beams.

El-Maaddawy and Sherif [16] studied the effectiveness of using EB-CFRP sheets to upgrade the capacity of concrete deep beams with square openings. The study included 13 beams that were tested under four-point bending. The openings size ranged between 0.3h and 0.5h, where h is the beam depth. The location of openings was at center of the load path and above and below the load path. Two failure modes were observed for deep beams without CFRP strengthening. The first was splitting in the top and bottom chords. The splitting was the successive action of the diagonal shear cracks. The second mode of failure for beams with openings occurred by rotation of three sides of opening. The failure in strengthened beams

occurred suddenly by formation of two diagonal shear cracks above and below the opening in addition to pull out of concrete at the top chord. CFRP repute occurred at the bottom chord when opening location was above the load path. When the opening was located below the load path, CFRP sheets detached in the top chord. Strength gain ranged between 66% and 71% when the opening was at the center of load path.

El Maaddawy and El Ariss [25] studied the behavior of RC beams with short shear span and web opening in the shear span. The beams were strengthened by EB-CFRP sheets around the opening. The test variables were the opening size and number of EB-CFRP layers. The results showed that all specimens failed in shear. The strain in longitudinal steel reinforcement did not reach yielding strain. A major crack at 45° was formed in the solid beam. In all beams without strengthening, diagonal cracks initiated from the two corners of the opening near the supports and loading points. The first signs of failure in strengthened specimens were delamination and/or rupture of CFRP sheets at corners of openings due to stress concentration at corners. The strengthened beams with EB-CRFP reinforcement showed an improvement in shear capacity as compared to control beams with opening. The number of applied layers of CFRP was not proportional to the increase in the load capacity. The strength gain was affected by the angle of inclination of lower load path. As the angle increased, a higher strength gain was achieved. Having an angle of 11° or more resulted to restore 90% to 100% of shear capacity of the solid beam.

Vuggumudi [26] had studied the application of EB glass fiber-reinforced polymer (GFRP) sheets on RC T-beams with web opening. The studied parameters were steel stirrups, shear span-to-depth ratio (a/h) and GFRP amount. Eleven RC T-

beams have been tested under a four-point bending system. The beams were divided into two groups according to the presence of internal shear reinforcement, steel stirrups were used in one group only. In each group, two beams were without FRP strengthening, one was solid beam and the other was with web opening. Shear span-to-depth (a/h) ratio for test specimens was either 2.66 or 2. GFRP sheets were applied by different schemes. Two or four layers of GFRP were applied on shear zones as U-wrap with and without anchorage. The GFRP sheets were anchored by GFRP plates at bottom surface of flange. Test results showed that the strengthening improved the capacity of RC T-beams with openings. Flange anchorage system was found to be effective and prevented debonding, thus strengthening became more effective to increase shear strength. The contribution of GFRP sheets to shear strength was higher in the absence of web steel reinforcement. The upgrade in shear capacity by EB-GFRP was increased as the a/d ratio decreased.

Ahmed et al. [27] investigated the effect of the thickness of externally bonded steel plate in repairing RC deep beams with opening. The usage of steel plate was compared with the usage of CFRP plates. A total of four beams were tested. All beams had an opening in shear spans. A control specimen was repaired by CFRP plates while the rest of the specimens were repaired by steel plates. EB plates were placed around the opening. All beams failed by formation of diagonal shear cracks at the corners of the opening. For repaired beams with CFRP plate, no fracture or debonding was observed. However, splitting failure and concrete crushing were observed in some repaired specimens. The strengthening using EB-CFRP or steel plates increased the load carrying capacity of the beams. The application of 2, 3 and 4 mm thick steel plates increased the load by 28%, 30%, and 32%, respectively.

Nevertheless, the load carrying capacity increased by 43% when EB-CFRP plates were used.

Osman et al. [8] examined the structural behavior of pre-cracked RC deep beams with opening repaired by aramid fiber-reinforcement polymers (AFRP) sheets. A total of seven rectangular RC beams were tested under four-point bending. Circular opening with 140 mm diameter was placed in the shear span. The beams were pre-loaded to generate cracks. The applied load was either 50% or 70% of the ultimate load of the control beam with opening. Then AFRP sheets were applied while keeping the load constant. After that, the load increased until failure. AFRP sheets were applied in U-wrap shape. Two layers with different directions were applied. One layer was placed horizontally, and the other was placed either vertically or inclined (60°). Test results showed that the solid concrete beam failed in shear by formation of diagonal crack at natural load path. The inclusion of an opening in shear span reduced the shear capacity by 50%. For strengthened beams, the bond interface was reported as the weakest point in the system. AFRP debonding or peeling occurred at failure in every strengthened specimen along with shear failure or concrete crushing. The strengthening system has increased the shear load capacity in a range between 21.8% and 66.4%. Inclination of FRP sheet at 60° was found more effective than vertical orientation of the sheets. Strengthened beams with AFRP exhibited a higher level of ductility. The contribution of AFRP sheets to shear resistance reduced as the damage level increases.

2.4 Strengthening of RC Slender Beams with Openings

The research works that studied strengthening of regular RC beams are presented in this section. Most of researchers used EB reinforcement technique to strengthen the beams.

Mansur et al. [11] attached EB-FRP strips on beams side surfaces near the opening aligned at 45°. It was reported that usage of EB-FRP strips succeeded to restore full strength of the beam.

Abdalla et al. [13] studied the application of EB-CFRP sheets on regular RC beam with rectangular web openings. The openings were located in the shear spans. The size of openings varied. Different configuration of CFRP sheets and various amounts of CFRP layers were applied. Unidirectional CFRP fabrics were externally bonded around the opening. Internal web steel reinforcement was used in all the beams. As per the test results, all beams except three failed in shear. The solid beam in addition to two strengthened beams with openings failed in flexure. All strengthening schemes yielded to decrease deflection, control cracks around openings and enhance the strength. However, the load capacity in only one of the specimens was restored when the opening size was 40% of the total beam depth.

Allam [28] investigated the applicability of EB steel plates and CFRP sheets to strengthen RC beams with large web opening in the shear span. Three test specimens were considered as control beams: solid beam, beam with opening and internally strengthened beam around the opening by steel bars. Another six beams specimens with web opening and external strengthening were tested. The openings were rectangular and located in the shear span. External strengthening was applied

using one of the two materials (Steel plates or CFRP sheets) by different schemes. All steel plates were bonded using epoxy adhesive. However, in some specimens, the bond was enhanced by anchoring the plates by bolts. Steel plates were applied around the opening and inside the opening for some specimens. CRFP sheets were applied either as combination two layers vertically and horizontally oriented around the opening or as U-shape wraps on all inner sides of the opening with another layer above the U-wrap in perpendicular direction. Applying steel plates provided better results than applying CFRP sheets application. The homogeneity in steel plates offered more resistance to diagonal cracks than unidirectional CFRP sheets. In general, the application of strengthening technique on internal and external sides of the opening was more effective than strengthening the external sides only. The scheme of bonding the steel plates around the opening and at inner faces of the opening achieved the best result by restoring the solid beam load capacity and changing the failure mode to flexural failure mode. Adding steel bolts to the system had a marginal effect but the beam stiffness was reduced due to the drilled holes in the concrete. U-wrapping scheme of CFRP sheet was more effective than the placing sheets on side surfaces of beam around the openings.

Pimanmas [17] investigated strengthening of RC beams with opening using NSM-CFRP rods. The specimens contained either square or circular openings. All openings were located at the center of shear span. CFRP rods mounted externally in grooves positioned as closed square around the opening or diagonally beside the opening extended over the beam's depth. Strengthened specimens with CFRP were compared with specimens that contained prefabricated internal steel bars around the opening. Applying CFRP reinforcement around the opening had enhanced the strength of the beam but the failure mode of solid beams was not restored. However,

strengthening using diagonal CFRP rods beside the opening yielded to have similar load capacity to solid beam. The bottom diagonal CFRP rod was more effective in shear resistance than the top one. The analytical analysis showed that inclined rods were more effective than fixing the rod in a vertical position. As such, the diagonal rods are perpendicular to cracks. In addition, placing a strengthening system away from opening doesn't strengthen the beam. If the opening is too big, the strut area in the concrete will be small and the utilization of CFRP rod to carry tension stresses will be insignificant. The length of CFRP rods affected the performance.

Chin et al. [18] examined the behavior of RC beams with large openings in the flexure region strengthened by CFRP laminates. The experimental program consisted of testing five RC beams with and without openings. Square or circular openings were cut in the center of midspan. The openings size was 75% and 82% of beam's effective depth. The CFRP laminates were unidirectional and externally bonded on concrete surface by epoxy resin. For beams with circular opening, CFRP laminates were applied horizontally above and below the opening, diagonally beside the opening and on the top and bottom surfaces of beam at the midspan. The laminates configuration was different for beams with square opening. The laminates were applied on the inner sides of the square opening and on the bottom surface of the beam. The control solid beam failed in shear. A major diagonal crack connecting the loading point and the support formed and the flexural steel reinforcement yielded concurrently. Strengthened beam with circular opening failed in shear by formation of large diagonal crack and crushing of concrete near support. In addition, the bottom reinforcement steel yielded. The strengthened beam with square opening failed in flexure by peeling of concrete cover at the bottom surface of beam in addition to concrete crushing in the top chord after yielding of the top steel. It was also observed

that CFRP laminates delimited at the top and bottom surfaces of the top chord. The strengthening technique for beam with circular opening significantly enhanced beam's capacity. The load capacity exceeded that of the solid beam by 42%. However, the strengthening method of square opening didn't restore the capacity and only increased the load carrying capacity by 10%, as compared to the unstrengthened beam with openings.

Mondal et al. [29] tested the behavior of RC beam with square opening strengthened by GFRP laminates. Ten specimens were tested under four-point bending. The openings were located in the shear spans. The height of all openings was 100 mm (0.38h), while the width was 100, 200, or 300 mm. An isotropic GFRP laminates were wrapped around the opening. The beams failed in shear either by rupture or debonding of GFRP. The application of proposed strengthening techniques did not restore the full capacity of the solid beam.

Diggikar et al. [30] investigated the behavior of reinforced cement concrete (RCC) beams with rectangular openings and strengthened by EB-CFRP or EB-GFRP sheets with different configurations. The experimental study consisted of testing ten specimens under four-point bending. Two of them were control specimens: a solid beam, and a beam with rectangular web opening. The rest of specimens included an opening and strengthened by CFRP or GFRP sheets with different configurations: around the opening, inside the opening, inside and around the opening, and as double layer around the opening. Steel stirrups were used as internal web reinforcement. Flexure failure mode was observed in the solid beam, nevertheless, some of the strengthened beams failed by flexure and others by shear. The strengthening using GRFP sheets increased load caring capacity by 3.74% to 37.41%, while 9.35% to

50.50% increase in the capacity was reported when CFRP sheets were utilized. Applying CFRP sheets around and inside the opening was the most effective technique. Whereas, placing FRP sheets around the openings on the side surface of the beam was more effective than placing the sheets inside the opening.

Fawzy [31] had experimentally investigated the application of EB steel plates and CFRP strips on RC deep beams with openings. A total of eight beams were tested under three-point bending. Square openings have been constructed in the shear span. The opening's height-to-beam's depth ratio was 0.5. According to the experimental results, the solid beam failed in flexure, while inclusion of an opening in beam's web changed the mode of failure to shear failure. All strengthening methods increased the load carrying capacity of beams with openings. All strengthening techniques except one didn't restore the solid beam capacity and the failure mode remained in shear. However, the full capacity and failure mode were restored when steel plate was bonded on the side faces of the beam around the opening.

2.5 Strut-and-Tie Model Design

The Strut-and-tie model (STM) originally belongs to the truss analogy which was introduced by Ritter [32] and Morsch [33] in the last century. The STM was proposed by Schlaich and Schäfer [34] as truss analogy for special cases of structural concrete with complex stresses flow (e.g. dapped-end beams, corbels, deep beams, and walls with openings). The guidance and constraints of developing STM are limited, which leaves a lot of engineering judgments and decisions to the designer. For example, determining the layout of load-resisting truss is an open-ended problem. There are no certain steps or procedures mentioned by the code to develop

the truss layout. The STM approach is considered in several practice codes and guidelines of several international organizations (e.g. American Association of State Highway and Transportation Officials (AASHTO), American Concrete Institute (ACI), Canadian Standards Association (CSA), and The international Federation for Structural Concrete (FIP)).

Kuchma et al. [35] have experimentally tested the validity of multiple STMs on three different D-regions. A total of 11 specimens which include three types of D-regions with different STMs were loaded until failure. The specimens were: a deep beam with a rectangular opening, a propped cantilever beam with an opening, and a beam with a dap at one end and an opening adjacent to the support at the other end. Several STMs were developed for each one of the D-regions. A grid reinforcement was added for all specimens to provide a cracking control for bottle-shaped strut. Steel reinforcements were placed in the ties locations. The author reported that STM can precisely predict the failure mode and failure location in some. The failure position changed as the truss model changed. In the specimens where steel reinforcements were added at ties locations, the internal stresses found to be redistributed and new cracks developed in different locations as the load increased. Comparing that with specimens with only welded-wire grid reinforcement, cracks initiated at certain locations and propagated as the load increased. The author compared the measured strain in some struts and ties with the theoretical values. It was reported that the measured strain in the strut is more than model-based strain and that could be due to the overestimation of strut cross-section area by the STM. Even though, the transverse strain was maximum at the middle of the strut and consistent with ACI code which assumes the formation of bottle-shaped strut. On the other hand, the measured values of steel strain were in good correlation with the calculated

values from the model. The author concluded that STM design under the provisions of ACI code is conservative in estimating the load caring capacity of structures with D-regions. The structures in real cases exhibit ductile behavior after peak load and that is against plastic truss assumption in STM. The layout of STM truss significantly affects the load-deformation response and failure locations. The stiffness of truss members can be properly estimated by STM assumptions.

Ley et al. [36] conducted experimental tests on simply supported dapped beams with openings to verify the validity of STM design method. Experimental tests were conducted on two series of specimens. The first series consisted of six relatively small-scale specimens including control specimen with no reinforcement. Each specimen was designed by different STM using the provisions of ACI 318-05. The second series consisted of two larger scale specimens to investigate the size effect on the precision of STM. Two irregularities (dapped end and web opening) were added to beams geometry which generates D-regions. The dimensions of the dapped side were 1/3 of beam length and 2/5 of beam height. One web opening was located under the point load at the mid-height. The opening dimensions were 1/3 of beam length and height. Steel reinforcements were added at ties locations, however additional steel was added at some locations to strengthen the struts where high load was anticipated. The control specimens without reinforcement failed by concrete fracture either in the lower chord or in the upper and lower chords. All reinforced specimens failed at higher load than the design load. All specimens showed liner behavior in load-deflection response except one specimen where the beam was designed by STM to provide ductility for the beam. The specimens had different failure modes and different crack patterns. However, some specimens had a similar mode of failure which involves shear failure (bottle strut failure), then formation of

flexural hinge and then collapse. The author concluded that the size effect on beams behavior is minimal as long as adequate reinforcement is provided. STM was not found to be a reliable tool to predict the failure mode or load capacity.

Godat and Chaallal [9] investigated the effectiveness of STM to predict the loading capacity of large scale deep T-beams strengthened by EB-CFRP laminates. A total of 12 beams were tested under three-point loading to validate the proposed STM. The test specimens were divided into four groups based on the spacing between steel stirrups. The *a/d* ratio for all beam was equal to 2. Specimens were strengthened by single, double, or triple layer of CFRP U-wrapping. The experimental results showed that the gain in load due to EB-CFRP strengthening ranged between 10.75% and 35.6%. As the steel stirrups were distributed over the shear span and the EB-CFRP sheets covered the whole length of the shear span. The STM contained a vertical tie located at the middle of shear spans, that corresponded to the steel stirrups and CFRP sheets in the shear span. The nominal strength of CFRP sheets used in STM calculations was calculated based on the effective strain as specified by ACI-440 [37]. STM predictions using ACI 318-08 code for the shear capacity of test specimens was very conservative. While the modified STM calculations which were based on ACI provisions but without strength reduction factors produced more accurate results as compared to experimental results. The STM has predicted the exact value of the ultimate load for beams with least amount of steel stirrups. Nevertheless, the load capacity predictions for all beams was governed by nodal strength, while the failure experimentally was governed by debonding of CFRP strips.

Lobsang [38] investigated the utilization of STM using ACI 318-11 provisions and numerical modeling to predict the behavior of deep beams with openings. Experimental work was conducted to verify the predictions of STM and numerical model. Three test specimens were studied. All of them had the same truss layout, however, extra reinforcement was added in two specimens to strengthen a strut where higher load was anticipated. In one of these two specimens, thicker bearing plates were used. The author reported that load capacity prediction by STM was always lower than the actual capacity. Diagonal reinforcement showed a positive effect on the beam capacity while STM underestimates the contribution of diagonal steel reinforcement.

2.6 Finite Element Modeling

Numerical finite element (FE) modeling is a modern approach to simulate the nonlinear behavior of complex structural elements. Some researchers have used FE modeling to analyze structural behavior of beams with discontinuity strengthened by composite materials.

Chin et al. [39] developed nonlinear FE model of RC beams with openings and compared the findings with the experimental results. The experimental results were obtained from Chin et al. [40]. ATENA software was used for developing 2D model. Six RC beams were modeled with four-point bending. Steel stirrups was used as internal web reinforcement. The location of openings was either $0.5d$ or d away from supports, where d in the effective depth of the beam. CFRP laminates were applied as full wraps at all edges. Bond slip model from a previous study was utilized. The numerical model results showed that load-deflection curves of FE models and experimental tests were comparable in term of load capacity. But there

was a difference in the deflection values because beams in FE model behaved stiffer due to perfect bond configuration between reinforcement steel and concrete. The model's predictions of crack pattern and location was considered.

Hawileh et al. [41] developed FE models to simulate the behavior of concrete beams with square openings strengthened by EB-CFRP sheets. A total of 12 beams were modeled. The beams varied in opening locations (at center of shear span, at top of shear span, or at bottom of shear span), opening size (150, 200 or 250 mm) and CFRP sheets alignment. Perditions of the numerical models were compared with experimental results reported by El-Maaddawy and Sherif [16]. FE model results showed that unstrengthened beams failed by yielding of shear steel reinforcement and development of major cracks in concrete. Strengthened beams failed by debonding of CFRP. Load-deflection curves of FE models were accurate as compared to those of the experimental tests. Also, the crack patterns in the FE models were relevant to the experimental observation. In general, the numerical modeling was conservative as it underestimates the strength and overestimates the deflection. Utilizing a bond-slip model for the bond between the concrete and CFRP sheet made the FE model results more accurate and relevant to the experimental results. In addition, debonding failure became possible in the model when bond-slip model was utilized.

2.7 Research Significance

No design equations are available in conventional building codes for designing concrete D-regions externally-strengthened with NSM composite reinforcement. More research is needed to develop an improved understanding of the behavior of concrete deep beams strengthened with NSM-composite reinforcement

around regions of extreme discontinuities. There is also a need to develop a modeling technique that can predict and simulate the nonlinear behavior of such complex structural elements. This research aims to fill this gap through experimental testing, strut-and-tie modeling, and numerical simulation. The effectiveness of the NSM-CFRP strengthening to upgrade the capacity of concrete deep beams with extreme discontinuities is elucidated. The accuracy and validity of the STM to predict the load capacity of concrete deep beams strengthened with NSM-CFRP reinforcement around the D-regions are examined. Numerical simulation models capable of predicting the nonlinear behavior of concrete deep beams with openings strengthened with NSM-CFRP reinforcement are developed. Research findings are expected to assist practitioners and researchers to develop rational and consistent solutions to solve complex structural engineering problems typically encountered in field applications.

Chapter 3: Development of Strut-and-Tie Models

This Chapter presents the details of the strut-and-tie models (STMs) for the reinforced concrete deep beam specimens of the current study. STM provisions of American Concrete Institute (ACI) code ACI 318-14 [1] and Canadian Standards Association code CSA S806 [5] are reviewed in this chapter. Four different STMs were developed: one model was for a solid deep beam and three models were for the deep beam specimens with openings strengthened by NSM-CFRP.

3.1 Provisions of ACI 318-14

The analysis of STM in ACI 318-14 [1] code accounts for the strength of struts, ties, and nodes. It is specified that the angle between the strut and tie axis at a node should be at least 25°. That is for the purpose of mitigation of cracking and avoid incompatibilities as the strut shortens almost in the same direction of the tie elongation [42]. The load carrying capacity of a structure is calculated based on the strength of concrete struts, ties and nodal zones.

3.1.1 Concrete Struts

The nominal strength of a concrete strut (F_{ns}) without longitudinal reinforcement in the strut is calculated by Eq. (3.1).

$$F_{ns} = 0.85 \, \beta_s \, f'_c \, A_{cs} \qquad (3.1)$$

Where β_s is strut coefficient, f'_c is concrete compressive strength and A_{cs} is the cross-sectional area of the strut. β_s accounts for the influence of cracks and crack-control reinforcement within the strut on the compressive strength of concrete.

Table 3.1 shows the values of β_s for normal weight concrete as mentioned in ACI 318-14 [1] code. The area of strut cross-section (A_{cs}) shall be the taken at the smaller strut end, so it would result in calculating a conservative value of F_{ns}.

Table 3.1: Strut coefficient for normal weight concrete as per ACI code

Strut geometry and location	β_s
Struts with uniform cross-sectional area along length	1.0
Bottle-shaped strut with internal crack control reinforcement	0.75
Bottle-shaped strut without internal crack control reinforcement	0.6
Strut located in tension members	0.4
All other cases	0.6

3.1.2 Ties

The nominal tensile strengths of steel and CFRP ties (F_{nt}) are calculated by Eq. (3.2) and Eq. (3.3), respectively, where f_y is the yield strength of steel, f_{fe} is effective strength of the CFRP, C_E is an environmental reduction factor, f_{fu} is the ultimate strength of CFRP, A_{ts} and A_{tf} are the total cross-sectional area of steel bars and CFRP strips, respectively. The value of C_E was taken as 1 in this study because the specimens were fabricated and tested in the laboratory.

$$F_{nt} = f_y \, A_{ts} \qquad (3.2)$$

$$F_{nt} = f_{fe} \, A_{tf} \qquad (3.3)$$

$$f_{fe} = C_E \, f_{fu} \qquad (3.4)$$

3.1.3 Nodal Zones

The nominal compressive strength of nodal zones is calculated by the Eq. (3.5). Where β_n is nodal zone coefficient and A_{nz} is the nodal zone area that is perpendicular to direction of the applied force. The values of β_n are presented in Table 3.2 as specified in ACI 318-14 [1].

$$F_{nn} = 0.85 \, \beta_n \, f'_c \, A_{nz} \qquad (3.5)$$

Table 3.2: Nodal zone coefficients as per ACI code

Configuration of nodal zone	β_n
Nodal zone bounded by struts, bearing areas, or both (CCC)	1.0
Nodal zone anchoring one tie (CCT)	0.8
Nodal zone anchoring two or more ties (CTT or TTT)	0.6

C: Compression force
T: Tensile force

3.2 Provisions of CSA S806

CSA S806 [5] provisions specify strength capacity equations for struts, ties and node regions where the applied force shall not exceed the calculated capacity.

3.2.1 Concrete Struts

The CSA S806 [5] considers the effect of ties' strain on the strength of an adjoining strut. The strut design capacity (F_s) is calculated using Eq. (3.6) to Eq. (3.8). Where ϕ_c is the resistance factor for concrete (taken as 1 in this study to calculate the nominal capacity instead of design capacity), f_{cu} is the limiting compressive strength in the strut, f'_c is the concrete compressive strength, ε_1 is a

factor that accounts for transverse tensile strain in a cracked strut, ε_f is the tensile strain in an adjoining tie to the strut, and θ_s is the angle between the strut and the adjoining tie. The CSA S806 [5] allows to take the value of the tie strain at the centerline of the strut if the strain in the tie varies across the width of the strut. Thus, strain might be taken as half of the calculated strain in the tie [43].

$$F_s = \phi_c \, f_{cu} \, A_{cs} \tag{3.6}$$

$$f_{cu} = \frac{f'_c}{0.8 + 170 \, \varepsilon_1} \leq 0.85 f'_c \tag{3.7}$$

$$\varepsilon_1 = \varepsilon_f + \left(\varepsilon_f + 0.002\right) cot^2\theta_s \tag{3.8}$$

3.2.2 Ties

The tie design capacity (F_t) is calculated for steel reinforcement as follows:

$$F_t = \phi_s \, f_{sy} \, A_{st} \tag{3.9}$$

Where ϕ_s is a resistance factor for steel which was taken as 1 in this study to calculate the nominal strength, f_{sy} is the yield tensile strength of the steel reinforcement, and A_{st} is the total cross-sectional area of the reinforcement.

The design capacity of CFRP tie (F_t) of is given by Eq. (3.10).

$$F_t = \phi_f \, f_{fu} \, A_{ft} \tag{3.10}$$

Where ϕ_f is a resistance factor for FRP which was taken as 1 in this study to calculate the nominal strength. f_{fu} is the ultimate tensile strength of the CFRP reinforcement and A_{ft} is the total cross-sectional area of the CFRP strips.

3.2.3 Nodal Zones

The calculated compressive stress at nodal zones should not exceed the following limits:

- 0.85 $\phi_c f'_c$ for nodal zones bounded by struts and bearing areas (CCC)
- 0.75 $\phi_c f'_c$ for nodal zones anchoring one tie only (CCT)
- 0.65 $\phi_c f'_c$ for nodal zones anchoring ties in more than one direction (CTT or TTT)

Where C and T denote for compression and tensile forces, respectively.

3.3 Geometry of Test Specimens

The size of the deep beam specimens tested in this study was constant. The specimens were 2700 mm long, 500 mm deep and 150 mm wide. The beams rested on two supports rendering an effective span of 2100 mm. The specimens were subjected to two point loads, each was applied at distance 400 mm from the support. Steel bearing plates for supports and loading points had a width of 100 mm and extended all over the beam width. Shear span-to-depth ratio (*a/h*) was equal to 0.8. Beams with extreme discontinuity had a 100 x 100 mm square opening. The center of the opening was located at the midpoint of the shear span. The longitudinal steel reinforcement was placed at a distance of 50 mm away from the bottom surface of the beam. Figure 3.1 shows the dimensions of typical deep beam specimen.

(a) Solid beam

(b) Beam with opening
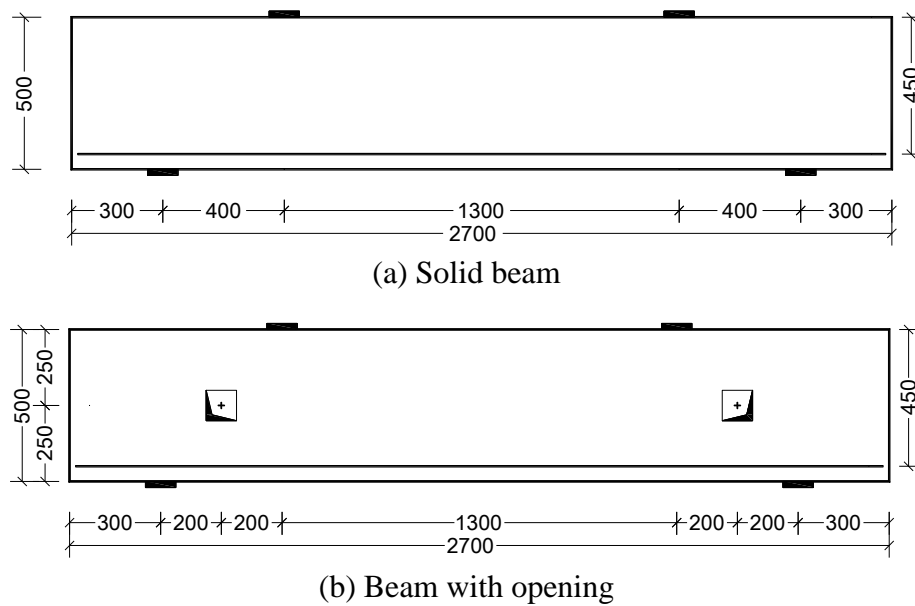
Figure 3.1: Deep beams dimensions

3.4 Development of Models

The development of STM begins by forming a truss layout where the internal stresses are assumed to flow through. The internal stresses are generated by the externally applied load. The stresses flow from the bearing plates of applied loads through the beam depth to the bearing plates of the supports. The STM design method allows designers to choose any STM deemed suitable for a particular problem. Although STM offers great flexibility in structural design, its accuracy and validity are still questionable because of the uncertainties in defining the strength and dimensions of the idealized load-resisting model [36, 44–46]. Identifying a proper STM requires several iterations to ensure stability and compatibility of the truss. For example, compression and tension members should be placed at the anticipated compression and tension zones, respectively. The developed STMs were used to determine the layout of three different NSM-CFRP strengthening schemes around regions of discontinuities. One STM was developed for the solid beam as shown in

Figure 3.2 and three other models (STM I, STM II and STM III) were developed for the deep beams with openings as shown in Figure 3.3 to Figure 3.5.

In all STMs, there were two longitudinal members in the constant moment region: one horizontal strut located at the top of the beam (S1) and one horizontal tie located at the bottom of the beam (T1). These two members account for the generated moment at the midspan which results in a compression stress at the top and a tensile stress at the bottom. The longitudinal tie was placed at the same depth of the longitudinal steel bars (450 mm from the top). The height of the nodal zone at the support was assumed to be quale to two times the concrete cover (100 mm). The nodes at the supports were CCT nodes. The nodal zone coefficient (β_n) for such nodes is equal to 0.8 as per ACI 318-14 [1]. The nodes at the loading points were CCC nodes with β_n equals to 1.0. As such, the height of the nodal zone at the loading point was assumed as 80% of that for the nodal zone at the support.

The load transfer mechanism in the solid deep beam was assumed to be through a single inclined strut in each shear span, connecting the node below the loading plate with the node above support plate (Figure 3.2). A dashed line represents a strut and a solid line represents a tie.

The developed STMs for the deep beam specimens with extreme discontinuities included inclined ties around the openings. STM I and STM II included a single tie inclined at 45° located in the bottom and top chords, respectively. STM III included two inclined ties in the shear span, one tie was in the top chord above the opening inclined at 68° whereas the other tie was in the bottom chord below the opening inclined at 28° (Figure 3.5). The width of struts and the angles between truss members were determined graphically.
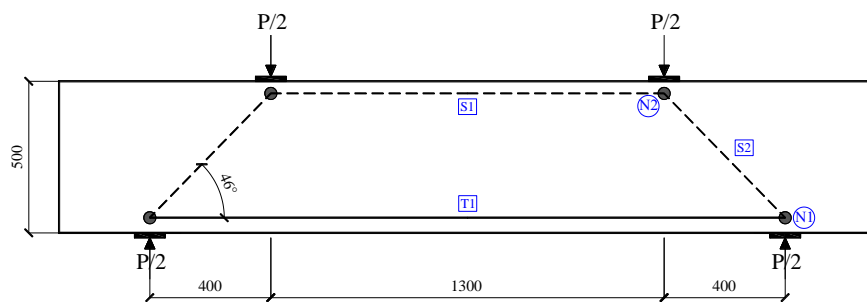
(a) Truss layout
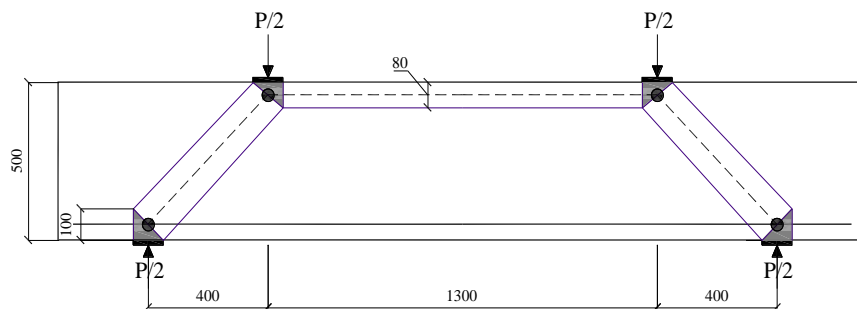
(b) Struts, ties and nodal zone

Figure 3.2: STM of solid deep beam details
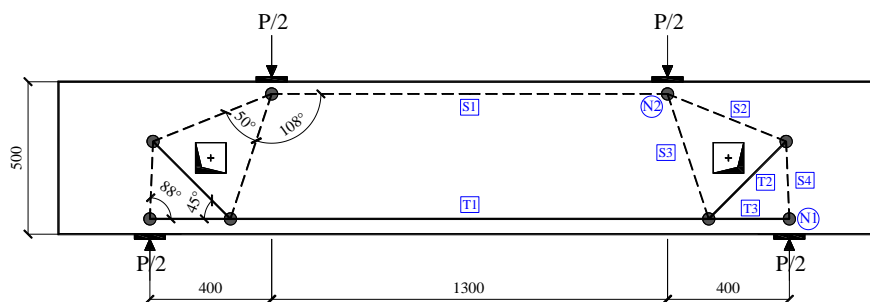
(a) Truss layout
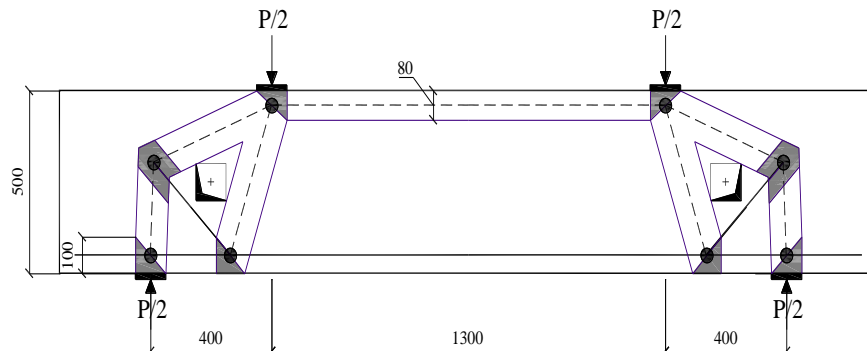
(b) Struts, ties and nodal zone

Figure 3.3: STM I details
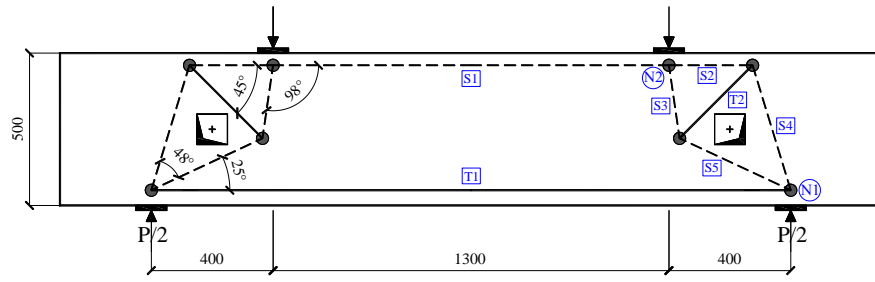
(a) Truss layout
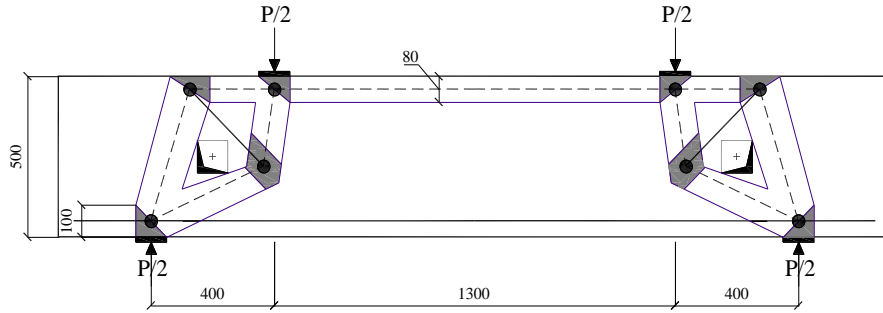
(b) Struts, ties and nodal zone

Figure 3.4: STM II details
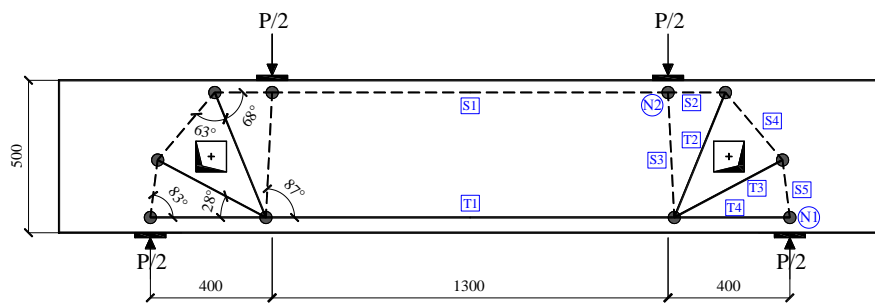
(a) Truss layout
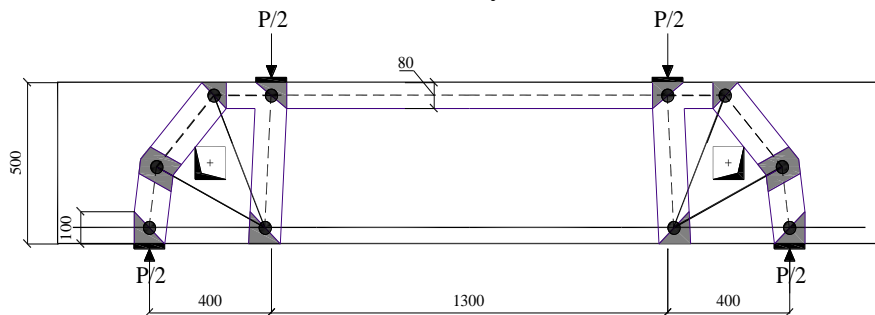
(b) Struts, ties and nodal zone

Figure 3.5: STM III details

3.5 Summary

The STM provisions of ACI 318-14 [1] and CSA S806 [5] were reviewed in this chapter. In this chapter the details of the three developed STMs: STM I, STM II, and STM III were presented. Each STM had a different configuration of ties around the discontinuity regions. The STMs will be used to determine the NSM-CFRP strengthening schemes as explained in the following chapter. Also, the details of specimens, strengthening technique, and testing procedures will be presented in the next chapter.

Chapter 4: Experimental Program

4.1 Introduction

In this chapter, an overall description of the experimental work of this research is presented. The purpose of laboratory experiments was to examine the behavior of RC deep beams with extreme discontinuities strengthened by NSM-CFRP and to determine the effectiveness of different NSM-CFRP strengthening schemes to improve the shear resistance of such beams. The laboratory experiments were also essential to examine the accuracy of the STM solution and numerical simulation model predictions. The main test parameters are the amount and configuration of NSM-CFRP strips. Three different configurations of strengthening schemes were adopted as per the proposed STMs. The deep beams with discontinuity regions included an opening in each shear span. The experimental work including fabrication and testing of specimens was carried out in the laboratories of the Civil and Environmental Engineering Department at the United Arab Emirates University.

4.2 Test Program

The experimental program is summarized in Table 4.1. A total of eight deep beam specimens were constructed and tested. One solid beam was used as a benchmark. The other seven beams had a square opening (100 x 100 mm) at the middle of each shear span that fully interrupted the natural load path. The opening height-to-beam depth ratio (h_o/h) was 0.2. One of the beams with openings was not strengthened. Whereas the remaining six beams were strengthened with NSM-CFRP reinforcement around the D-regions of the beam. The configurations of the NSM-CFRP reinforcement around the openings were based on different STMs: namely

STM-I, STM-II, and STM-III (refer to Figure 3.3 to Figure 3.5 in Chapter 3). The NSM-CFRP were applied as single or double strips. For all specimens, the shear span-to-depth ratio (a/h) was 0.8, concrete compressive strength (f'_c) was 40 MPa.

Table 4.1: Test matrix

Group	Size of cutout (mm)	Strengthening scheme	Location of NSM-CFRP	Amount of NSM-CFRP	Specimen Designation
Control	N.A.	N.A.	N.A.	N.A.	Solid
	100x100	N.A.	N.A.	N.A.	D-NS
Strengthened	100x100	STM-I	Crossing bottom chord	One strip ($A_{f,tie}$= 75 mm^2)	D-I-1S
				Two strips ($A_{f,tie}$= 150 mm^2)	D-I-2S
	100x100	STM-II	Crossing top chord	One strip ($A_{f,tie}$= 75 mm^2)	D-II-1S
				Two strips ($A_{f,tie}$= 150 mm^2)	D-II-2S
	100x100	STM-III	Crossing top and bottom chords	One strip ($A_{f,tie}$= 75 mm^2)	D-III-1S
				Two strips ($A_{f,tie}$= 150 mm^2)	D-III-2S

$A_{f,tie}$ = area of CFRP per tie

4.3 Details of Test Specimens

The geometry and details of reinforcement of test specimens are shown in Figure 4.1. All test specimens were similar in terms of dimensions and internal steel reinforcement. The beams were 150 mm wide, 500 mm deep, and 2700 mm long. The effective span was 2100 mm, while 300 mm from each side was left free for the purpose of handling the beam and providing a development length for the bottom

steel reinforcement. The dimensions of the beams were decided in a way to ensure that they could be fabricated and tested in the laboratory. Four No.16 (16 mm diameter) ribbed steel bars were placed in two layers where their centroid was located at a depth of 450 mm measured from the top surface of the beam. No web reinforcement was provided along the effective beam span. This configuration of steel reinforcement grants that the beam failure mode is governed by shear failure. Two No.8 (8 mm diameter) top steel bars in addition to vertical steel stirrups of No. 8 with 75 mm spacing were placed at the ends outside the test region. Small and large stirrups were used as shown in Figure 4.1. The small stirrups surrounded the bottom steel bars and the larger stirrups surrounded the bottom and the top steel bars. The top steel bars were used as hangers. The purpose of the steel stirrups outside the test region was to provide confinement to the bottom steel bars and prevent slippage during testing. The beams with cutouts had a square opening of 100 x 100 mm at each shear span. The center of each opening was located at the mid-height of the beam (250 mm below the top surface) and at the middle of shear span (200 mm away from the support). This was done in an effort to induce an extreme discontinuity that can fully interrupt the natural load path.

Six deep beam specimens with openings were strengthened by NSM-CFRP strengthening technique around the D-regions in three different schemes. The NSM-CFRP strips represented the diagonal ties in the shear spans of the STMs developed in Chapter 3, however, they were extended beyond the length of ties of the STMs to provide development length as an anchorage for CFRP strips. As shown in Figure 4.2, STM-I included one or two diagonal NSM-CFRP strips in the bottom chord below the opening. STM-II included one or two diagonal NSM-CFRP strips in the

top chord above the opening. STM-III included one or two diagonal NSM-CFRP strips in the top and bottom chords.

(a) Solid beam

(b) Beam with opening

(c) Section A-A

(d) Section B-B
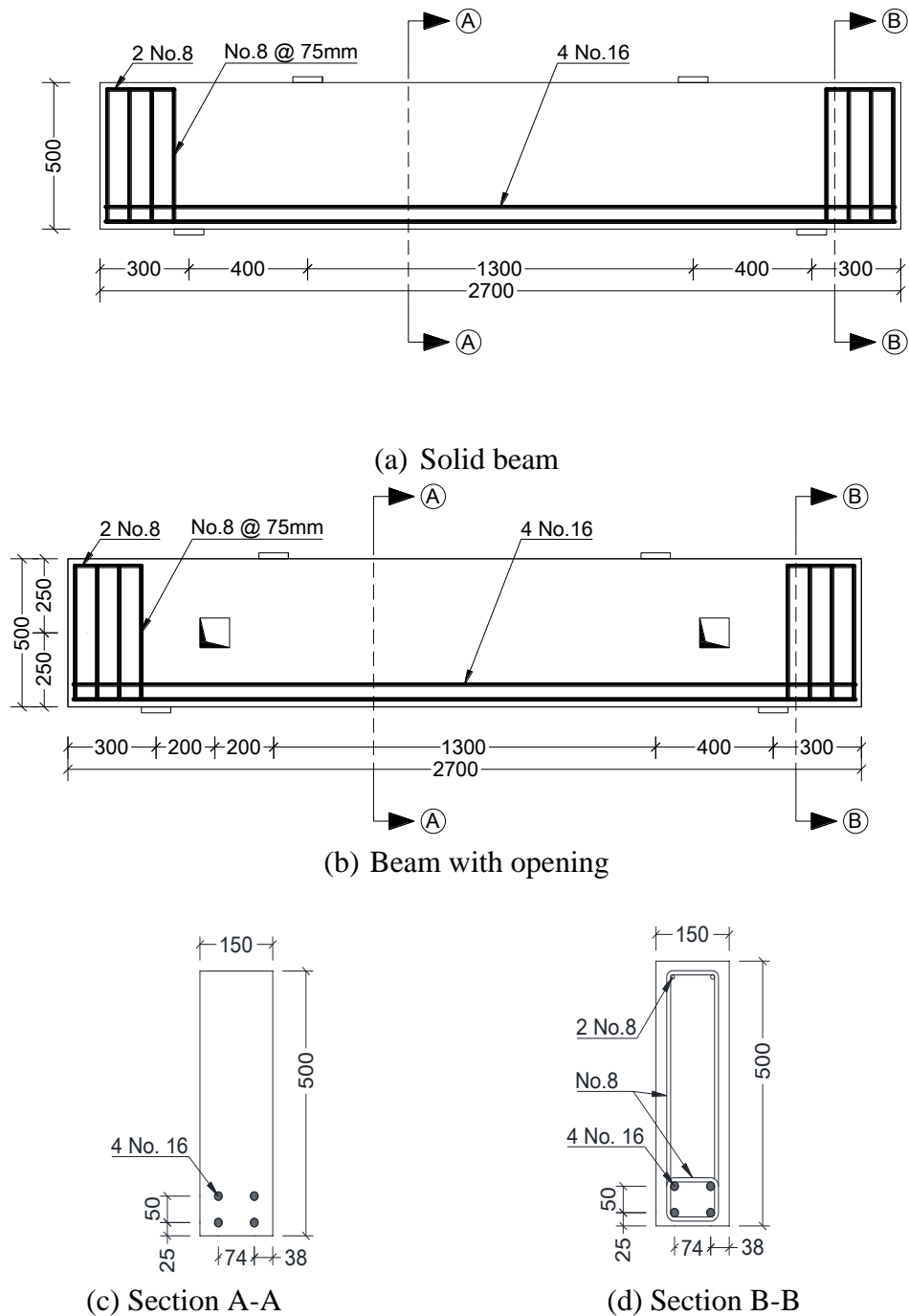
Figure 4.1: Dimensions and reinforcement details of test specimens

(a) STM-I

(b) STM- II

(c) STM-III
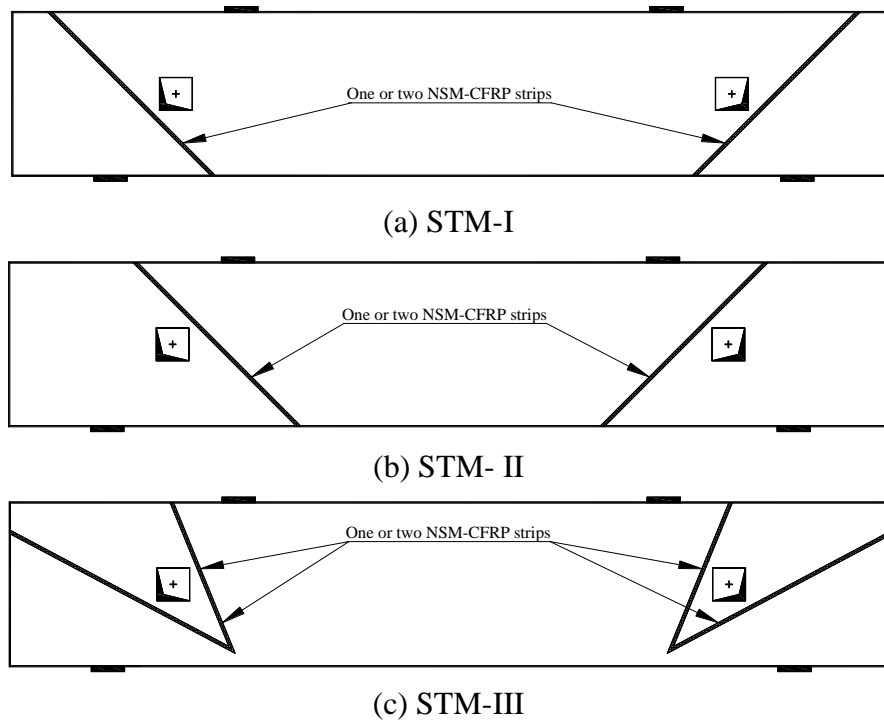
Figure 4.2: Strengthening schemes

4.4 Specimens Fabrication

Wooden forms were assembled using 18 mm plywood sheets as shown in Figure 4.3 (a). Wooden boxes were fixed inside formworks at proper locations to create the openings. The reinforcement steel bars for each beam were cut and assembled as one steel cage that included the bottom longitudinal reinforcement along the beam length plus the vertical stirrups and steel hangers at the end outside the test region. Figure 4.3 (b) shows the steel cages.

Prior to the installation of steel cages inside the forms, five strain gauges of 5 mm gauge length were attached on one bottom steel bar at midspan and at distances 100, 200, 300, and 400 mm away from the center of the support. Figure 4.4 shows the locations of strain gauges. The procedures used to attach strain gauges to steel bars are shown in Figure 4.5 and summarized as the following:

1. Mark strain gauge location on the steel bar.

2. Flatten the surface by angle grinder.

3. Smoothen the surface by sandpaper.

4. Clean the surface by ethyl alcohol.

5. Bond the strain gauge on the steel bar by an adhesive and prevent contact between strain gauge wires and steel bar by wrapping insulating tape on steel bar.

6. Add protection layer against water on strain gauge by a coating tape (SB tape).

7. Wrap the whole area by an insulation tape for further protection.

After bonding of strain gauges to the steel bars, the steel cages were kept inside the laboratory at room temperature until the day of concrete casting to prevent any damages that might occur to the strain gauges.

(a) Wooden forms   (b) Steel cages
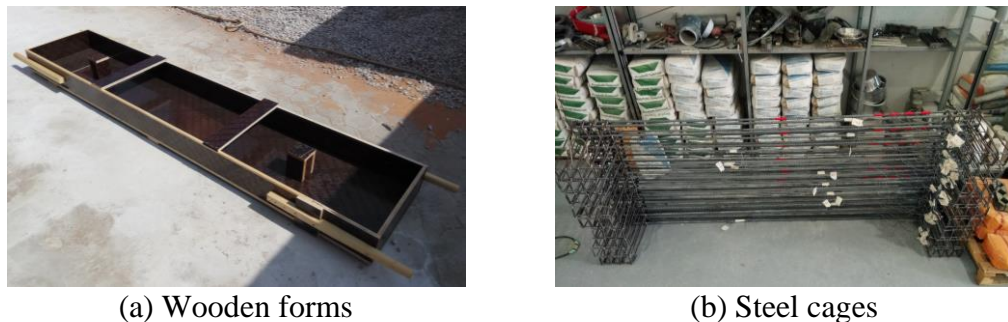
Figure 4.3: Specimens fabrication
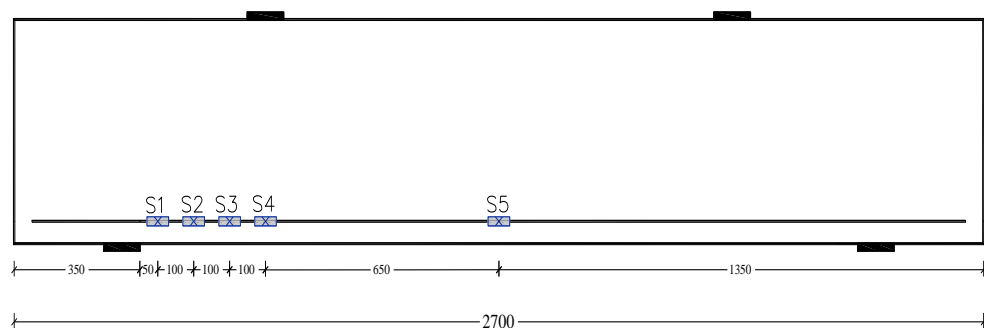
Figure 4.4: Steel strain gauges locations

(a) Surface preparation

(b) Strain gauge bonded on steel bar

(c) Coating tape

(d) Extra protection
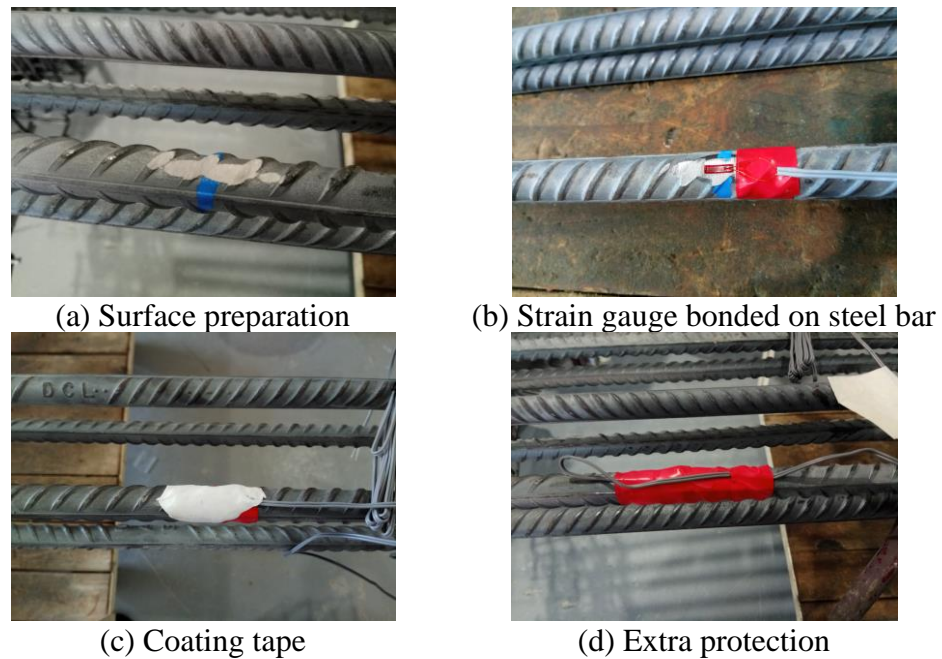
Figure 4.5: Installation of strain gauges

The casting process is summarized in Figure 4.6. The forms with the steel cages inside were placed in the open yard of the concrete laboratory. Ready-mix concrete was ordered from a local factory. The concrete was directly poured from the concrete mixer. Compaction was applied by a concrete vibrator, then the surface was smoothened by a finishing trowel. Five cube and ten cylinder were sampled for concrete compressive strength measurements. After hardening, all beam specimens, concrete cubes and cylinders were covered by wet burlap and polyethylene sheets. Water curing was applied for seven consecutive days. After 28 days, the forms were removed. Then, NSM-CFRP strengthening was applied on the specimens.

(a) Casting area

(b) Ready-mix concrete

(c) Concrete pouring and vibration
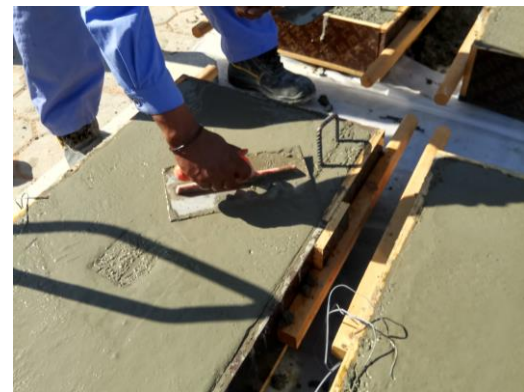
(d) Surface smoothing

(e) Burlap

(f) Polyethene sheets above burlap

Figure 4.6: Casting process

4.5 Material Properties

4.5.1 Concrete

The constituent materials of the ready-mix concrete were: Ordinary Portland Cement (OPC), two grades of coarse aggregates with nominal maximum size of 10 and 20 mm, fine aggregates with a combination of dune sand and crushed sand, tap water, and a high range superplasticizer. Concrete mixture proportions are presented in Table 4.2. To measure the concrete compressive strength, five cubes of 150 x 150 mm and five cylinders of 150 mm diameter and 300 mm height were tested under compression. Another five cylinders were used to determine the splitting tensile strength. The tests were conducted before testing the deep beams. The concrete strength test results are given in Table 4.3. The cube and cylinder compressive strengths were on average 48 and 40 MPa with a corresponding standard deviations of 2.8 and 1.4 MPa, respectively. The splitting strength was on average 3.3 MPa with a standard deviation of 0.3 MPa.

Table 4.2: Concrete mixture proportions

	Cement	Coarse aggregates		Fine aggregates		Water	Admixture (superplasticizer)
		10 mm	20 mm	Dune sand	Crushed sand		
Density (kg/m^3)	3150	2720	2720	2640	2660	1000	1200
Ratio by weight	1	0.96	1.95	0.61	1.59	0.45	0.01

Table 4.3: Concrete strength testing results

Specimen	Cube compressive strength f_{cu} (MPa)	Cylinder compressive strength f'_c (MPa)	Tensile splitting strength f_{ct} (MPa)
1	44	40	3.4
2	47	40	3.8
3	47	39	3.2
4	50	42	3.0
5	51	41	3.4
Average	48 ± 2.8	40 ± 1.4	3.3 ± 0.3

4.5.2 Reinforcement Steel

Tensile test was conducted on three random samples of steel No.16. Table 4.4 shows the test results. The average yield and ultimate strengths were 544 MPa and 657 MPa, respectively.

Table 4.4: Steel tensile test results

Specimen	Yield strength (MPa)	Ultimate strength (MPa)
1	542	657
2	550	659
3	541	656
Average	544 ± 5	657 ± 2

4.5.3 CFRP Composites

CFRP composite strips were used as NSM reinforcement around the opening. The cross-sectional dimension of the strips was 2.5 x 15 mm (37.5 mm^2). The modulus of elasticity was 165 GPa, the tensile strength was 3100 MPa and the ultimate strain was 0.019 (data was obtained from manufacturer). The CFRP strips

were installed inside grooves on the concrete's surface. Then, bonded to the sides of the groove using a thixotropic epoxy adhesive (Sikadur 30 LP®).

(a) Thickness   (b) Width
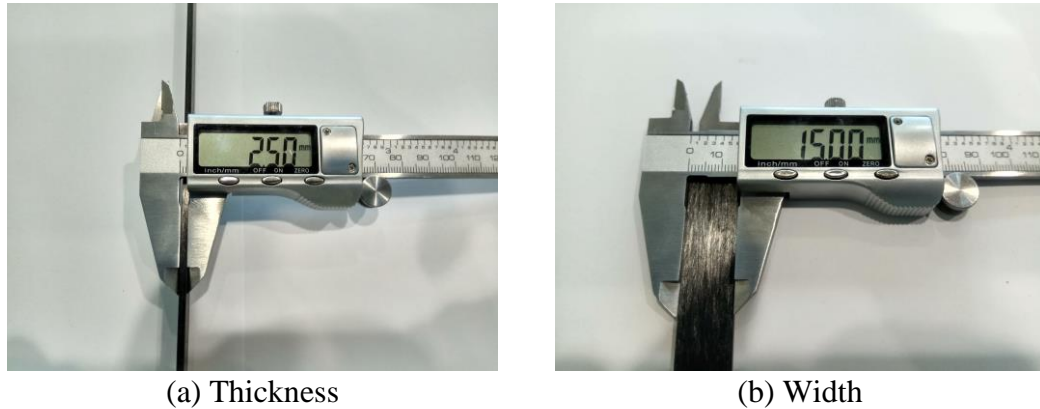
Figure 4.7: CFRP strip cross-sectional dimensions

4.6 Strengthening Technique

The CFRP materials were supplied by the manufacturer as a roll. The CFRP was cut into strips by a saw at certain lengths as required by each NSM strengthening model. A strain gauge of 5 mm long was boned at the closest point to the opening on each CFRP strip. Figure 4.8 shows the positions of strain gauges glued on FRP strips and the designation for each strain gauge. The presented strain gauges in Figure 4.8 are in the east shear span. Therefore, a letter E was added to the designation of the strain gauges shown in this figure. For the strain gauges in the west shear span the letter E was replaced by the letter W. To bond a strain gauge, the surface of the CFRP was first cleaned by ethyl alcohol. After that, the strain gauge was glued on the CFRP strip. Two pieces of insulating tape were attached above and below strain gauge naked wires to ensure that they were not connected with the CFRP. Figure 4.9 presents the prepared CFRP strips.

(a) D-I-1S

(b) D-I-2S

(c) D-II-1S

(d) D-II-2S

(e) D-III-1S

(f) D-III-2S
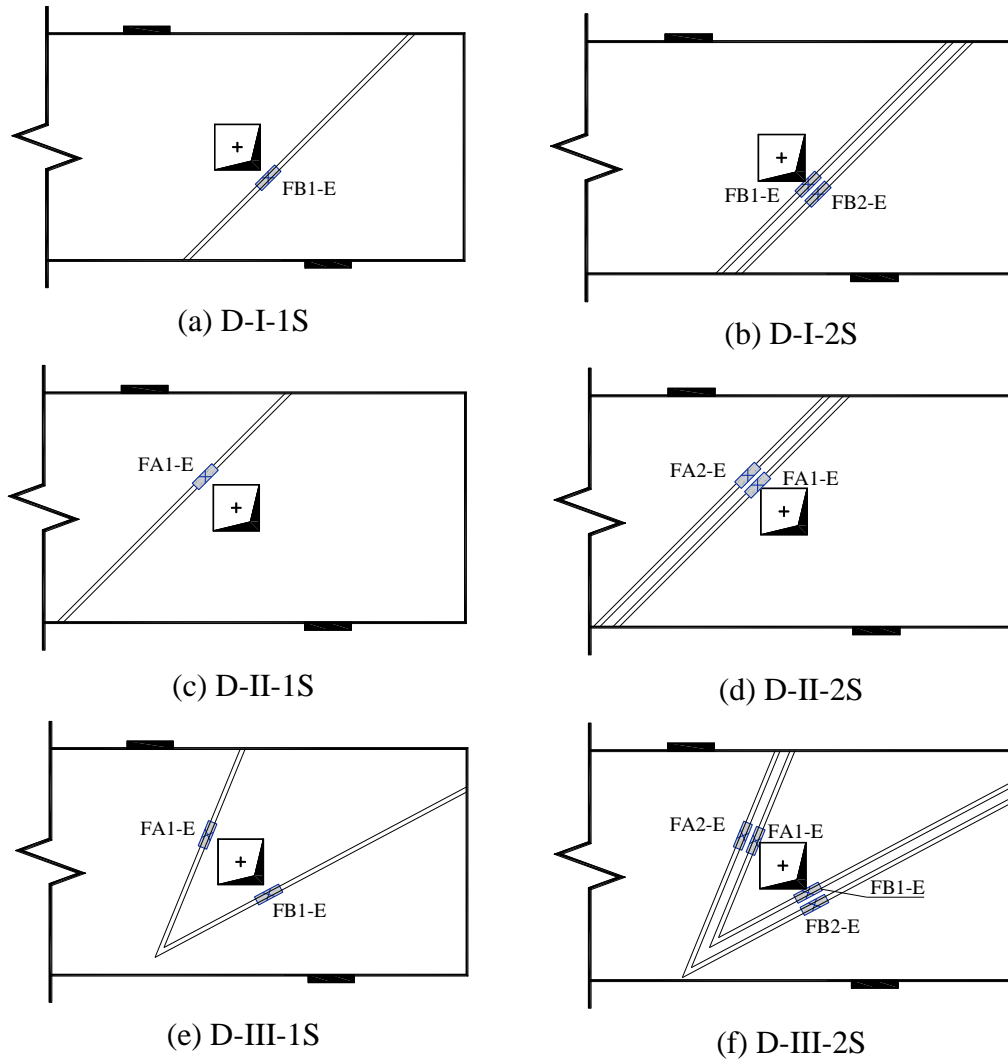
Figure 4.8: Strain gauges locations on FRP

(a) Strain gauge attached on CFRP strip

(b) CFRP strips

Figure 4.9: CFRP preparation

NSM strengthening was done in two stages. First, it was applied on one surface. Then the beams were flipped, and the strengthening was applied on the second surface. The NSM locations were marked on the surface of the beams. Grooves were cut along the marks by a slitting machine (Hilti®DC-SE20) as shown in Figure 4.10(a). The slitting machine was used along with vacuum cleaner as recommended by the manufacturer to remove the dust. The groove size was 10 x 24 mm. The size was in accordance with ACI 440.2R-08 [37]. The code specifies that the groove width and depth should be at least 3 a_b and 1.5 b_b respectively, where a_b is the smallest cross-sectional dimension and b_b is the larger cross-sectional dimension of the CFRP strip. Groove arrangements are shown in Figure 4.11. Epoxy adhesive was prepared and placed in the grooves by a trowel before placing the CFRP reinforcement. The grooves were totally filled by epoxy to make sure that CFRP strips were totally surrounded by epoxy. CFRP plates were then inserted in the grooves and the extra epoxy was removed.

(a) Groove cutting   (b) Epoxy filling   (c) CFRP strip insertion

Figure 4.10: Strengthening methodology

(a) D-I-1S

(b) D-I-2S

(c) D-II-1S

(d) D-II-2S

(e) D-III-1S

(f) D-III-2S
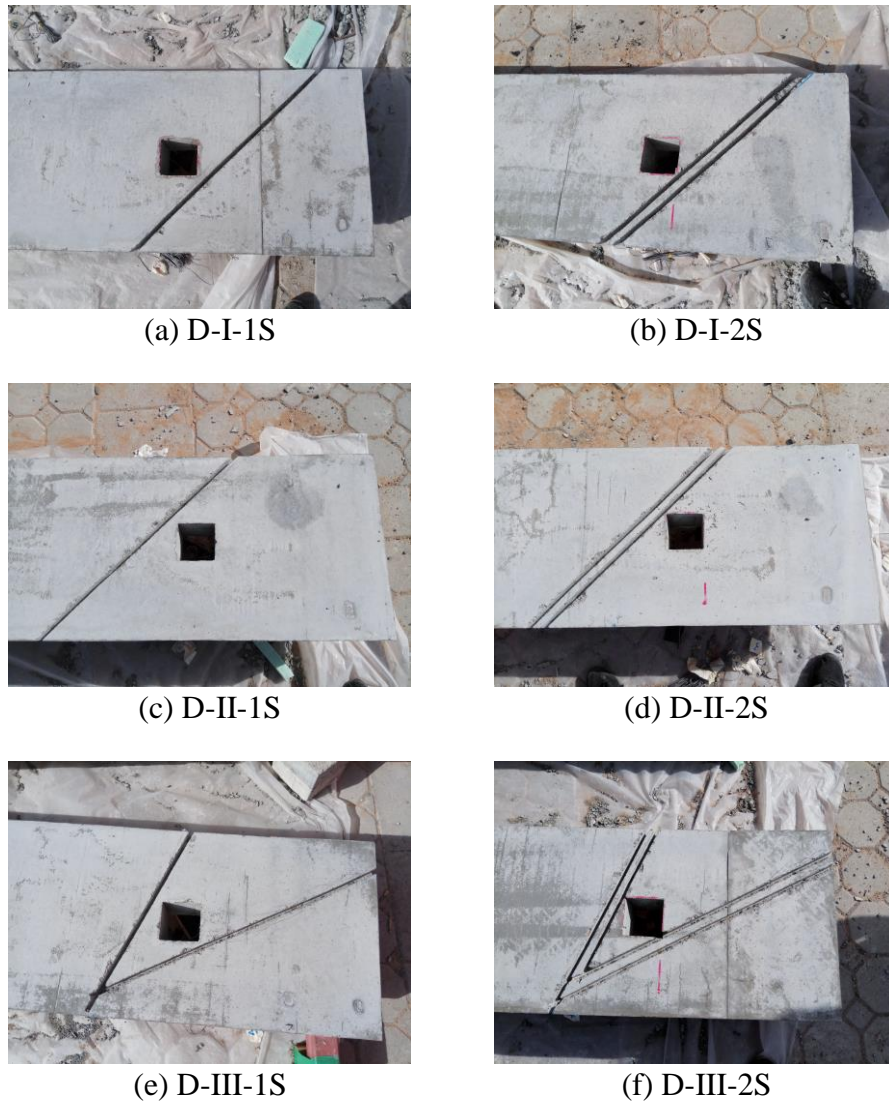
Figure 4.11: Grooves arrangements

4.7 Instrumentations and Testing

The test specimens were tested under four-point bending until failure. The specimens were placed on two supports that were 2100 mm apart from each other. The load was applied on two points 1300 mm apart at the top surface by two MTS actuators. Initially, the tests were conducted under load-control at rate of 0.5 kN/sec to ensure that both actuators apply equal load to the beam during test. At approximately 75% of the theoretical load capacity, the load was applied at a

displacement-control at a rate of 0.6 mm/min. This was done for the purpose of safety to avoid collapse of the beam at the ultimate load and to capture the post-peak response if exhibited by any specimen. Four bearing steel plates (100 x 150 x 20 mm) were placed below loading points and above supports to transfer the load and prevent concertation of stresses. There was a gap between the end of the actuators and the top surface of the beam. As such, a rigid steel short column was fabricated and installed at the bottom of each actuator to transfer load to the beam. The applied loads were recorded by load cells of 500 kN capacity which were placed between the steel plates on the top surface of the beam and the rigid steel columns connected to the actuators. A linear variable differential transducer (LVDT) was placed below the beam at the midspan to measure the deflection. Sixty (60) mm strain gauges were bonded to the concrete surface at certain locations to measure the concrete strains (Figure 4.12). All measuring tools including load cells, LVDT, and strain gauges were connected to one data acquisition system to record all readings simultaneously. Figure 4.13 shows the test setup. The side surfaces of beams were painted white prior to testing to visualize the cracks. Cracks developed during testing were marked on the surface and the corresponding load value was recorded and written beside each mark.

(a) Solid

(b) D-NS
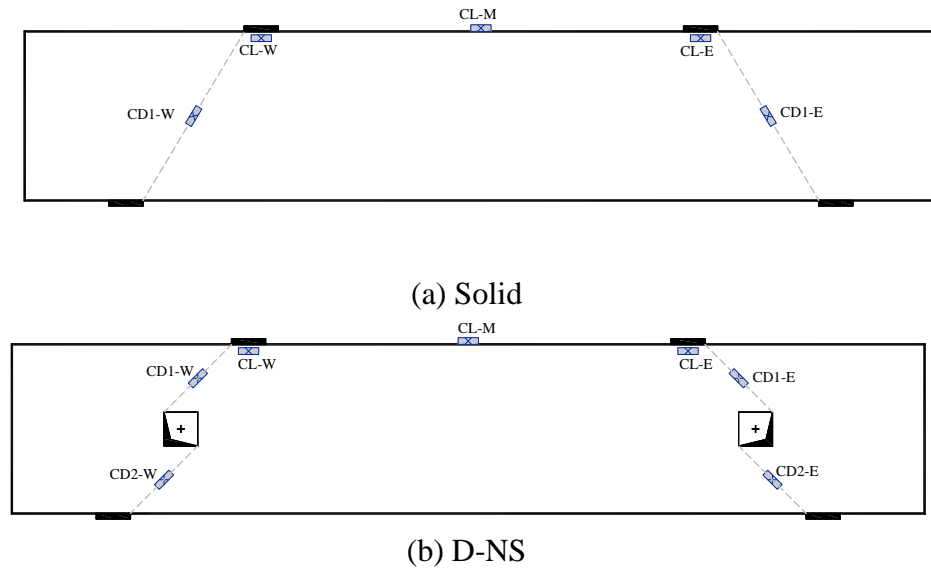
Figure 4.12: Concrete strain gauges positions and designations

4.8 Summary

This chapter illustrated the details of experimental program including the test specimens, strengthening technique, test setup, and instrumentations. The experimental results and the findings will be presented in the following chapter.
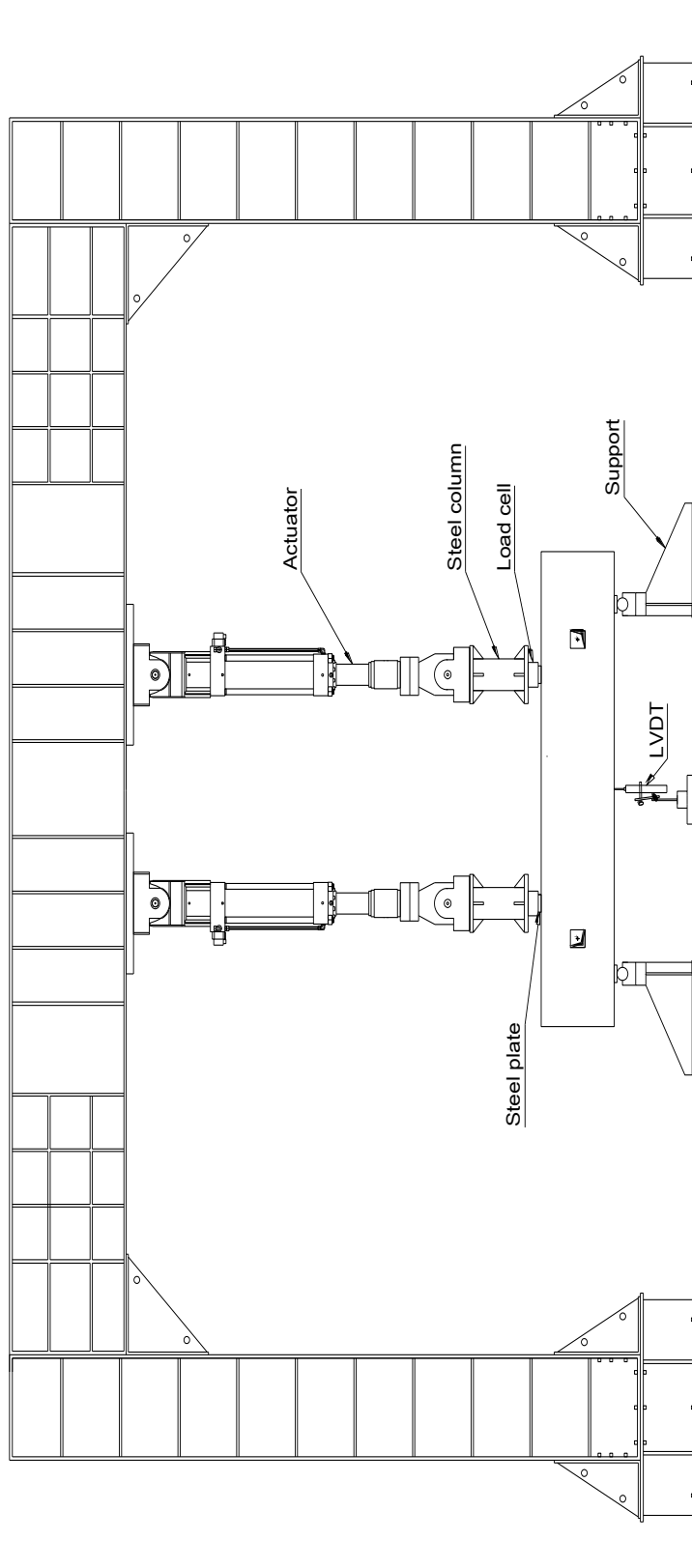
Figure 4.13: Test setup

Chapter 5: Experimental Results

5.1 Introduction

The experimental test results of eight deep beam specimens are presented in this chapter. The testing program consisted of two control unstrengthened concrete deep beams: a solid beam and a beam with a discontinuity in each shear span. The other six specimens were strengthened around the discontinuity regions. Crack patterns were marked during testing and the failure mode was recorded. Several measurements were taken during testing including: applied load, deflection at midspan and strains in CFRP strips, steel, and concrete.

5.2 Load-Deflection Response

The load versus the deflection is plotted in Figure 5.1 to Figure 5.4 for all test specimens. The load value presents the total applied loads by the two actuators. The deflection is the measured displacement of the bottom surface of the beam at midspan.

5.2.1 Unstrengthened Specimens

For the solid specimen, the load-deflection response consists of two linear segments (Figure 5.1). The first segment was steeper than the other segment. The slope was changed at about 100 kN. This possibly denotes a formation of flexure cracks. However, the flexural cracks were not visible at this stage. A slight change in the slop occurred at 270 kN due to initiation of the first shear crack. The load kept increasing until reaching the ultimate load of 565 kN which was attained at deflection of 4.4 mm. No post-peak response was captured due to the nature of the

failure where the beam was failed suddenly and did not exhibit any additional deflection.

The response of specimen D-NS started with a linear relationship between the load and the deflection (Figure 5.1). The response was identical to that of the solid specimen up to a load value of approximately 100 kN. The change in response occurred because of the formation of first shear crack. In the post-cracking stage, the specimen D-NS exhibited a higher rate of deflection increase and a reduced flexural stiffness compared with that of the solid specimen. At a load value of 200 kN, there was a sudden increase in the deflection without an increase in the load. The deflection value jumped from 1.7 to 1.9 mm. This was attributed to the formation of a vertical crack in the outer boundary of the top chord. After that, the deflection continued to increase linearly with the load until the load reached approximately 300 kN where a new shear crack developed in the bottom chord. The beam failed shortly after formation of this crack with a maximum load carrying capacity of 338 kN and a corresponding deflection of 4 mm.
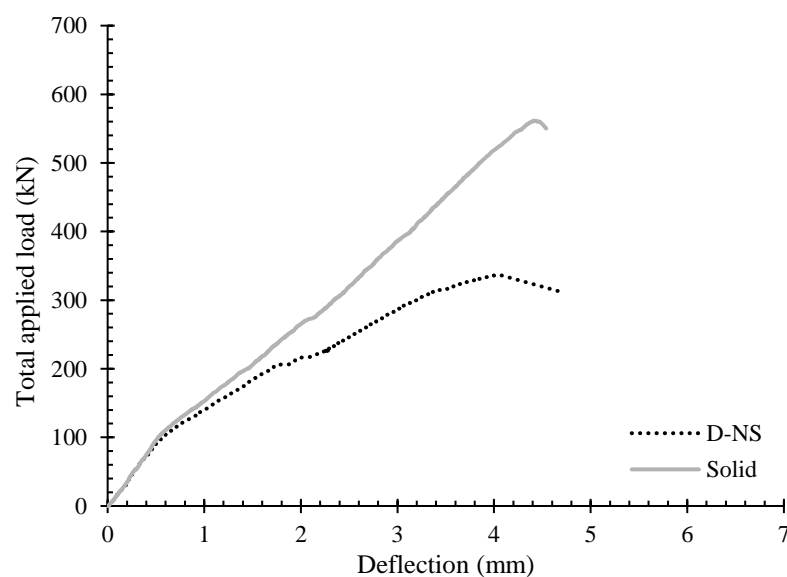
Figure 5.1: Load-deflection response of the unstrengthened specimens

5.2.2 Strengthened Specimens – Scheme STM I

Figure 5.2 shows the load-deflection response of specimens D-I-1S and D-I-2S, in addition to that of the solid specimen for the purpose of comparison. Specimens D-I-1S and D-I-2S showed a bilinear response. The change in the slope of the load-deflection response occurred at approximately 115 kN. The flexural stiffness of specimen D-I-2S matched with that of the solid specimen, whereas the stiffness of D-I-1S was slightly lower. The ultimate load of specimens D-I-1S and D-I-2S were 528 and 658 kN and the corresponding deflections at peak load were 4.5 and 5.6 mm, respectively.
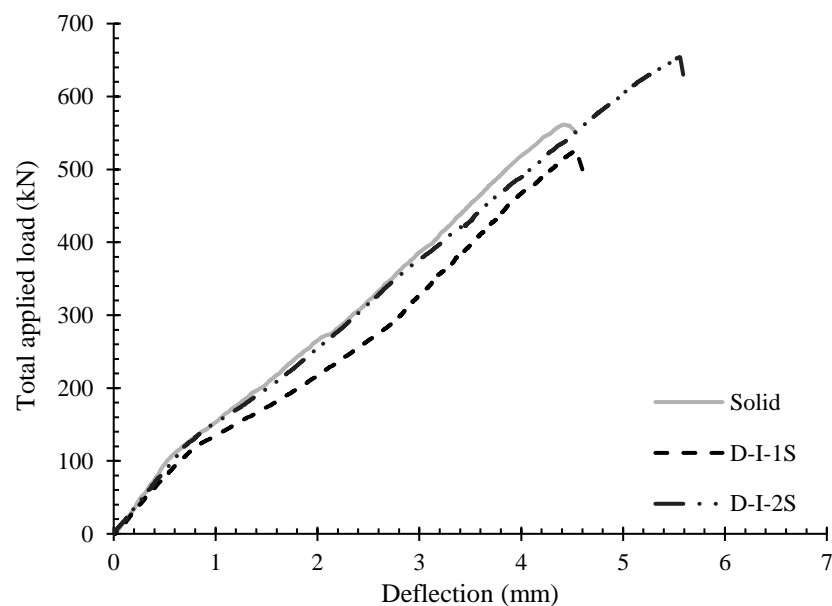
Figure 5.2: Load-deflection response of control and STM I specimens

5.2.3 Strengthened Specimens – Scheme STM II

Figure 5.3 presents the load-deflection responses of the two specimens D-II-1S and D-II-2S in addition to that of the solid specimen. The response of specimen D-II-1S was bilinear with a slight change in slope at about 200 kN. The response of

specimen D-II-2S was also a bilinear, however, the slope changed at approximately 160 kN. This occurred when the first shear crack developed. The response of D-II-2S coincided with that of the solid specimen. Obviously, specimen D-II-1S with the lower amount of NSM-CFRP reinforcement exhibited higher deflections than those showed by D-II-2S with the greater amount of NSM-CFRP reinforcement. Specimens D-II-1S and D-II-2S reached their peak loads of 573 and 572 kN at deflection values of 6.1 and 4.7 mm, respectively.
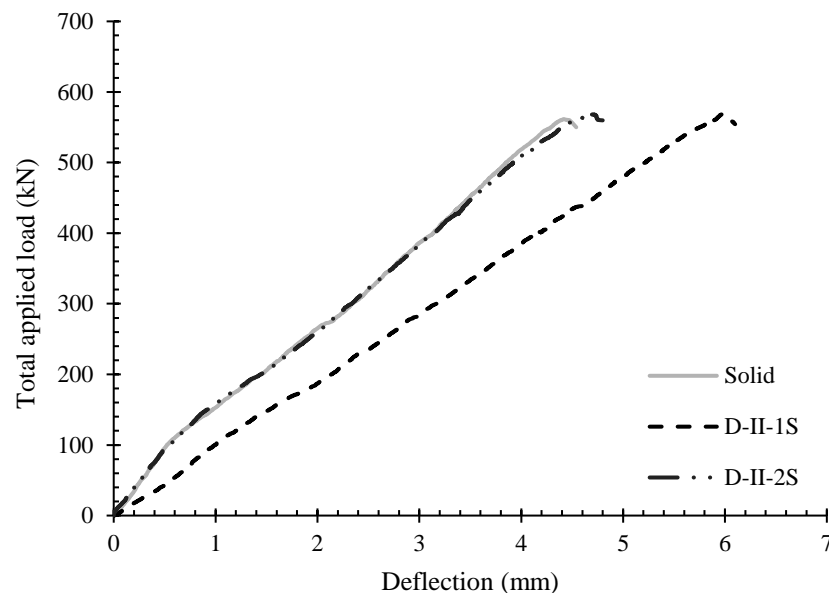
Figure 5.3: Load-deflection response of control and STM II specimens

5.2.4 Strengthened Specimens – Scheme STM III

The load-deflection response of specimens D-III-1S, D-III-2S and that of the solid specimen are presented in Figure 5.4. The load-deflection relationship was bilinear. The strengthened specimens had almost an identical response up to a load value of approximately 150 kN where the deflection started to increase at a higher rate. Due to the higher amount NSM-CFRP reinforcement in D-III-2S, the post-cracking stiffness was slightly higher than that of D-III-1S. Nevertheless, the

stiffness of the two strengthened specimens was slightly lower than that of the solid specimen. Specimens D-III-1S and D-III-2S failed at load values of 531 and 586 kN, respectively. The deflection of the two specimens at the failure was almost the same which was approximately 5 mm.
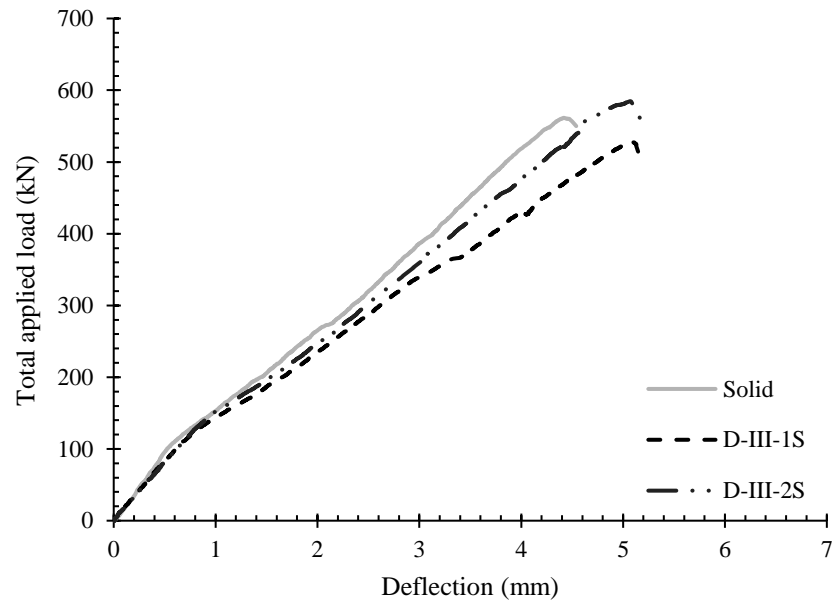
Figure 5.4: Load-deflection response of control and STM III specimens

5.3 Crack Pattern and Failure Mode

5.3.1 Unstrengthened Specimens

The crack pattern of the solid specimen is presented in Figure 5.5. Diagonal cracks in the shear spans near the support plates were started to appear at a total load of 270 kN. The first flexural crack was formed near the midspan when the load reached 300 kN. As the load was progressing, shear cracks propagated toward the loading points. In parallel, new flexural cracks were formed and existing flexural cracks extended vertically upward. Finally, the beam was failed in a shear compression mode of failure as crushing in concrete was formed at the tip of the

diagonal strut in the east shear span. In addition, a new shear crack was formed in the east shear span along the strut. The crushing area is shaded in Figure 5.5(a) and the diagonal failure crack was drawn in bold in the same Figure. The areas above the support plate in both shear spans were suspicious for concrete crushing, however, visual observation shows no crushing in those areas as there was no sign of crushing on the back side of the beam.
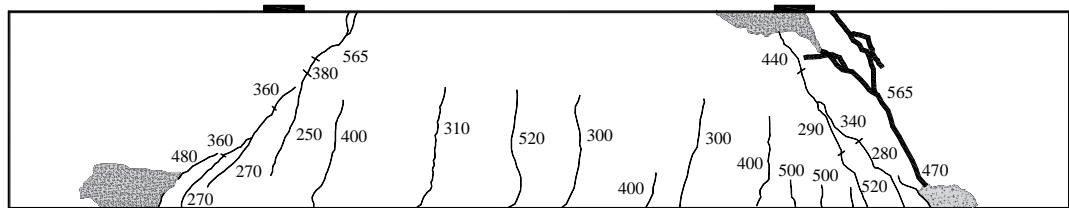
(a) schematic drawing of the crack pattern
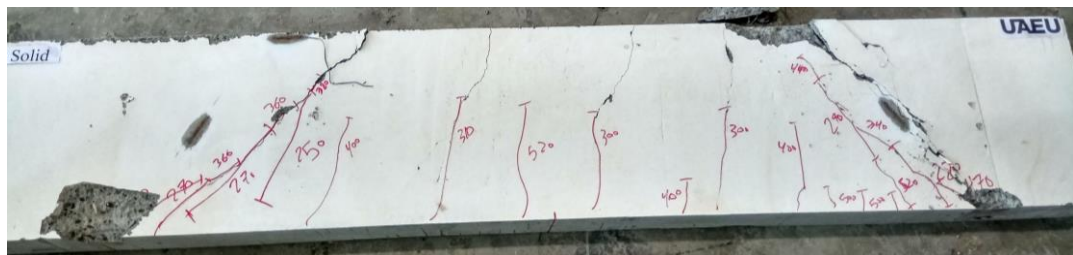
(b) picture of the beam at failure

(c) close view of the crack pattern

Figure 5.5: Crack pattern of the solid specimen

The crack pattern of specimen D-NS is illustrated in Figure 5.6. In the early stages, at 120 kN, a diagonal shear crack initiated at the bottom corner of the opening near the support. After a slight increase in the load, another shear crack was

developed at the opposite corner of the opening. At 200 kN, the formed cracks extended toward the loading and support plates, besides, a vertical crack was developed at the top chord of the beam approaching the top uncracked corner of the opening. After that, at a load of 250 kN, a small vertical crack was formed in the bottom chord below the loading point. The diagonal crack in the bottom chord reached support plate when the load reached 270 kN. The diagonal crack at the top chord almost reached the loading plate at 280 kN. At a load value of 300 kN, a new shear crack formed in the west side of the beam. The crack was initiated from the bottom inner edge of the opening and merged with the existing cracks. Then, the failure occurred shortly at a load value of 338 kN in a diagonal tension mode of failure. Remarkably, no cracks were observed in the constant moment region.

(a) schematic drawing of the crack pattern

(b) picture of the beam at failure

Figure 5.6: Crack pattern of specimen D-NS

(c) close view of the crack pattern

Figure 5.6: Crack pattern of specimen D-NS (Continued)

5.3.2 Strengthened Specimens – Scheme STM I

Figure 5.7 shows the crack pattern of specimen D-I-1S specimen. The blue lines present the location of NSM-CFRP reinforcements. When the load reached 190 kN, a diagonal crack crossing the center of the opening in the west shear span initiated. A similar diagonal crack initiated in the east shear span at 240 kN. The cracks kept extending toward bearing areas as the load was increasing. At 300 kN, a vertical crack at the outer boundary of the top chord was generated. Four flexural cracks appeared in the constant moment region at 400 kN of load. A new shear crack generated in the top chord of the west shear span at load value of 528 kN. The crack extended between the top corners of the opening and the load plate. The newly generated crack caused splitting in the top chord as mode of failure. Local crushing of concrete was observed above the west support plate and below the east load plate. The crack causing failure was drawn in bold in Figure 5.7(a) to indicate the failure.

(a) schematic drawing of the crack pattern

(b) picture of the beam at failure

(c) close view of the crack pattern

Figure 5.7: Crack pattern of specimen D-I-1S

The crack pattern of specimen D-I-2S is shown in Figure 5.8. The first shear crack was observed at a load value of 180 kN. It was a diagonal shear crack in the shear span initiated from top corner of the opening nearest to the load plate. The crack kept approaching the loading point as the load increased. When the load reached 240 kN, a similar crack formed in the east shear span. As the load increased, diagonal cracks developed in the bottom chord of both shear spans. Several flexural cracks developed in the constant moment region at a load value of 340 kN. At a load of 420 kN, a vertical crack was formed at the outer end of the top chord. A new diagonal crack developed in the west shear span at 630 kN. The failure occurred suddenly in the east shear span when the load reached 658 kN. The failure occurred

by crushing the inner diagonal strut near the opening. The shaded area in Figure 5.8 (a) indicates the crushing location. The failure caused a diagonal crack along the strut. A horizontal shear-tension crack was observed at the level of the longitudinal steel at the onset of failure which caused spalling of the cover.

(a) schematic drawing of the crack pattern

(b) picture of the beam at failure

(c) close view of the crack pattern

Figure 5.8: Crack pattern of specimen D-I-2S

5.3.3 Strengthened Specimens – Scheme STM II

Figure 5.9 presents the cracking pattern of specimen D-II-1S after testing. The blue lines present the location of NSM-CFRP reinforcements. The first noticeable shear crack developed in the bottom chord of each shear span at 200 kN of load. The crack initiated from the bottom corner of the opening closer to the support

plate and approached the inner corner of the support plate. The crack extended over nearly 75% of bottom chord height. The crack reached the support plate at a load value of 400 kN. At 300 kN, a diagonal crack developed at the opposite corner of the opening. When the load reached 340 kN, a vertical crack at the outer boundary of the top chord formed. The crack extended from the top of the beam to the mid-height of the chord. At the same time, flexural cracks started to appear in the constant moment region. As the load progressed, the existing cracks extended and new shear cracks developed. At 570 kN, two independent splitting cracks developed in the top and bottom chord of the east shear span causing sudden failure of the beam (frame type mode of failure).
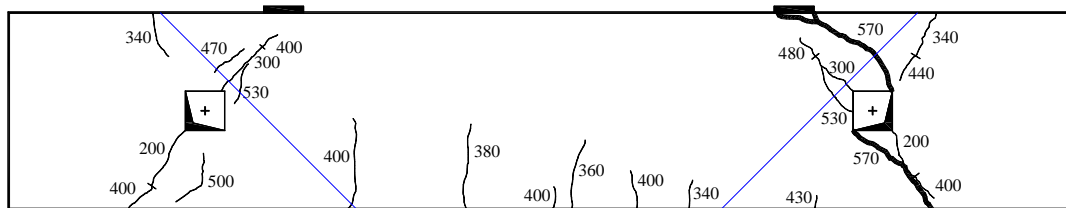
(a) schematic drawing of the crack pattern.

(b) picture of the beam at failure

Figure 5.9: Crack pattern of specimen D-II-1S
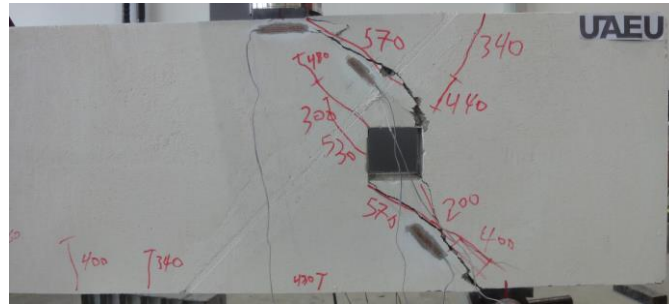
(c) close view of the crack pattern

Figure 5.9: Crack pattern of specimen D-II-1S (Continued)

The crack pattern of D-II-2S specimen is shown in Figure 5.10. Likewise specimen D-II-1S, the first visible shear crack was a diagonal crack initiated at 160 kN from the corner of the opening nearest to the support plate. The crack kept extending toward the support plate as the load increased. Few flexural cracks were formed in the constant moment region at a load value of 300 kN. The number of flexural cracks increased with the increase in the applied load. The cracks in the top chord of the shear span started to appear at a load value of 420 kN. One crack was inclined and initiated from the top inner corner of the opening, while the other crack was vertical and located at the outer boundary of the top chord. At a load value of 500 kN, new shear cracks developed in the top and bottom chords in each shear span. At 550 kN, the shear crack at the west bottom chord extended and reached the support plate. Eventually, the shear crack expanded causing a splitting mode of failure in the bottom chord at a load value of 572 kN.
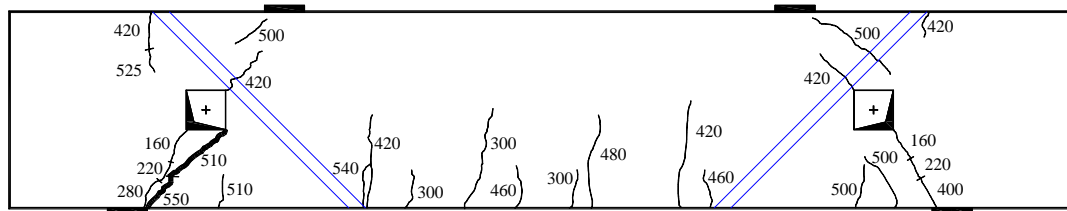
(a) schematic drawing of the crack pattern
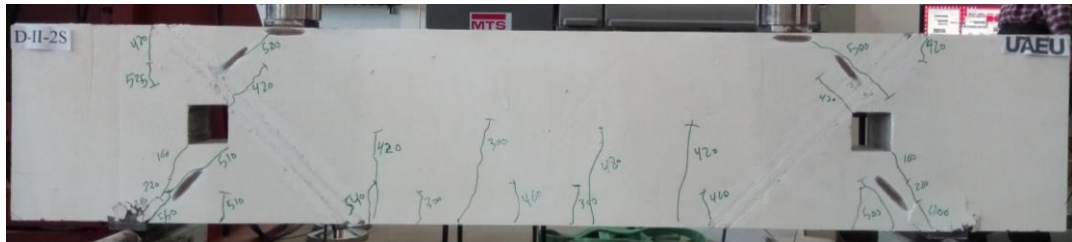
(b) picture of the beam at failure
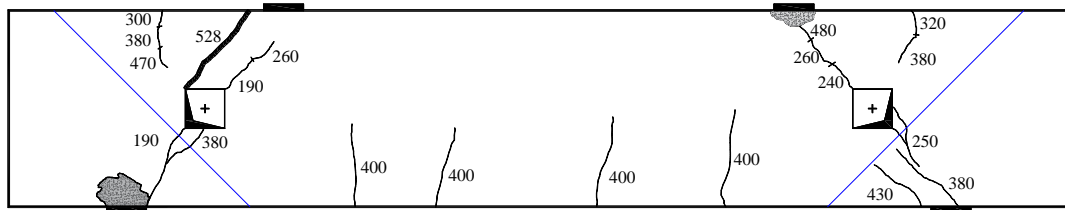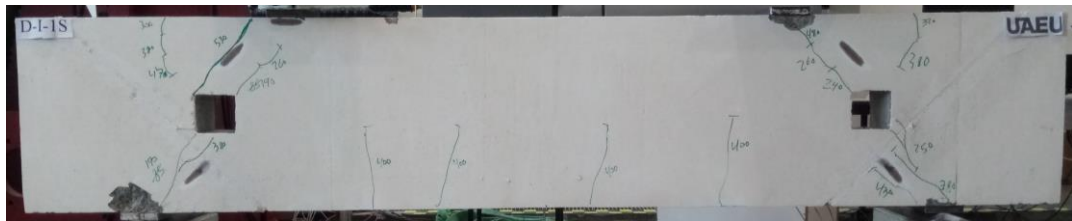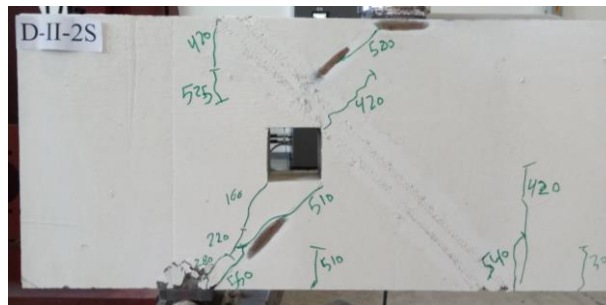

(c) lose view of the crack pattern

Figure 5.10: Crack pattern of specimen D-II-2S

5.3.4 Strengthened Specimens – Scheme STM III

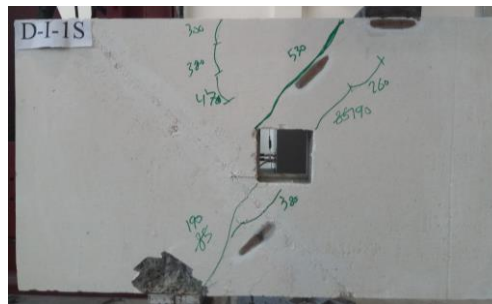Figure 5.11 presents the crack pattern of specimen D-III-1S. The blue lines present the location of NSM-CFRP reinforcements. The first visible crack formed at a load value of 260 kN. It was a shear crack in the bottom chord of the west shear span initiated from the nearest corner of the opening to the support plate. When the load reached 320 kN, cracks in the constant moment region started to appear. Then, at 340 kN, a shear crack developed in the west top chord. At 360 kN, a vertical crack formed in the east top chord above the support plate. As the load increased, the cracks in the shear spans extended and new cracks in the constant moment region

appeared. Prior to failure, a new crack initiated at the east top chord at a load value of 510 kN. At the onset of failure, the shear crack in the top chord expanded and extended to reach the load plate. In addition, a new shear crack developed in the bottom chord. The two cracks caused a splitting failure mode (frame type) in the east shear span at 531 kN.
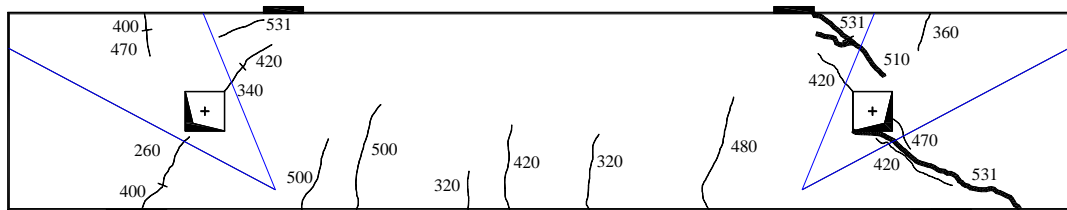
(a) schematic drawing of the crack pattern
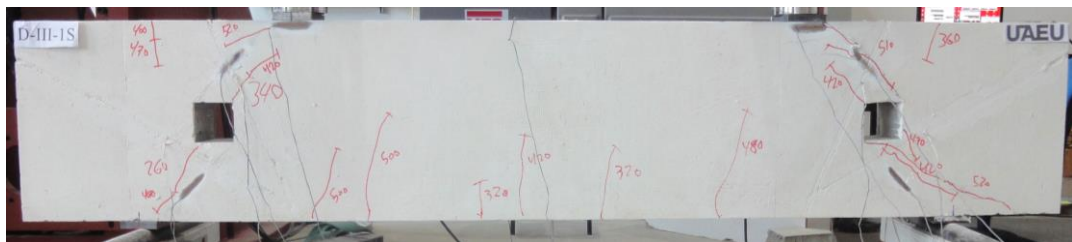
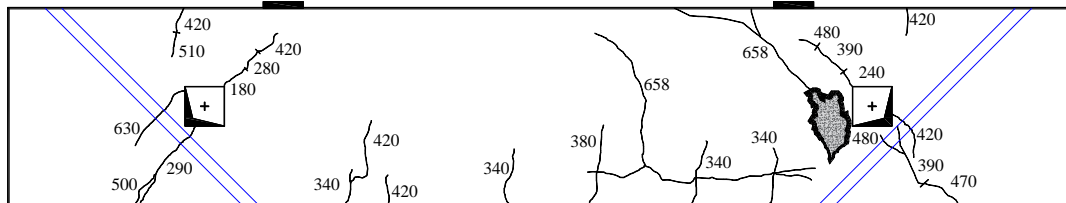(b) picture of the beam at failure
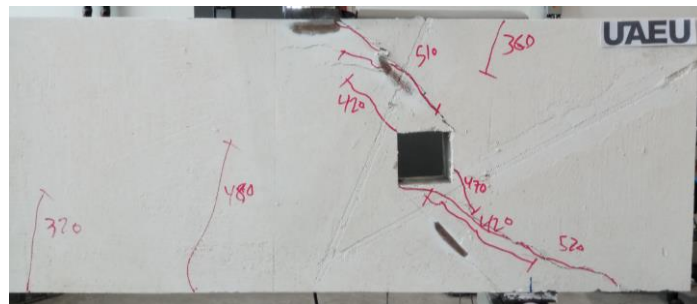
(c) close view of the crack pattern

Figure 5.11: Crack pattern of specimen D-III-1S

The crack pattern of specimen D-III-2S is shown in Figure 5.12. The first shear crack initiated from the inner edge of the west support plate at a load value of 420 kN. Flexural cracks started to appear at 480 kN. At a load value of 520 kN, a shear crack developed in the top chord of the west shear span initiated from the

corner of the opening near the loading plate. At 560 kN, a vertical crack at the top chord above the support plate generated. Up to this stage, all developed shear cracks were visible in the west shear span. However, several shear cracks were observed at the east bottom chord prior to failure at 580 kN. All cracks were very tiny and hard to be observed. This indicated that high amount of NSM-CFRP reinforcement in the shear spans was effective in controlling the growth of cracks. At a total load of 586 kN, the beam failed by crushing of the vertical strut in the top chord (Figure 5.12).
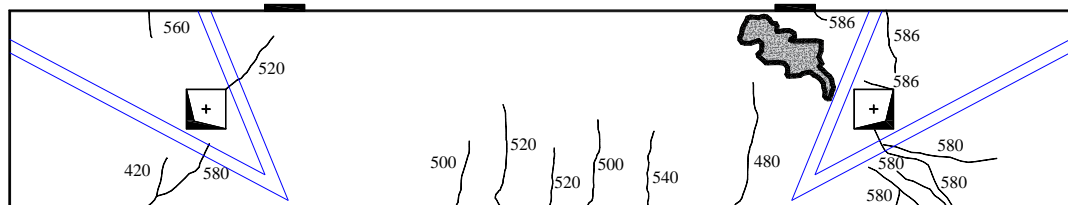
(a) schematic drawing of the crack pattern
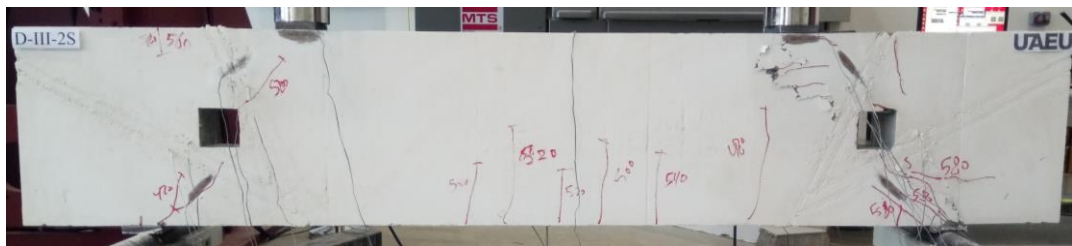
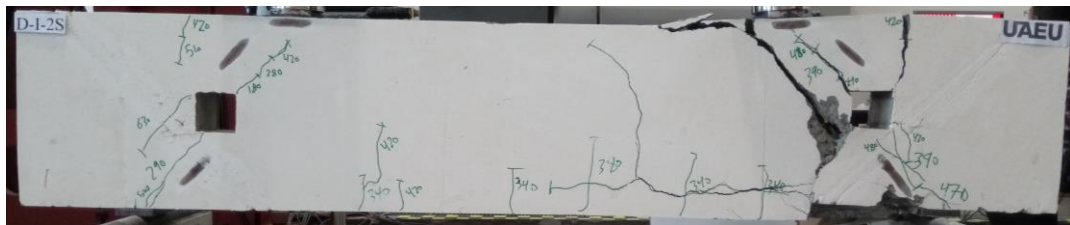(b) picture of the beam at failure

(c) close view of the crack pattern
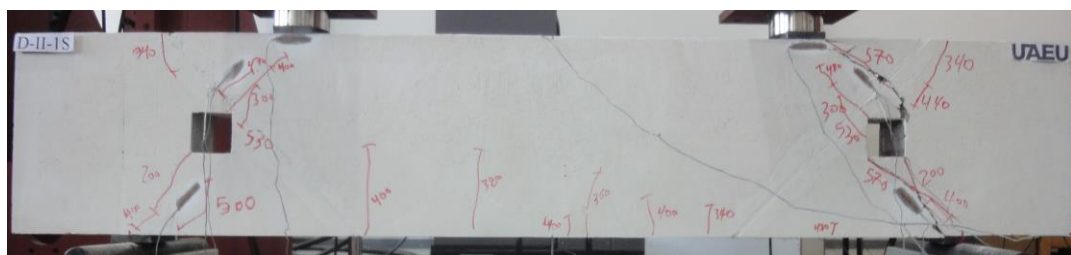
Figure 5.12: Crack pattern of specimen D-III-2S

5.4 Data Analysis

Table 5.1 shows a summary of the key results of all test specimens. For the solid specimen, the shear cracking load was approximately 48% of the ultimate load and it was attained at a midspan deflection of 2.0 mm. The solid specimen failed in shear compression mode of failure at an ultimate load of 565 kN and a deflection of 4.4 mm. The cracking load of specimen D-NS (120 kN) corresponded to 36% of the peak load. The observed failure mode was a diagonal tension and it took place at a deflection of 4.0 mm and a load of 338 kN. It is worth noting that creation an opening at the center of the shear spans resulted in changing the failure mode of the solid beam. In addition, the strength dropped by 40%. Nevertheless, the deflection at ultimate load was not significantly affected. The first visible crack in specimens D-I-1S and D-I-2S occurred at 36% and 27% of the peak loads, respectively. D-I-1S restored 93% of the solid beam's strength. The capacity of D-I-2S exceeded that of the solid beam by 16%. For specimens D-II-1S and D-II-2S, shear cracks initiated at 200 and 160 kN, respectively, which corresponded to 35% and 28% of their peak loads, respectively. The STM II-based strengthening scheme restored the load carrying capacity of the solid specimen. Both specimens (D-II-1S and D-II-2S) had the same ultimate load because they exhibited the same failure mode (diagonal splitting in the bottom chord). The shear cracks in specimens D-III-1S and D-III-2S initiated at load values of 260 and 420 kN, respectively, which corresponded to 49% and 72% of the peak loads, respectively. This indicated that the installation of NSM-CFRP in the top and bottom chords delayed the initiation of shear cracks .The strength of D-III-1S was 94% of that of the solid beam. The strength of D-III-2S was only 10% higher than that of D-III-1S.

Table 5.1: Summary of test results

Group	Specimen	Shear cracking stage		Ultimate stage		P_{max}/P_{Solid}	Strength gain[*]	Failure mode
		P_{cr} (kN)	Δ_{cr} (mm)	P_{max} (kN)	Δ_{peak} (mm)	(%)	(%)	
Control	Solid	270	2.0	565	4.4	-	-	Shear compression
	D-NS	120	0.8	338	4.0	60	-	Diagonal tension
Strengthened	D-I-1S	190	1.5	528	4.5	93	56	Diagonal splitting
	D-I-2S	180	1.3	658	5.6	116	95	Crushing of strut
	D-II-1S	200	2.2	573	6.1	101	70	Diagonal splitting
	D-II-2S	160	1.0	572	4.7	101	69	Diagonal splitting
	D-III-1S	260	2.3	531	5.1	94	57	Diagonal splitting
	D-III-2S	420	3.5	586	5.0	104	73	Crushing of strut

[*] With respect to D-NS specimen

5.5 Strain Measurements

5.5.1 Steel Strains

The strain in the main longitudinal steel reinforcement was measured at five points. The strain gauges were placed at 100, 200, 300, 400 and 1050 mm away from the center of the support plate. Table 5.2 reports the maximum measured strains in the longitudinal steel for all test specimens. No yielding in the steel was reported in all test specimens.

Figure 5.13 to Figure 5.16 show the measured readings of steel strains in the shear span at four different stages of loading: 25%, 50%, 75% and 100% of the peak load. Some readings were missing due to malfunction of the strain gauge before

testing. For all test specimens, the strain values increased in all locations as the load increased. All specimens exhibited almost a uniform steel strain profile within the shear span which confirmed the development of the deep beam action. For specimen D-II-1S, the strain was uniform in the first three stages with a slight drop in the strain located at a distance 400 mm from the support. This difference became more obvious as the load increased. At ultimate load, there was a sudden jump in the strain at the closest location to the support possibly due to a development of crack that crossed the strain gauge.

Table 5.2: Maximum measured strain in steel reinforcement

Specimen	$\varepsilon_{s,max}$ ($\mu\varepsilon$)	$\varepsilon_{s,max} / \varepsilon_y$ [*]
Solid	2179	80%
D-NS	1824	67%
D-I-1S	1778	65%
D-I-2S	2035	75%
D-II-1S	2668	98%
D-II-2S	1653	61%
D-III-1S	2099	77%
D-III-2S	1908	70%

[*] yield strain = 2720 $\mu\varepsilon$
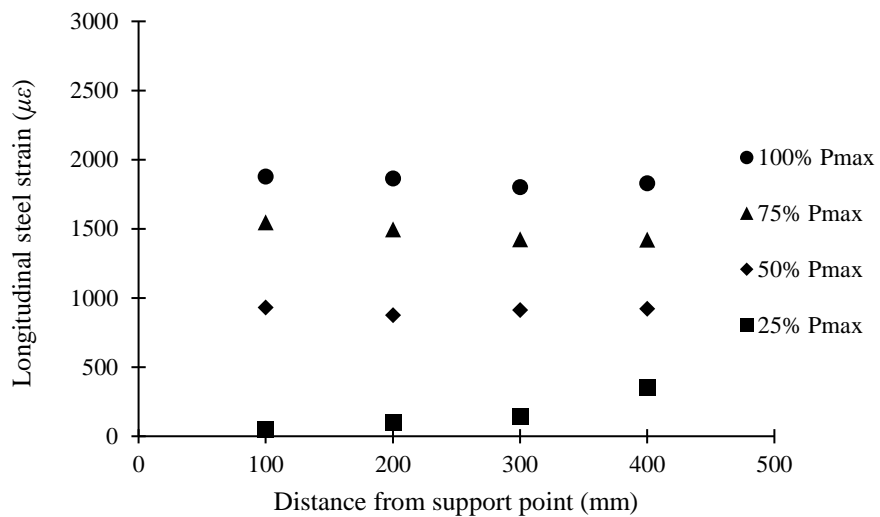
(a) Solid
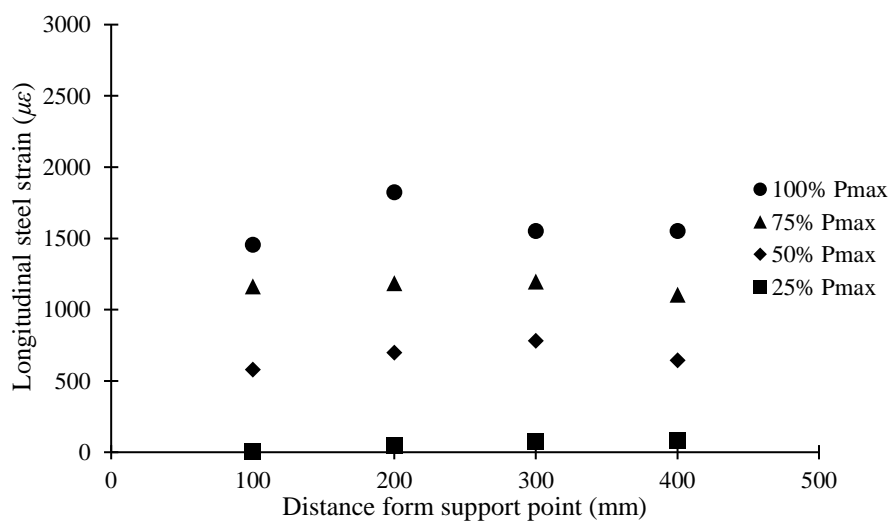
(b) D-NS

Figure 5.13: Steel strain profile of unstrengthened specimens
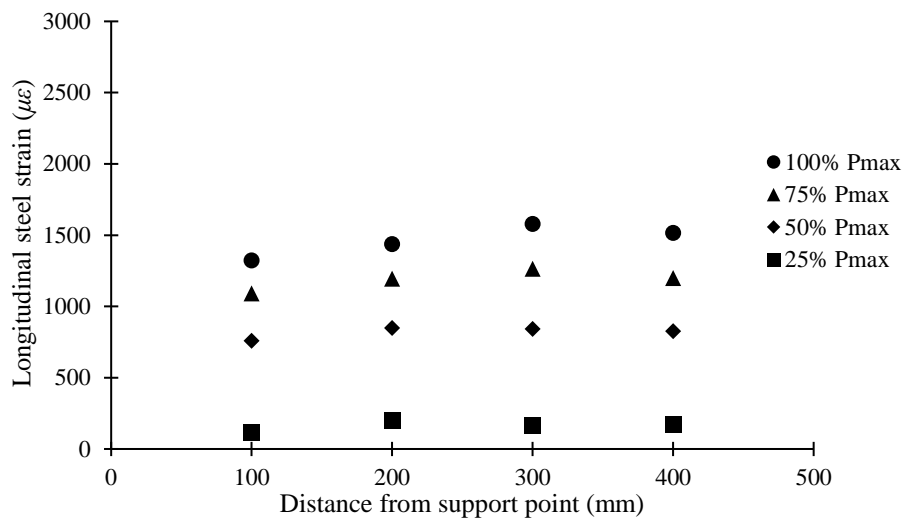
(a) D-I-1S
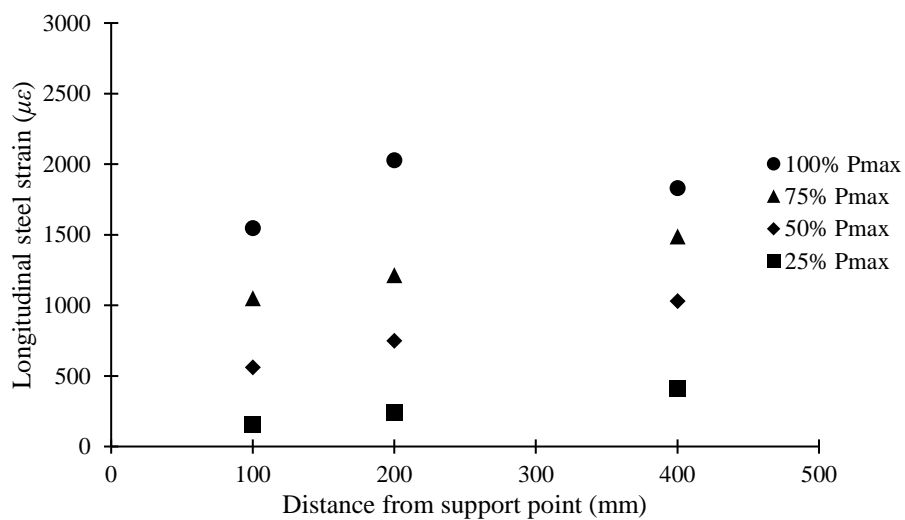
(b) D-I-2S

Figure 5.14: Steel strain profile of strengthened specimens – Scheme STM I
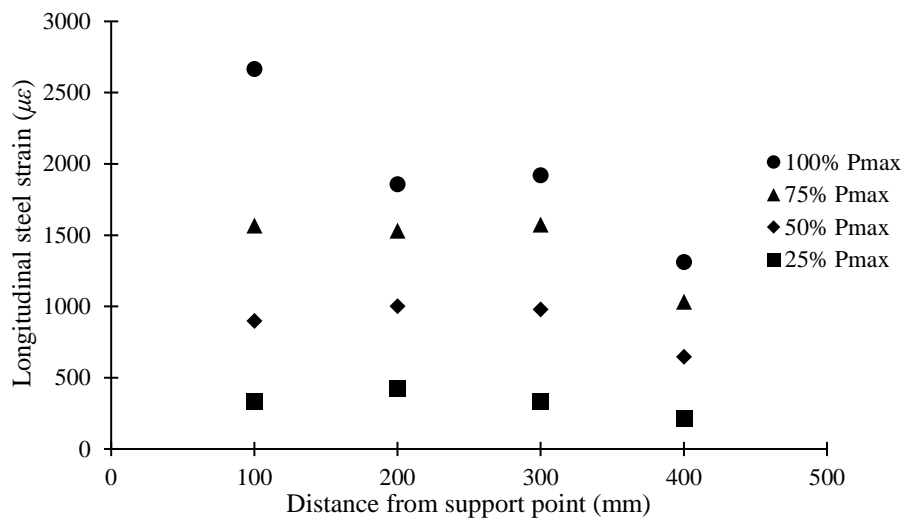
(a) D-II-1S
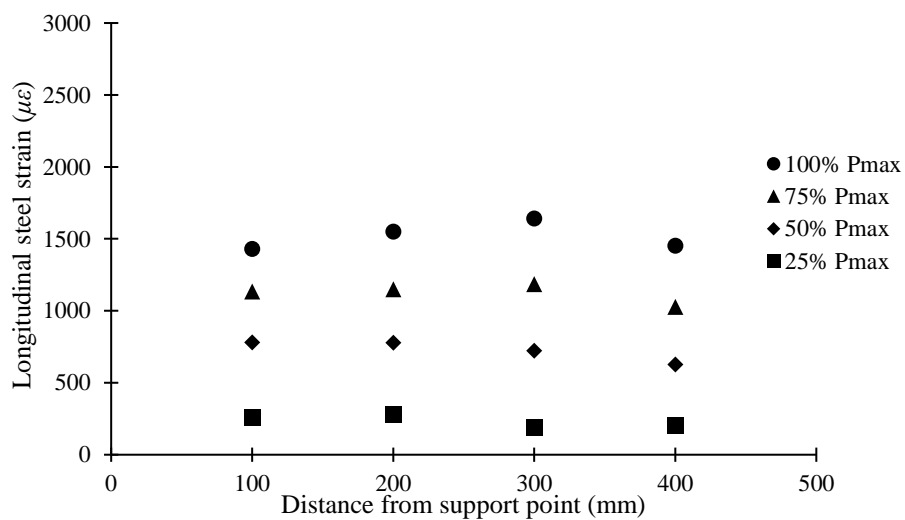
(b) D-II-2S

Figure 5.15: Steel strain profile of strengthened specimens – Scheme STM II
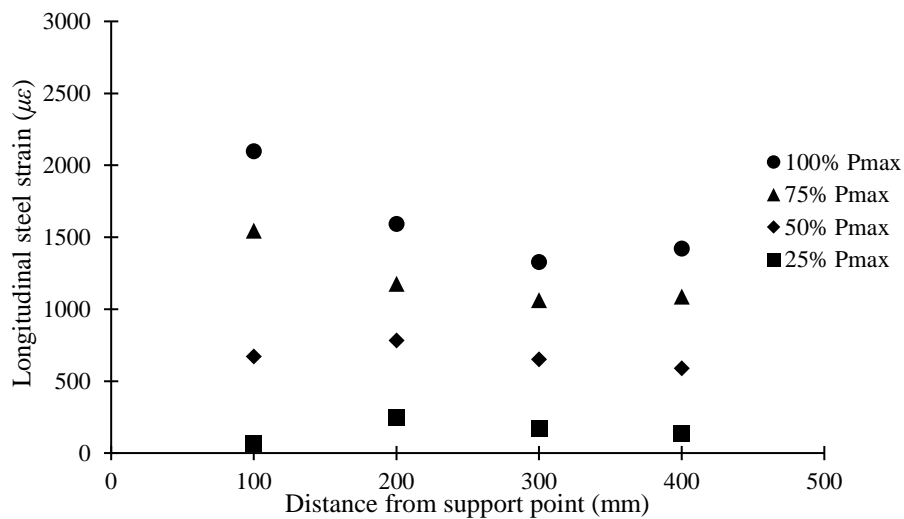
(a) D-III-1S
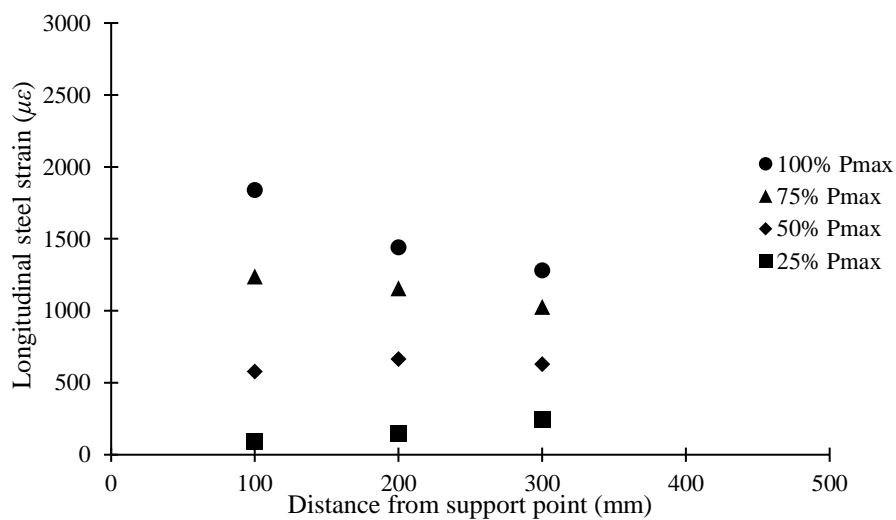
(b) D-III-2S

Figure 5.16: Steel strain profile of strengthened specimens – Scheme STM III

5.5.2 CFRP Strains

The strains in CFRP reinforcement are reported in this section. The strain gauges were installed on CFRP strips at the closest point to the opening. The designation for all CFRP strain readings began with the letter F to denote the readings were for CFRP reinforcement. Letters A or B were used to indicate that the CFRP reinforcement was located above or below the opening, respectively. The number 1 was used in case of single strip or the for the closest strip to the opening in case of double strips. The letters E or W were used to indicate whether the reading was taken in the east or west shear span, respectively.

The CFRP strain responses in the STM I specimens are shown in Figure 5.17. both specimens exhibited a bilinear load-strain response. The slope changed at approximately 120 kN for D-I-1S and 140 kN for D-I-2S. The strain gauge FB1-W in specimen D-I-1S experienced a significant increase in strain after cracking then failed at 160 kN with a corresponding strain value of 3673 $\mu\varepsilon$. The increase rate of CFRP strains was almost the same for both specimens. No rupture was observed through strain readings or visually during testing.

Figure 5.18 presents the CFRP strain response of the STM II specimens. The trend was bilinear. The strain values within the same specimens were almost identical. The CFRP strips in D-II-1S experienced higher strains than those of specimen D-II-2S. This is logical as the amount of CFRP in D-II-2S was double the amount of CFRP in D-II-S1.

Figure 5.19 (a) and (b) show the strain responses of CFRP in the bottom and top chords of STM III specimens, respectively. FA1-W and FA2-W strain gauges

failed during the early stages of testing. The general trend of the curves was bilinear. The strain in the bottom and top chords were insignificantly different. Specimen D-III-1S tended to exhibit higher strains than those of D-III-2S. The values of the strain were well below the ultimate strain of CFRP (19000 µε).
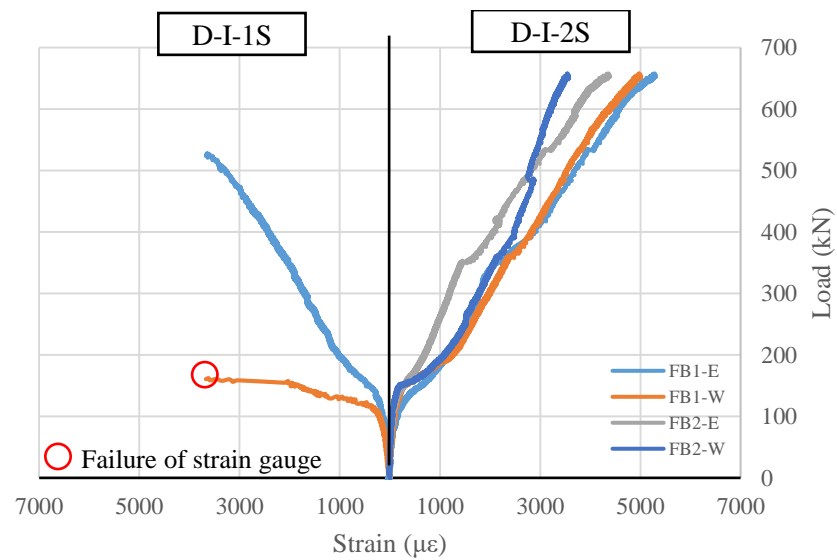
Figure 5.17: CFRP strain response of STM I specimens
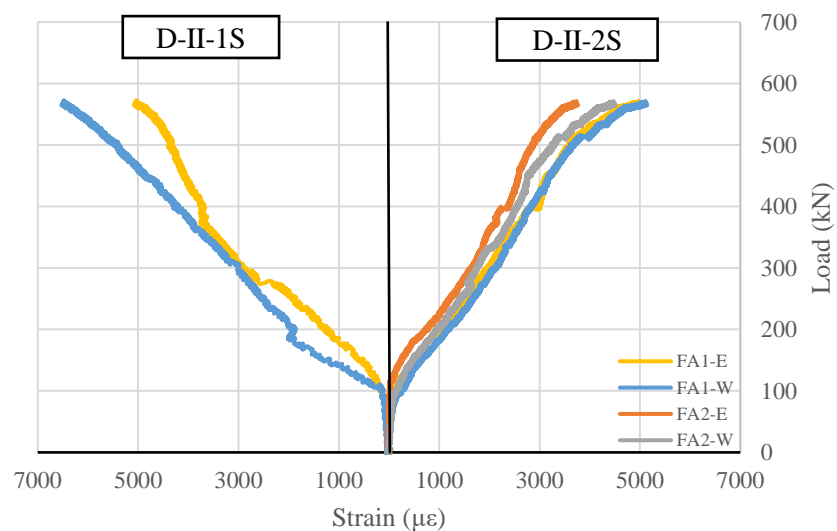
Figure 5.18: CFRP strain response of STM II specimens
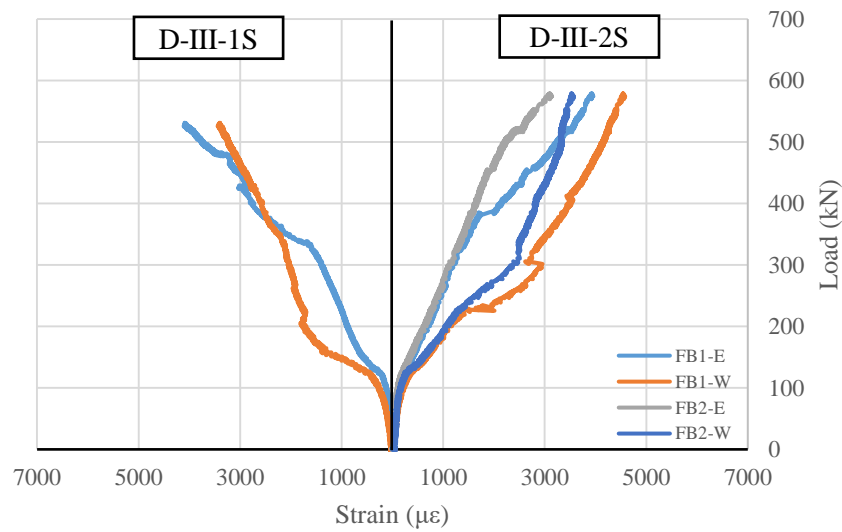
(a) CFRP strips in the bottom chord
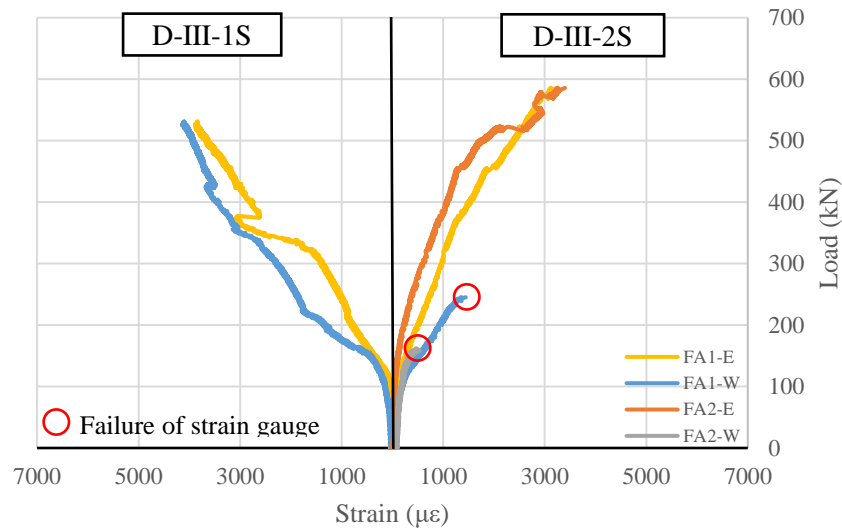
(b) CFRP strips in the top chord

Figure 5.19: CFRP strain response of STM III specimens

5.5.3 Concrete Strains

Values of the measured concrete strains at ultimate load in longitudinal and diagonal directions are presented in Table 5.3. The terms CL-M, CL-W, and CL-E refer to strain readings at the midspan and below the west and east loading points, respectively. The terms CD1-W and CD2-W refer to diagonal strains in the top and bottom chords of the west shear span, respectively. Whereas CD1-E and CD2-E refer

to diagonal strains in the top and bottom chords of east shear span, respectively. Some readings were missing due to malfunction of the strain gauges.

Table 5.4 reports the maximum longitudinal and diagonal concrete strains. For the solid specimen, the maximum concrete strain in the longitudinal direction (857 με) was measured at the midspan top surface of the beam. The maximum diagonal concrete strain was 604 με in the east shear span. In specimen D-NS, the existence of the openings in shear span resulted in significant increase in the diagonal concrete strain. The maximum measured strain in D-NS in the diagonal direction was 1841 με recorded at 96% of ultimate load before the failure of the strain gauge at the west bottom chord. Whereas, the maximum longitudinal strain was only 761 με. In general, the concrete strain values in the bottom chords were significantly higher than those in the top chord except for specimen D-III-2S which exhibited equal strains in the top and bottom chords.

STM I specimens exhibited insignificant difference between longitudinal and diagonal strains. The maximum concrete strain values for both specimens (D-I-1S and D-I-2S) were around 1000 με.

Specimen D-II-1S exhibited a minor difference between the maximum longitudinal and diagonal strains which were 1355 and 1062 με, respectively. However, the higher amount of NSM-CFRP reinforcement in D-II-2S provided a significant increase in the diagonal concrete strain in the bottom chord which reached 1714 με. As the NSM-CFRP reinforcement applied in the top and bottom chords in STM III specimens, the strain results showed that the values of the maximum diagonal strain were lower than those of longitudinal strain. The maximum

longitudinal and diagonal strains were 1826 and 1011 µε for D-III-1S, respectively, and 1617 and 798 for D-III-2S µε, respectively.

Table 5.3: Concrete strains at ultimate load

Specimen	Longitudinal strain			Diagonal strain			
	Midspan	West load point	East load point	West shear span		East shear span	
	CL-M (µε)	CL-W (µε)	CL-E (µε)	CD1-W (µε)	CD2-W (µε)	CD1-E (µε)	CD2-E (µε)
Solid	857	619	688[1]	489	-	604	-
D-NS	457	237[2]	761	255	1841[3]	146	1098
D-I-1S	675	959	779[4]	329	1000	220	841
D-I-2S	1014	917	92[5]	454	838	369	797
D-II-1S	770	802	1355	331[6]	993	247	1062
D-II-2S	798	655	869	416	1714[7]	202[8]	676
D-III-1S	733	623	1826	671	1011	543[9]	-
D-III-2S	-	891	1617	778	798	94[10]	-

[1] Strain gauge failed at 73% of ultimate load   [6] Strain gauge failed at 76% of ultimate load

[2] Strain gauge failed at 64% of ultimate load   [7] Strain gauge failed at 96% of ultimate load

[3] Strain gauge failed at 96% of ultimate load   [8] Strain gauge failed at 75% of ultimate load

[4] Strain gauge failed at 56% of ultimate load   [9] Strain gauge failed at 85% of ultimate load

[5] Strain gauge failed at 15% of ultimate load   [10] Strain gauge failed at 66% of ultimate load

Table 5.4: Maximum concrete strains

Specimen	Longitudinal strain (µε)	Diagonal strain (µε)
Solid	857	604
D-NS	761	1841
D-I-1S	959	1000
D-I-2S	1014	838
D-II-1S	1355	1062
D-II-2S	869	1714
D-III-1S	1826	1011
D-III-2S	1617	798

5.6 Efficiency Factor of NSM-CFRP Strengthening Schemes

Strength results of tested specimens are presented in Table 5.5. The presence of an opening in the shear span had a major effect on the load carrying capacity of a deep beam. For the beams of current study, installation of an opening in the shear spans resulted in a 40% reduction in load carrying capacity. The NSM-CFRP strengthening schemes around the openings restored successfully the original load carrying capacity of all specimens, except D-I-1S and D-III-1S. However, the strengths of these two specimens were above 90% of that of the solid beam. The highest load capacity was achieved by specimen D-I-2S where the beam was strengthened by STM I using two CFRP strips. The amount of CFRP reinforcement had insignificant effect on the beams' capacity in STM I and STM III strengthening schemes. Doubling the amount of NSM-CFRP strips increased the capacity by 23% and 10% for STM I and STM III specimens, respectively. Increasing the amount of CFRP in the top chord of shear span for STM II specimens did not provide additional strength gain since the failure was due to a diagonal splitting in the bottom chord.

In order to evaluate the efficiency of the NSM-CFRP strengthening reinforcement, an efficiency factor was calculated. The efficiency evaluation is important from the economic standpoint. The efficiency factor (EF) was calculated by the Eq. (5.1) only for the specimens with a capacity higher than or equal to that of the solid specimen. Specimens having a load capacity lower than that of solid specimen were considered unqualified for calculating EF. In Eq. (5.1), the gained load capacity due to strengthening was divided by the summation of the tensile strengths provided by all NSM-CFRP reinforcement. The symbol P_{max} refers to the maximum load carried by the specimen, P_{D-NS} refers to the load carrying capacity of

the control specimen which contains discontinuity regions without shear reinforcement, A_{FRP} refers to the cross-sectional area of each CFRP strip used in the strengthening scheme and f_{fu} refers to the rupture strength of CFRP.

$$EF = \frac{P_{max} - P_{D-NS}}{\Sigma A_{FRP}\, f_{fu}} \times 100 \qquad (5.1)$$

The calculated efficiency factor (*EF*) for each specimen is provided in Table 5.5, besides the specimens are ranked according to their efficiency factor. Specimens D-I-1S and D-III-1S were disqualified because their strengths were less than that of the solid beam. The highest efficiency was achieved by specimen D-II-1S, where the discontinuity regions were strengthened using STM II with one CFRP strip. Specimen D-I-2S which was strengthened below the opening in each shear span with two CFRP strips came in the second place. The third place was achieved by D-II-2S. Specimen D-III-2S which was strengthened with double CFRP strips in the top and bottom chords achieved the least rank The application of NSM-CFRP above and below the opening resulted less efficiency due to the high amount of NSM-CFRP used. For all STM strengthening layouts, it was found that increasing the amount of CFRP reduced the efficiency of the strengthening scheme. This occurred because the strength gain was not proportional to CFRP amount.

Table 5.5: CFRP material efficiency factor

Specimen	P_{max} (kN)	P_{max}/P_{solid}	$P_{max} - P_{D-NS}$ (kN)	ΣA_{FRP}	$A_{FRP} f_{fu}^{*}$ (kN)	EF (%)	Rank
Solid	565	-	-	-	-	-	-
D-NS	338	60%	-	-	-	-	-
D-I-1S	528	93%	-	-	-	-	-
D-I-2S	658	116%	320	300	930	34%	2
D-II-1S	573	101%	235	150	465	51%	1
D-II-2S	572	101%	234	300	930	25%	3
D-III-1S	531	94%	-	-	-	-	-
D-III-2S	586	104%	248	600	1860	13%	4

* f_{fu} = 3100 MPa

5.7 Summary

Throughout this chapter, the results obtained from laboratory testing were presented and discussed. This included the load deflection response, failure mode, crack pattern, and strain measurements. The effectiveness of the NSM-CFRP reinforcement in strengthening the discontinuity regions was examined throughout the obtained experimental results. Furthermore, an efficiency factor was developed to assess the economical sufficiency of each strengthening solution. The accuracy of STM predictions will be evaluated in the following chapter.

Chapter 6: Strut-and-Tie Model Predictions

6.1 Introduction

This chapter presents STM results of the tested specimens. ACI 318-14 [1] and CSA S806 [5] provisions were applied to calculate the strength of the specimens. The STM analysis requires several iterations to reach a solution (ultimate load). The details of calculations for the last iteration are presented. At the end of the chapter, the accuracy of the predictions is examined through a comparison with experimental results.

6.2 STM Procedures

The ultimate load of the specimens was calculated based on the capacity limits in struts, ties and external nodal zones. The truss layout and the load of each truss member are presented in a schematic drawing for each specimen in Figure 6.1 to Figure 6.14. The rectangular boxes contain the designation of struts and ties. The letter "S" denotes a strut and the letter "T" denotes a tie. The circles are used for numbering the nodes. The STM procedures to calculate the load capacity are summarized as follows:

1. The generated internal forces in the truss elements by a given external load value were computed.
2. The capacities of truss elements (struts, ties, nodes) were computed as per the corresponding code or standards.
3. The values of the internal forces were compared with those of the truss elements' capacities.
4. The steps 1 to 3 were repeated until an element reached its capacity limit.

The calculations for the load capacity are provided in Table 6.1 to Table 6.14. It should be noted that the external nodal zones at the load and support locations are

typically more critical than the internal nodal zones. This is because the capacity of the internal nodal zones is governed by the capacity limit of the adjoining struts which are already considered in the analysis. Also, there is a sufficient area to spread the reinforcement of the adjoining ties. As such, only the calculations of the external nodal zones at the support and load locations are presented.

6.3 STM Results

6.3.1 STM Results Based on ACI 318-14

This section presents the results of STMs as per ACI 318-14 [1] code provisions. The following are the notations used in this section:

F_i = internal force of the element
w_s = width of strut
β_s = strut coefficient
F_{ni} = nominal strength of the truss element
β_n = node coefficient
F_r = resultant force on a node face
w_n = width of a node face
F_{nn} = nominal strength of the node

The predicted load capacity of the solid specimen was 562 kN. The strength of the beam was limited by the failure of the diagonal strut in the shear span. For D-I-1S, the failure was due to rupture of the diagonal tie below the opening (T2). However, a different failure mode was observed in experimental testing. The predicted load capacity of D-I-1S was 470 kN. The predicted load capacity for D-I-2S was 636 kN. The failure occurred in strut S4. Despite that, the failure experimentally was due to crushing of strut S3. The predicted capacity of D-II-1S was limited to a load value of 518 kN due to the failure in the diagonal tie (T2). Comparing the calculated strength of D-II-1S and D-II-2S would show that doubling the amount of CFRP reinforcement has prevented the failure in the T2. Therefore, the

predicted strength of specimen D-II-2S was 640 kN. As per the STM calculation, failure of D-II-2S occurred in strut S5. Remarkably, the failure observed experimentally occurred at the same predicted location. For D-III-1S, the predicted load capacity was limited by the failure of the diagonal tie above the opening (T2) at 586 kN. At the same load of 586 kN, S3 reached 92% of its nominal strength. Therefore, doubling the amount of shear reinforcement in D-III-2S resulted in a slight increase in the load capacity. The predicted failure load of specimen D-III-2S was 636 kN. The failure was predicted to occur in strut S3 which was in agreement with the failure mode observed experimentally.
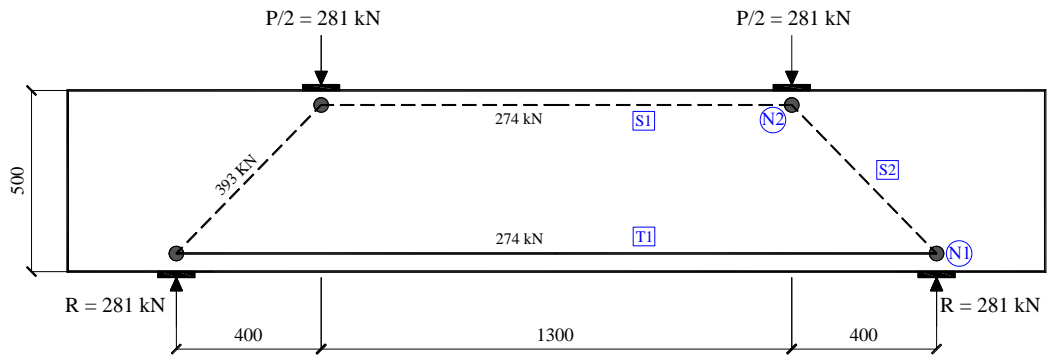
Figure 6.1: Schematic drawing of the internal forces of the solid beam at failure
($P_u = 562$ kN)

Table 6.1: STM calculations for the solid beam at failure ($P_u = 562$ kN)

Element	Type	F_i (kN)	w_s or w_n (mm)	Area (mm²)	β_s or β_n	F_{ni} (kN)	Status
S1	Strut	274	80	12000	1.0	408	Safe
S2	Strut	393	128	19209	0.6	392	Failed
T1	Tie	274	-	804	-	438	Safe
N1	Node (horizontal face)	281	100	15000	0.8	408	Safe
(CCT)	Node (inclined face)	393	141	21150	0.8	575	Safe
	Node (vertical face)	274	100	15000	0.8	408	Safe
N2	Node (horizontal face)	281	100	15000	1	510	Safe
(CCC)	Node (vertical face)	274	80	12000	1	408	Safe
	Node (inclined face)	393	128	19200	1	653	Safe

Figure 6.2: Schematic drawing of the internal forces of D-I-1S at failure
($P_u = 470$ kN)

Table 6.2: STM calculations for D-I-1S at failure ($P_u = 470$ kN)

Element	Type	F_i (kN)	w_s or w_n (mm)	Area (mm^2)	β_s or β_n	F_{ni} (kN)	Status
S1	Strut	229	80	12000	1.0	408	Safe
S2	Strut	188	111	16713	0.6	341	Safe
S3	Strut	174	120	18026	0.6	368	Safe
S4	Strut	235	104	15600	0.6	318	Safe
T1	Tie	229	-	804	-	438	Safe
T2	Tie	233	-	75	-	233	Failed
T3	Tie	10	-	804	-	438	Safe
N1	Node (horizontal face)	235	100	15000	0.8	408	Safe
(CCT)	Node (inclined face)	235	104	15600	0.8	424	Safe
	Node (vertical face)	10	100	15000	0.8	408	Safe
N2	Node (horizontal face)	235	100	15000	1	510	Safe
(CCC)	Node (vertical face)	229	80	12000	1	408	Safe
	Node (inclined face)	188	111	16650	1	566	Safe
	Node (inclined face)	174	120	18000	1	612	Safe
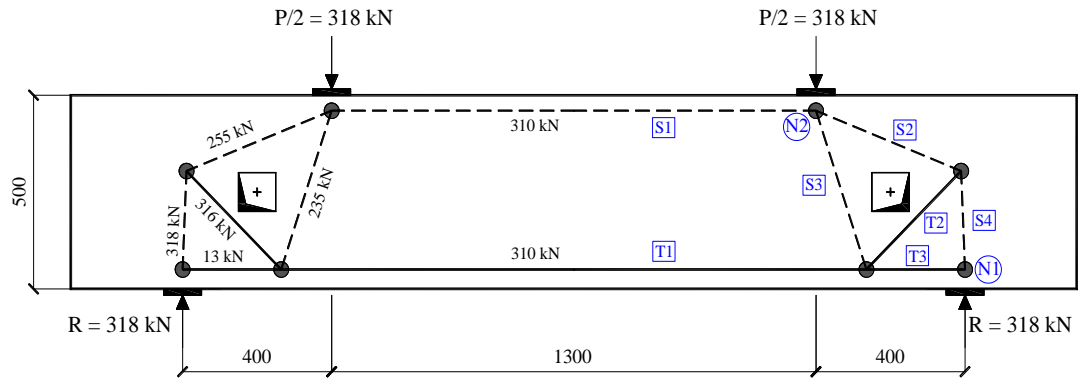
Figure 6.3: Schematic drawing of the internal forces of D-I-2S at failure
(P_u = 636 kN)

Table 6.3: STM calculations for D-I-2S at failure (P_u = 636 kN)

Element	Type	F_i (kN)	w_s or w_n (mm)	Area (mm²)	β_s or β_n	F_{ni} (kN)	Status
S1	Strut	310	80	12000	1.0	408	Safe
S2	Strut	255	111	16713	0.6	341	Safe
S3	Strut	235	120	18026	0.6	368	Safe
S4	Strut	318	104	15600	0.6	318	Failed
T1	Tie	310	-	804	-	438	Safe
T2	Tie	316	-	150	-	465	Safe
T3	Tie	13	-	804	-	438	Safe
N1	Node (horizontal face)	318	100	15000	0.8	408	Safe
(CCT)	Node (inclined face)	318	104	15600	0.8	424	Safe
	Node (vertical face)	13	100	15000	0.8	408	Safe
N2	Node (horizontal face)	318	100	15000	1	510	Safe
(CCC)	Node (vertical face)	310	80	12000	1	408	Safe
	Node (inclined face)	255	111	16650	1	566	Safe
	Node (inclined face)	235	120	18000	1	612	Safe
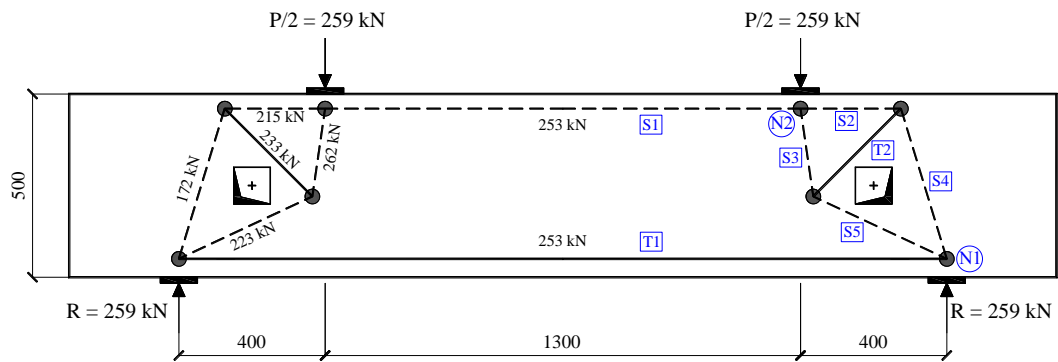
Figure 6.4: Schematic drawing of the internal forces of D-II-1S at failure
(P_u = 518 kN)

Table 6.4: STM calculations for D-II-1S at failure (P_u = 518 kN)

Element	Type	F_i (kN)	w_s or w_n (mm)	Area (mm²)	β_s or β_n	F_{ni} (kN)	Status
S1	Strut	253	80	12000	1.0	408	Safe
S2	Strut	215	80	12000	1.0	408	Safe
S3	Strut	262	110	16500	0.6	337	Safe
S4	Strut	172	126	18900	0.6	386	Safe
S5	Strut	223	90	13500	0.6	275	Safe
T1	Tie	253	-	804	-	438	Safe
T2	Tie	233	-	75	-	233	Failed
N1	Node (horizontal face)	259	100	15000	0.8	408	Safe
(CCT)	Node (inclined face)	172	127	19050	0.8	518	Safe
	Node (inclined face)	223	127	19050	0.8	518	Safe
	Node (vertical face)	253	100	15000	0.8	408	Safe
N2	Node (horizontal face)	259	100	15000	1	510	Safe
(CCC)	Node (vertical face)	253	80	12000	1	408	Safe
	Node (inclined face)	215	80	12000	1	408	Safe
	Node (inclined face)	262	111	16650	1	566	Safe
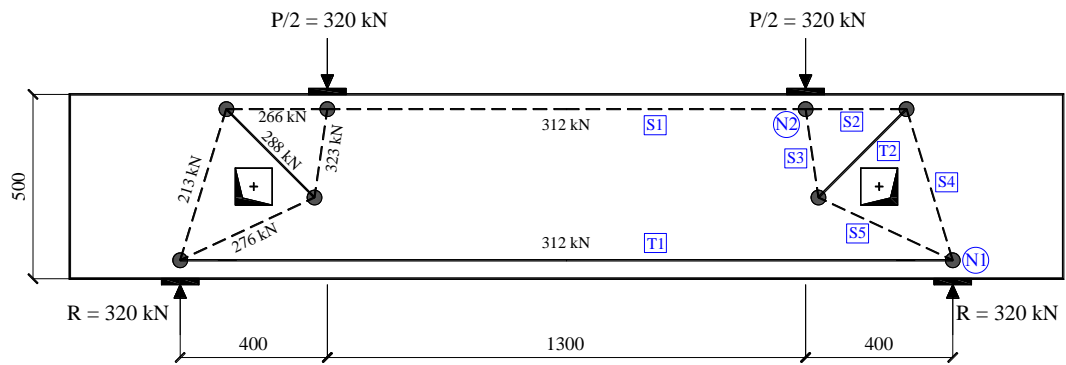
Figure 6.5: Schematic drawing of the internal forces of D-II-2S at failure
$(P_u = 640$ kN)

Table 6.5: STM calculations for D-II-2S at failure $(P_u = 640$ kN)

Element	Type	F_i (kN)	w_s or w_n (mm)	Area (mm^2)	β_s or β_n	F_{ni} (kN)	Status
S1	Strut	312	80	12000	1.0	408	Safe
S2	Strut	266	80	12000	1.0	408	Safe
S3	Strut	323	110	16500	0.6	337	Safe
S4	Strut	213	126	18900	0.6	386	Safe
S5	Strut	276	90	13500	0.6	275	Failed
T1	Tie	312	-	804	-	438	Safe
T2	Tie	288	-	150	-	465	Safe
N1	Node (horizontal face)	320	100	15000	0.8	408	Safe
(CCT)	Node (inclined face)	213	127	19050	0.8	518	Safe
	Node (inclined face)	276	127	19050	0.8	518	Safe
	Node (vertical face)	312	100	15000	0.8	408	Safe
N2	Node (horizontal face)	320	100	15000	1	510	Safe
(CCC)	Node (vertical face)	312	80	12000	1	408	Safe
	Node (inclined face)	266	80	12000	1	408	Safe
	Node (inclined face)	323	111	16650	1	566	Safe
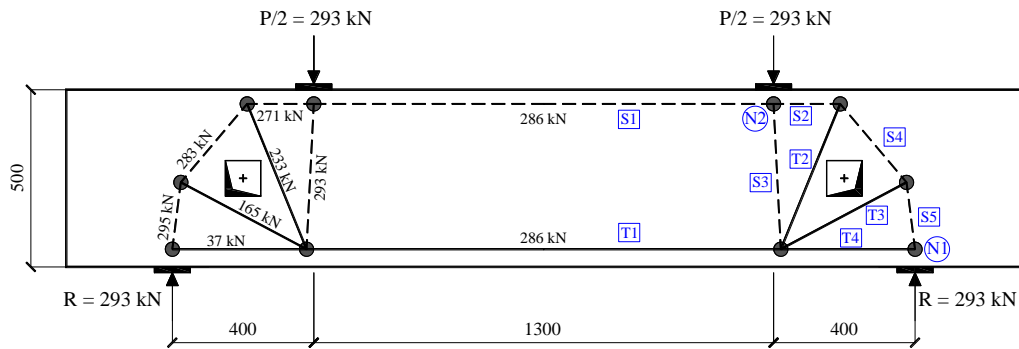
Figure 6.6: Schematic drawing of the internal forces of D-III-1S at failure
(Pu = 586 kN)

Table 6.6: STM calculations for D-III-1S at failure (P_u = 586 kN)

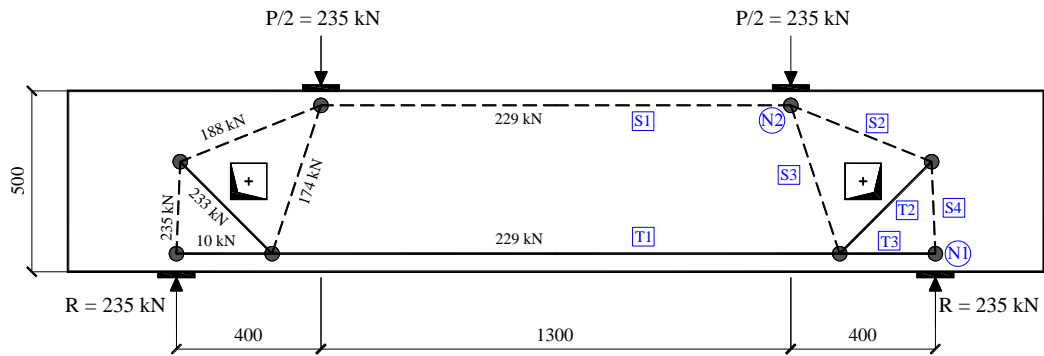| Element	Type	F_i (kN)	w_s or w_n (mm)	Area (mm²)	β_s or β_n	F_{ni} (kN)	Status
S1	Strut	286	80	12000	1.0	408	Safe
S2	Strut	271	80	12000	1.0	408	Safe
S3	Strut	293	104	15600	0.6	318	Safe
S4	Strut	283	113	16950	0.6	346	Safe
S5	Strut	295	112	16800	0.6	343	Safe
T1	Tie	286	-	804	-	438	Safe
T2	Tie	233	-	75	-	233	Failed
T3	Tie	165	-	75	-	233	Safe
T4	Tie	37	-	804	-	438	Safe
N1	Node (horizontal face)	293	100	15000	0.8	408	Safe
(CCT)	Node (inclined face)	295	112	16800	0.8	457	Safe
	Node (vertical face)	286	100	15000	0.8	408	Safe
N2	Node (horizontal face)	293	100	15000	1	510	Safe
(CCC)							
	Node (vertical face)	286	80	12000	1	408	Safe
	Node (inclined face)	271	80	12000	1	408	Safe
	Node (inclined face)	293	104	15600	1	530	Safe
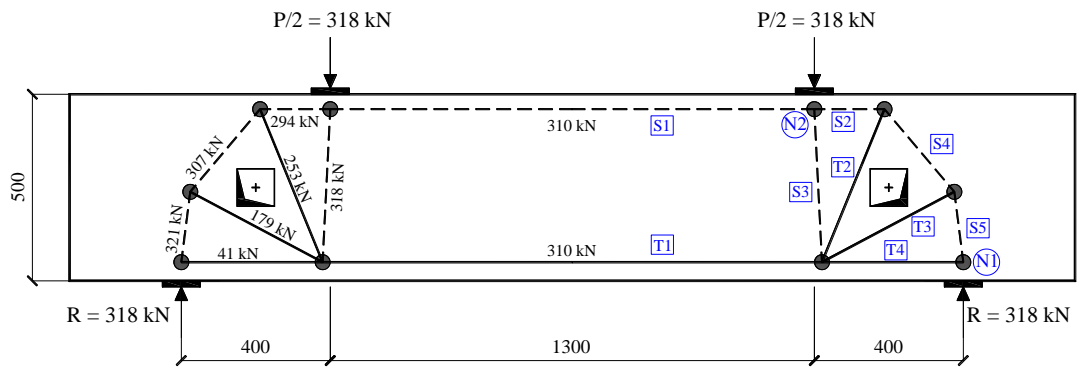
Figure 6.7: Schematic drawing of the internal forces of D-III-2S at failure
($P_u = 636$ kN)

Table 6.7: STM calculations for D-III-2S at failure ($P_u = 636$ kN)

Element	Type	F_i (kN)	w_s or w_n (mm)	Area (mm^2)	β_s or β_n	F_{ni} (kN)	Status
S1	Strut	310	80	12000	1.0	408	Safe
S2	Strut	294	80	12000	1.0	408	Safe
S3	Strut	318	104	15600	0.6	318	Failed
S4	Strut	307	113	16950	0.6	346	Safe
S5	Strut	321	112	16800	0.6	343	Safe
T1	Tie	310	-	804	-	438	Safe
T2	Tie	253	-	150	-	465	Safe
T3	Tie	179	-	150	-	465	Safe
T4	Tie	41	-	804	-	438	Safe
N1	Node (horizontal face)	318	100	15000	0.8	408	Safe
(CCT)	Node (inclined face)	321	112	16800	0.8	457	Safe
	Node (vertical face)	310	100	15000	0.8	408	Safe
N2	Node (horizontal face)	318	100	15000	1	510	Safe
(CCC)	Node (vertical face)	310	80	12000	1	408	Safe
	Node (inclined face)	294	80	12000	1	408	Safe
	Node (inclined face)	318	104	15600	1	530	Safe

6.3.2 STM Results Based on CSA S806

This section presents calculations and results of STMs as per CSA S806 [5] standard provisions. The abbreviations that are used in this section are defined as follow:

F_i = internal force of the element
ε_f = tensile strain in an adjoining tie
θ_s = the smallest angle between the strut and the adjoining tie
ε_1 = calculated transverse tensile strain in a cracked strut
f_{cu} = calculated limiting compressive strength in the strut
F_{ni} = nominal strength of the element

The predicted failure load of the solid specimen was 738 kN. The predicted failure occurred due to crushing of the diagonal strut in the shear span. The maximum calculated strength of specimen D-I-1S was 368 kN due to failure of strut S4. Specimen D-I-2S failed also due to crushing of strut S4 but at a higher load value of 480 kN. This can be attributed to the reduced strain in the adjoining ties when calculating the strut strength. When more CFRP reinforcements were added, the strain in the tie at a certain value of load became less. Accordingly, the capacity of strut S4 in specimen D-I-2S was higher. Moving to STM II specimens, failure of specimen D-II-1S occurred due to crushing of strut S2 at 352 kN. Specimen D-II-2S failed due to crushing of the diagonal strut S5 in the bottom chord at 422 kN. Specimens D-III-1S and D-III-2S failed by crushing of S3. This was consistent with the failure mode observed experimentally for D-III-2S. The predicted load capacities for D-III-1S and D-III-2S were 220 kN and 280 kN, respectively. In STM III, the angle between S3 and T2 was very small (25.1°) which increased the calculated transverse strain in S3 and hence reduced its limiting compressive strength.
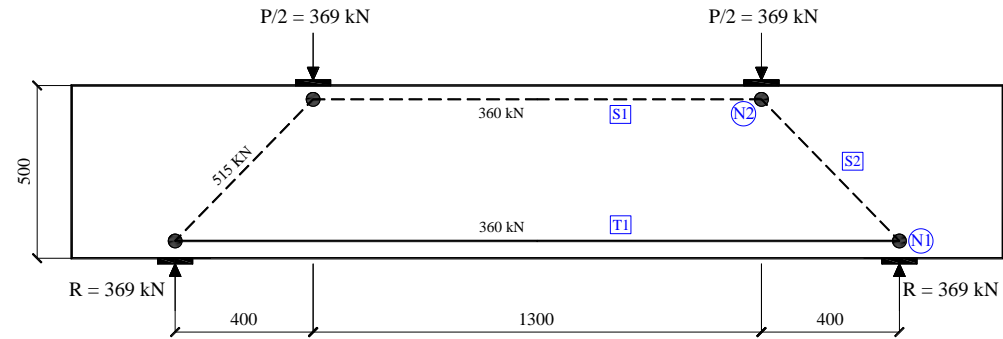
Figure 6.8: Schematic drawing of the internal forces of the solid beam at failure (P_u = 738 kN)

Table 6.8: STM calculations for the solid beam at failure (P_u = 738 kN)

Element	Type	F_i (kN)	w_s or w_n (mm)	Area (mm²)	Adjoining tie	$\varepsilon_f/2$	θ_s (degree)	ε_1	F_{cu} (MPa)	$0.85f'_c$ (MPa)	Selected stress limit (MPa)	F_{ni} (kN)	Status
S1	Strut	360	80	12000	-	-	-	0	50.0	34.0	34.0	408	Safe
S2	Strut	515	128	19209	T1	0.0011	45.7	0.0041	26.8	34.0	26.8	514	Failed
T1	Tie	360	-	804	-	0.0022	-	-	-	-	-	438	Safe
N1	Node (horizontal face)	369	100	15000	-	-	-	-	-	-	30.0*	450	Safe
(CCT)	Node (inclined face)	515	141	21150	-	-	-	-	-	-	30.0*	635	Safe
	Node (vertical face)	360	100	15000	-	-	-	-	-	-	30.0*	450	Safe

* for CCC node stress limit = $0.85 f'_c$ and for CCT node stress limit = $0.75 f'_c$

Table 6.8: STM calculations for the solid beam at failure (Pu = 738 kN) (Continued)

Element	Type	F_i (kN)	w_s or w_n (mm)	Area (mm²)	Adjoining tie	$\varepsilon_f/2$	θ_s (degree)	ε_l	F_{cu} (MPa)	$0.85f'_c$ (MPa)	Selected stress limit (MPa)	F_{ni} (kN)	Status
N2	Node (horizontal face)	369	100	15000	-	-	-	-	-	-	34.0*	510	Safe
(CCC)	Node (vertical face)	360	80	12000	-	-	-	-	-	-	34.0*	408	Safe
	Node (inclined face)	515	128	19200	-	-	-	-	-	-	34.0*	653	Safe

* for CCC node stress limit = 0.85 f'_c and for CCT node stress limit = 0.75 f'_c

Figure 6.9: Schematic drawing of the internal forces of D-I-1S at failure (P_u = 368 kN)

Table 6.9: STM calculations for D-I-1S at failure (P_u = 368 kN)

Element	Type	F_i (kN)	w_s or w_n (mm)	Area (mm²)	Adjoining tie	$\varepsilon_f/2$	θ_s (degree)	ε_1	F_{cu} (MPa)	$0.85f'_c$ (MPa)	Selected stress limit (MPa)	F_{ni} (kN)	Status
S1	Strut	180	80	12000	-	-	-	0	50.0	34.0	34.0	408	Safe
S2	Strut	147	111	16713	T2	0.0074	66.8	0.0091	17.0	34.0	17.0	285	Safe
S3	Strut	136	120	18026	T1	0.0006	71.7	0.0008	42.4	34.0	16.3	293	Safe
		136	120	18026	T2	0.0074	63.3	0.0098	16.3				
		136	120	18026	T3	0.0000	71.7	0.0002	47.5				
S4	Strut	184	104	15600	T2	0.0074	47.4	0.0153	11.7	34.0	11.7	183	Failed
		184	104	15600	T3	0.0000	87.6	0.0000	49.7				
T1	Tie	180	-	804	-	-	-	-	-	-	-	438	Safe
T2	Tie	183	-	75	-	-	-	-	-	-	-	233	Safe
T3	Tie	8	-	804	-	-	-	-	-	-	-	438	Safe
N1	Node (horizontal face)	184	100	15000	-	-	-	-	-	-	30.0*	450	Safe
(CCT)	Node (inclined face)	184	104	15600	-	-	-	-	-	-	30.0*	468	Safe
	Node (vertical face)	8	100	15000	-	-	-	-	-	-	30.0*	450	Safe
N2	Node (horizontal face)	184	100	15000	-	-	-	-	-	-	34.0*	510	Safe
(CCC)	Node (vertical face)	180	80	12000	-	-	-	-	-	-	34.0*	408	Safe
	Node (inclined face)	147	111	16650	-	-	-	-	-	-	34.0*	566	Safe
	Node (inclined face)	136	120	18000	-	-	-	-	-	-	34.0*	612	Safe

* for CCC node stress limit = 0.85 f'_c and for CCT node stress limit = 0.75 f'_c

Figure 6.10: Schematic drawing of the internal forces of D-I-2S at failure (P_u = 480 kN)

Table 6.10: STM calculations for D-I-2S at failure (P_u = 480 kN)

Element	Type	F_i (kN)	w_s or w_n (mm)	Area (mm^2)	Adjoining tie	$\varepsilon_f/2$	θ_s (degree)	ε_1	F_{cu} (MPa)	$0.85f'_c$ (MPa)	Selected stress limit (MPa)	F_{ni} (kN)	Status
S1	Strut	234	80	12000	-	-	-	0	50.0	34.0	34.0	408	Safe
S2	Strut	192	111	16713	T2	0.0048	66.8	0.0061	21.8	34.0	21.8	365	Safe
S3	Strut	178	120	18026	T1	0.0007	71.7	0.0010	41.0	34.0	20.9	377	Safe
		178	120	18026	T2	0.0048	63.3	0.0065	20.9				
		178	120	18026	T3	0.0000	71.7	0.0003	47.5				
S4	Strut	240	104	15600	T2	0.0048	47.4	0.0106	15.4	34.0	15.4	240	Failed
		240	104	15600	T3	0.0000	87.6	0.0000	49.6				
T1	Tie	234	-	804	-	-	-	-	-	-	-	438	Safe

Table 6.10: STM calculations for D-I-2S at failure ($Pu = 480$ kN) (Continued)

Element	Type	F_i (kN)	w_s or w_n (mm)	Area (mm^2)	Adjoining tie	$\varepsilon_f/2$	θ_s (degree)	ε_1	F_{cu} (MPa)	$0.85f'_c$ (MPa)	Selected stress limit (MPa)	F_{ni} (kN)	Status
T1	Tie	234	-	804	-	-	-	-	-	-	-	438	Safe
T2	Tie	238	-	150	-	-	-	-	-	-	-	465	Safe
T3	Tie	10	-	804	-	-	-	-	-	-	-	438	Safe
N1	Node (horizontal face)	240	100	15000	-	-	-	-	-	-	30.0*	450	Safe
(CCT)	Node (inclined face)	240	104	15600	-	-	-	-	-	-	30.0*	468	Safe
	Node (vertical face)	10	100	15000	-	-	-	-	-	-	30.0*	450	Safe
N2	Node (horizontal face)	240	100	15000	-	-	-	-	-	-	34.0*	510	Safe
(CCC)	Node (vertical face)	234	80	12000	-	-	-	-	-	-	34.0*	408	Safe
	Node (inclined face)	192	111	16650	-	-	-	-	-	-	34.0*	566	Safe
	Node (inclined face)	178	120	18000	-	-	-	-	-	-	34.0*	612	Safe

* for CCC node stress limit = $0.85\,f'_c$ and for CCT node stress limit = $0.75\,f'_c$
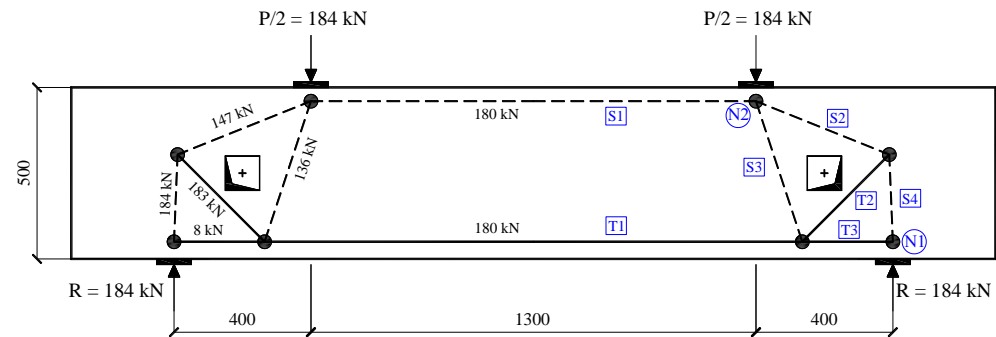

Figure 6.11: Schematic drawing of the internal forces of D-II-1S at failure ($P_u = 352$ kN)

Table 6.11: STM calculations for D-II-1S at failure ($P_u = 352$ kN)

Element	Type	F_i (kN)	w_s or w_n (mm)	Area (mm²)	Adjoining tie	$\varepsilon_f/2$	θ_s (degree)	ε_1	F_{cu} (MPa)	$0.85f'_c$ (MPa)	Selected stress limit (MPa)	F_{ni} (kN)	Status
S1	Strut	172	80	12000	-	-	-	0	50.0	34.0	34.0	408	Safe
S2	Strut	146	80	12000	T2	0.0064	45	0.0148	12.1	34.0	12.1	145	Failed
S3	Strut	178	110	16500	T2	0.0064	53.3	0.0111	14.9	34.0	14.9	246	Safe
S4	Strut	117	126	18900	T1	0.0005	73	0.0008	43.0	34.0	17.5	330	Safe
		117	126	18900	T2	0.0064	62	0.0088	17.5				
S5		152	90	13500	T1	0.0005	25	0.0122	13.9	34.0	13.9	188	Safe
		152	90	13500	T2	0.0064	70	0.0075	19.3				
T1	Tie	172	-	804	-	-	-			-	0	438	Safe
T2	Tie	158	-	75	-	-	-			-	0	233	Safe
N1	Node (horizontal face)	176	100	15000	-	-	-	-	-	-	30.0*	450	Safe
(CCT)	Node (inclined face)	117	127	19050	-	-	-	-	-	-	30.0*	572	Safe
	Node (inclined face)	152	127	19050	-	-	-	-	-	-	30.0*	572	Safe
	Node (vertical face)	172	100	15000	-	-	-	-	-	-	30.0*	450	Safe
N2	Node (horizontal face)	176	100	15000	-	-	-	-	-	-	34.0*	510	Safe
(CCC)	Node (vertical face)	172	80	12000	-	-	-	-	-	-	34.0*	408	Safe
	Node (inclined face)	146	80	12000	-	-	-	-	-	-	34.0*	408	Safe
	Node (inclined face)	178	111	16650	-	-	-	-	-	-	34.0*	566	Safe

* for CCC node stress limit = 0.85 f'_c and for CCT node stress limit = 0.75 f'_c
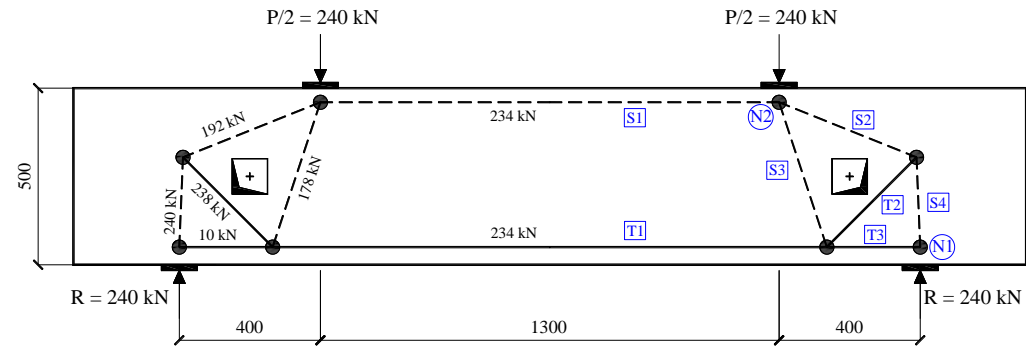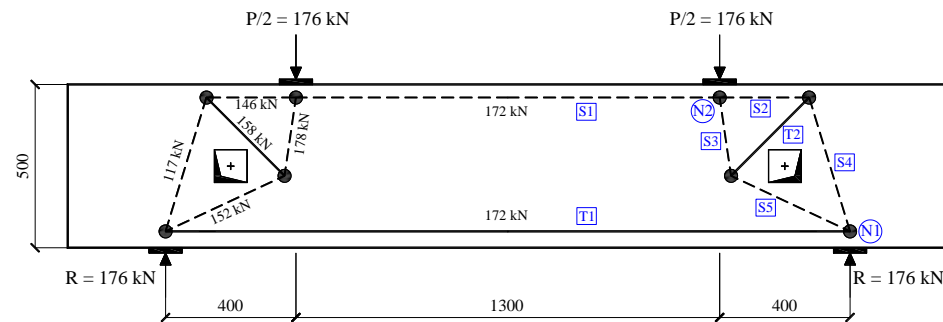
Figure 6.12: Schematic drawing of the internal forces of D-II-2S at failure (P_u = 422 kN)

Table 6.12: STM calculations for D-II-2S at failure (P_u = 422 kN)

Element	Type	F_i (kN)	w_s or w_n (mm)	Area (mm²)	Adjoining tie	$\varepsilon_f/2$	θ_s (degree)	ε_1	F_{cu} (MPa)	$0.85f'_c$ (MPa)	Selected stress limit (MPa)	F_{ni} (kN)	Status
S1	Strut	206	80	12000	-	-	-	0	50.0	34.0	34.0	408	Safe
S2	Strut	175	80	12000	T2	0.0038	45	0.0097	16.4	34.0	16.4	196	Safe
S3	Strut	213	110	16500	T2	0.0038	53.3	0.0071	20.0	34.0	20.0	330	Safe
S4	Strut	140	126	18900	T1	0.0006	73	0.0009	42.1	34.0	23.1	437	Safe
		140	126	18900	T2	0.0038	62	0.0055	23.1				
S5		182	90	13500	T1	0.0006	25	0.0128	13.5	34.0	13.5	182	Failed
		182	90	13500	T2	0.0038	70	0.0046	25.3				
T1	Tie	206	-	804	-	-	-	-	-	-	-	438	Safe

Table 6.12: STM calculations for D-II-2S at failure (Pu = 422 kN) (Continued)

Element	Type	F_i (kN)	w_s or w_n (mm)	Area (mm²)	Adjoining tie	$\varepsilon_f/2$	θ_s (degree)	ε_1	F_{cu} (MPa)	$0.85f'_c$ (MPa)	Selected stress limit (MPa)	F_{ni} (kN)	Status
T2	Tie	190	-	150	-	-	-	-	-	-	-	465	Safe
N1	Node (horizontal face)	211	100	15000	-	-	-	-	-	-	30.0*	450	Safe
(CCT)	Node (inclined face)	140	127	19050	-	-	-	-	-	-	30.0*	572	Safe
	Node (inclined face)	182	127	19050	-	-	-	-	-	-	30.0*	572	Safe
	Node (vertical face)	206	100	15000	-	-	-	-	-	-	30.0*	450	Safe
N2	Node (horizontal face)	211	100	15000	-	-	-	-	-	-	34.0*	510	Safe
(CCC)	Node (vertical face)	206	80	12000	-	-	-	-	-	-	34.0*	408	Safe
	Node (inclined face)	175	80	12000	-	-	-	-	-	-	34.0*	408	Safe
	Node (inclined face)	213	111	16650	-	-	-	-	-	-	34.0*	566	Safe

* for CCC node stress limit = 0.85 f'_c and for CCT node stress limit = 0.75 f'_c
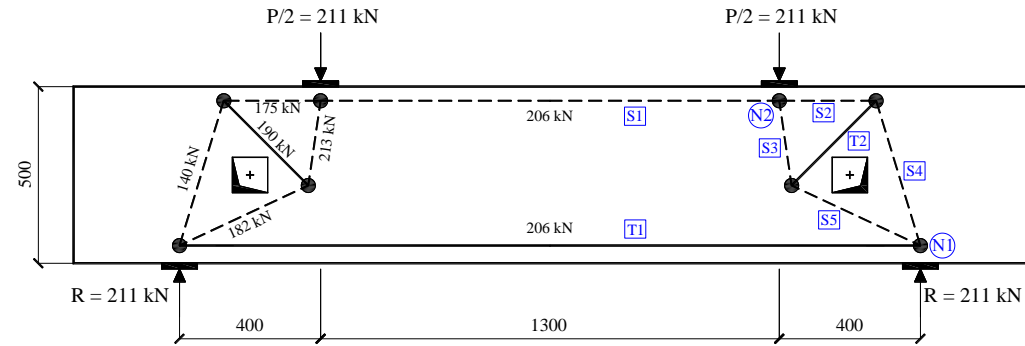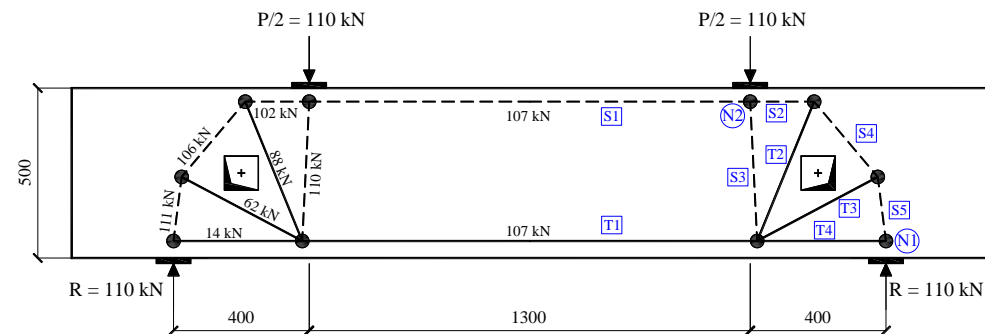

Figure 6.13: Schematic drawing of the internal forces of D-III-1S at failure (P_u = 220 kN)

Table 6.13: STM calculations for D-III-1S at failure (P_u = 220 kN)

Element	Type	F_i (kN)	w_s or w_n (mm)	Area (mm²)	Adjoining tie	$\varepsilon_f/2$	θ_s (degree)	ε_1	F_{cu} (MPa)	$0.85f'_c$ (MPa)	Selected stress limit (MPa)	F_{ni} (kN)	Status
S1	Strut	107	80	12000	-	-	-	0	50.0	34.0	34.0	408	Safe
S2	Strut	102	80	12000	T2	0.0035	67.7	0.0045	25.6	34.0	25.6	308	Safe
S3	Strut	110	104	15600	T1	0.0003	87.1	0.0003	46.6	34.0	7.0	110	Failed
		110	104	15600	T2	0.0035	25.1	0.0288	7.0				
		110	104	15600	T3	0.0025	64.9	0.0035	28.7				
		110	104	15600	T4	0.0000	87.1	0.0000	49.5				
S4	Strut	106	113	16950	T2	0.0035	62.5	0.0050	24.1	34.0	24.1	409	Safe
		106	113	16950	T3	0.0025	77.7	0.0027	31.7				
S5		111	112	16800	T3	0.0025	69.3	0.0031	30.0	34.0	30.0	504	Safe
		111	112	16800	T4	0.0000	82.7	0.0001	49.2				
T1	Tie	107	-	804	-	-	-	-	-	-	0	438	Safe
T2	Tie	88	-	75	-	-	-	-	-	-	0	233	Safe
T3	Tie	62	-	75	-	-	-	-	-	-	-	233	Safe
T4	Tie	14	-	804	-	-	-	-	-	-	-	438	Safe
N1	Node (horizontal face)	110	100	15000	-	-	-	-	-	-	30.0*	450	Safe
(CCT)	Node (inclined face)	111	112	16800	-	-	-	-	-	-	30.0*	504	Safe
	Node (vertical face)	107	100	15000	-	-	-	-	-	-	30.0*	450	Safe
N2	Node (horizontal face)	110	100	15000	-	-	-	-	-	-	34.0*	510	Safe
(CCC)	Node (vertical face)	107	80	12000	-	-	-	-	-	-	34.0*	408	Safe
	Node (inclined face)	102	80	12000	-	-	-	-	-	-	34.0*	408	Safe
	Node (inclined face)	110	104	15600	-	-	-	-	-	-	34.0*	530	Safe

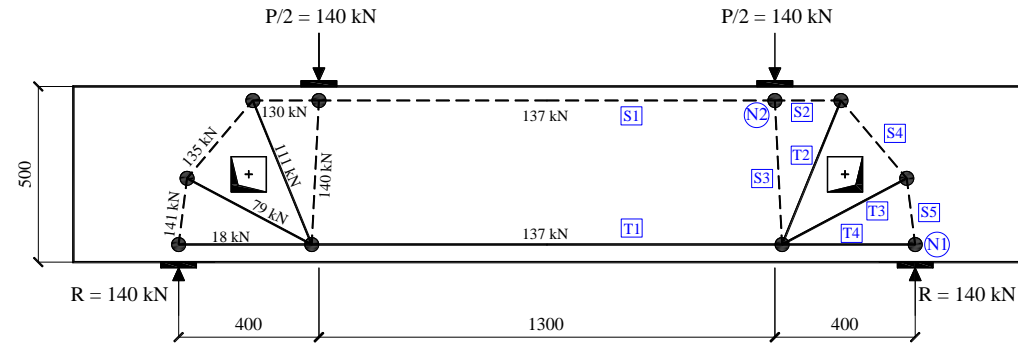* for CCC node stress limit = 0.85 f'_c and for CCT node stress limit = 0.75 f'_c

Figure 6.14: Schematic drawing of the internal forces of D-III-2S at failure ($P_u = 280$ kN)

Table 6.14: STM calculations for D-III-2S at failure ($P_u = 280$ kN)

Element	Type	F_i	w_s or w_n	Area	Adjoining tie	$\varepsilon_f/2$	θ_s	ε_1	F_{cu}	$0.85f'_c$	Selected stress limit	F_{ni}	Status
		(kN)	(mm)	(mm^2)			(degree)		(MPa)	(MPa)	(MPa)	(kN)	
S1	Strut	137	80	12000	-	-	-	0	50.0	34.0	34.0	408	Safe
S2	Strut	130	80	12000	T2	0.0023	67.7	0.0030	30.7	34.0	30.7	368	Safe
S3	Strut	140	104	15600	T1	0.0004	87.1	0.0004	45.8	34.0	8.9	139	Failed
		140	104	15600	T2	0.0023	25.1	0.0216	8.9				
		140	104	15600	T3	0.0016	64.9	0.0024	33.2				
		140	104	15600	T4	0.0001	87.1	0.0001	49.4				
S4	Strut	135	113	16950	T2	0.0023	62.5	0.0034	29.0	34.0	29.0	492	Safe
		135	113	16950	T3	0.0016	77.7	0.0018	36.4				

Table 6.14: STM calculations for D-III-2S at failure (Pu = 280 kN) (Continued)

Element	Type	F_i (kN)	w_s or w_n (mm)	Area (mm^2)	Adjoining tie	$E_f/2$	θ_s (degree)	ε_1	F_{cu} (MPa)	$0.85f'_c$ (MPa)	Selected stress limit (MPa)	F_{ni} (kN)	Status
S5	Strut	141	112	16800	T3	0.0016	69.3	0.0021	34.6	34.0	34.0	571	Safe
		141	112	16800	T4	0.0001	82.7	0.0001	49.1				
T1	Tie	137	-	804	-	0.0008	-	-	-	-	-	438	Safe
T2	Tie	111	-	150	-	0.0045	-	-	-	-	-	465	Safe
T3	Tie	79	-	150	-	0.0032	-	-	-	-	-	465	Safe
T4	Tie	18	-	804	-	0.0001	-	-	-	-	-	438	Safe
N1	Node (horizontal face)	140	100	15000	-	-	-	-	-	-	30.0*	450	Safe
(CCT)	Node (inclined face)	141	112	16800	-	-	-	-	-	-	30.0*	504	Safe
	Node (vertical face)	137	100	15000	-	-	-	-	-	-	30.0*	450	Safe
N2	Node (horizontal face)	140	100	15000	-	-	-	-	-	-	34.0*	510	Safe
(CCC)	Node (vertical face)	137	80	12000	-	-	-	-	-	-	34.0*	408	Safe
	Node (inclined face)	130	80	12000	-	-	-	-	-	-	34.0*	408	Safe
	Node (inclined face)	140	104	15600	-	-	-	-	-	-	34.0*	530	Safe

* for CCC node stress limit = 0.85 f'_c and for CCT node stress limit = 0.75 f'_c

6.4 Comparative Analysis

A comparison between the STM predictions and the experimental results is illustrated in Table 6.15. It was found that the STM predictions based on ACI 318-14 [1] were noticeably more accurate than those based on CSA S806 [5]. The predicted-to-measured strength ratio based on ACI 318-14 [1] was on average 1.01 with a minimum of 0.89 and a maximum of 1.12. The standard deviation was 0.09 while the coefficient of variation was 0.09. On the other hand, the STM predictions based on CSA S806 [5] were conservative except for the solid deep beam where the predicted strength was 31% higher than that recorded experimentally. The predicted-to-measured strength ratio was on average 0.71 with a minimum of 0.41 and a maximum of 1.31. The standard deviation was 0.29 and the coefficient of variation was 0.41. The STM prediction based on CSA S806 [5] was very sensitive to the number and orientation of ties in the truss model. The CSA S806 [5] provided very conservative prediction for the load capacity of STM III specimens. This occurred because of the increase in the number of ties and the existence of a small angle (25.1°) between the failed strut (S3) and the adjoining tie (T2). For efficient STM modeling, it is recommended to minimize the number of ties and avoid using a small angle between a strut and adjoining ties.

Table 6.15: Comparison between STM predictions and experimental results

Specimen	STM results		Experimental results	Ratios	
	P_{ACI} (kN)	P_{CSA} (kN)	P_{EXP} (kN)	P_{ACI}/P_{Exp}	P_{CSA}/P_{Exp}
Solid	562	738	565	0.99	1.31
D-I-1S	470	368	528	0.89	0.70
D-I-2S	636	480	658	0.97	0.73
D-II-1S	518	352	573	0.90	0.61
D-II-2S	640	422	572	1.12	0.74
D-III-1S	586	220	531	1.10	0.41
D-III-2S	636	280	586	1.09	0.48
Average				1.01	0.71
Standard deviation				0.09	0.29
Coefficient of variation				0.09	0.41

P_{ACI} = predicted load capacity by ACI 318-14 provisions
P_{CSA} = predicted load capacity by CSA S806 provisions

6.5 Summary

The load capacities of the tested specimens were calculated using STM procedures. The STM calculations were based on the provisions of ACI 318-14 [1] and CSA S806 [5]. The strength predictions were compared to the experimental data. Accordingly, the accuracy and validity of STM to predict the load capacity of the tested deep beams were investigated. The next chapter focuses on the development of numerical models. Numerical predictions will also be compared to experimental results in the following chapter.

Chapter 7: Numerical Modeling and Simulation

7.1 Introduction

All test specimens were analyzed numerically by three-dimensional (3D) finite element (FE) models using ATENA 3D software developed by Červenka Consulting [47]. It is a powerful tool to simulate the behavior of complex RC structures. It was utilized in this research to predict the nonlinear response of the tested specimens as they were specified as deep beams with extreme discontinuities.

7.2 Material Constitutive Laws

The mechanical properties of concrete and reinforcements were used as input data for defining the behavior of each material. The software provides built-in material constitutive models which requires few inputs from the user. In addition, it provides alternative models where the user has space to manually adjust material constitutive models.

7.2.1 Concrete Constitutive Models

Two material constitutive models for the concrete were studied in this research. The first model was a predefined model in the software. The model name as in the software is "CC3DNonLinCementitious2" which is designated in this research as DEFAULT model. The second used material constitutive model for concrete was named in the software as "CC3DNonLinCementitious2User". It is designated as USER model. For both material constitutive models (DEFAULT and USER), the software requires the user to input the cube compressive strength of concrete (f_{cu}). The rest of the concrete properties are autogenerated by the software

using built-in equations. However, the user has more space to edit and modify key values of the material constitutive laws.

7.2.1.1 The DEFAULT Concrete Constitutive Model

In the DEFAULT concrete constitutive model, the user is allowed to change few parameters such as concrete cylinder compressive strength, tensile strength, elastic modulus and etc. The model considers concrete behavior under compression (plastic) and tension (fracturing). The hardening/softening plasticity model is based on Menétrey-Willam failure surface [48]. However, the fracture model is based on the classical orthotropic smeared crack formulation and crack band model. The fracture model employs Rankine failure criterion. The combination of the two behavior models allows simulating concrete crushing under high confinement, cracking, and crack closure due to crushing in other directions.

The stress-strain relationship of concrete under compression is mainly composed of ascending and descending branches. The law of the ascending branch is based on the strains, while the descending branch is based on displacements. The ascending branch begins by linear relation with a slope equals to E_c up to a compressive stress value of f'_{co} which is equal to $2f'_t$, where E_c = concrete modulus of elasticity and f'_t = uniaxial concrete tensile strength. Then the curve is continued by a nonlinear elliptical segment until the stress reaches concrete cylinder compressive strength (f'_c). The function of the curve is given by Eq. (7.1), Where σ_c = compressive stress, f'_{co} = compressive stress at the onset of nonlinear compressive behavior, ε_p = plastic strain, and ε_{cp} = plastic strain at compressive strength. Figure 7.1 demonstrates the compressive hardening behavior.

$$\sigma_c = f_{co} + (f'_c - f_{co})\sqrt{1 - \left(\frac{\varepsilon_{cp} - \varepsilon_p}{\varepsilon_{cp}}\right)^2} \qquad (7.1)$$
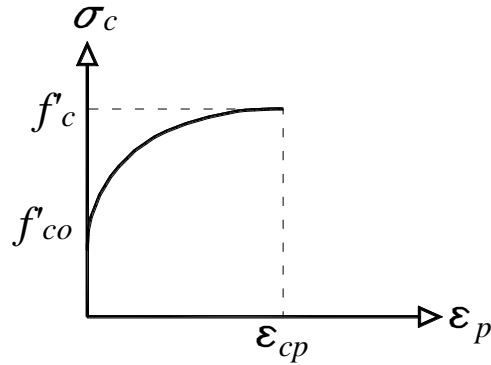
$$f'_{co} = 2f'_t \qquad (7.2)$$

Figure 7.1: Concrete compressive hardening

The descending branch of the concrete compressive stress-strain curve is assumed to be linear. The stress is inversely proportional to the displacements (w_c) through the length scale (L_c). The displacement w_c is a function of the plastic strain (ε_p) as expressed in Eq. (7.3). Where ε_{cp} is plastic concrete strain at compressive strength and L_c corresponds to the projection of element size into the direction of minimal principal stresses as shown in Figure 7.2. The stress reaches zero when the displacement is equal to w_d. where w_d is the plastic displacement which is equal to 0.5 mm for normal concrete [49].

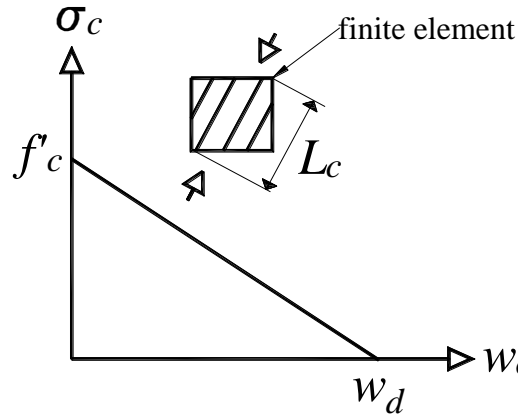$$w_c = (\varepsilon_p - \varepsilon_{cp}) L_c \qquad (7.3)$$

Figure 7.2: Concrete compressive softening

The concrete compressive strength in a direction parallel to the cracks is reduced based on the compression field theory as proposed by Vecchio and Collins [50]. The reduced compressive strength (f'^{ef}_c) is a function of f'_c and compressive strength reduction factor (r_c) given by Eq. (7.5), where ε_1 = strain in a direction normal to the crack and r_c^{lim} = minimum value for the reduction factor taken as 0.8 [51].

$$f'^{ef}_c = r_c f'_c \tag{7.4}$$

$$r_c = \frac{1}{0.8 + 170\varepsilon_1}, \qquad r_c^{lim} \leq r_c \leq 1 \tag{7.5}$$

For the stress-strain curve under tension, the curve begins with linear relation with the same slope of the linear ascending portion of compressive stress-strain curve which is equal to the concrete modulus of elasticity (E_c). The relation stays linear until the tensile stress (σ_t) reaches the concrete tensile strength (f_t). Then, the stress-strain relation turns into exponential decay based on the crack opening displacement (w_t) computed from the fracturing strain (ε_f) multiplied by crack band length (L_t) as in Eq. (7.6). L_t is assumed to be equal to the size of the element projected into the

crack direction as shown in Figure 7.3. The fracture energy of the concrete needed to create a unit area of stress-free crack (G_f) determines the value of crack opening at the complete release of stress (w_{tc}).
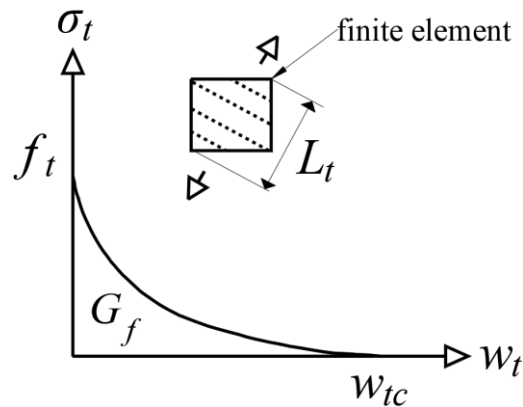
$$w_t = \varepsilon_f \, L_t \qquad (7.6)$$

Figure 7.3: Concrete tensile softening

The modified compression field theory [50] was adopted in ATENA to calculate the shear strength of a cracked concrete (τ_{ef}) using Eq. (7.7). Where, a_g = maximum aggregate size, w = maximum crack width at the given location.

$$\tau_{ef} = \frac{0.18 \sqrt{f'_c}}{0.31 + \dfrac{24w}{a_g + 16}} \qquad (7.7)$$

The following table shows the concrete properties in FE models using the DEFAULT material model. The principal input was the cube compressive strength which was 48 MPa based on the experimental testing. However, two properties were manually modified: the cylinder compressive strength (f'_c) which was entered as the measured value (40 MPa) and the tensile strength (f_t) which was taken as half of

measured splitting tensile strength (1.7 MPa) [52]. All other properties were generated by the software using built-in equations.

Table 7.1: Concrete properties of the DEFAULT model

Parameter	Description	Value
f_{cu}	Cube compressive strength	-48 MPa
f'_c	Cylinder compressive strength	-40 MPa
f_t	Tensile strength	1.7 MPa
E_c	Elastic modulus	3.641×10^4 MPa
μ	Poisson's ratio	0.2
G_f	Specific fracture energy	7.925×10^{-5} MN/m
w_d	Critical compressive displacement	-5×10^{-4} m
ε_{cp}	Plastic strain at compressive strength	-1.12×10^{-3}
$r_{c,lim}$	Reduction of compressive strength due to cracks	0.8
a_g	Maximum aggregate size	0.02 m

7.2.1.2 The USER Concrete Constitutive Model

The constitutive laws in tension and compression of the USER model are almost similar to those of the DEFAULT model until the peak stress is reached at a strain value of ε_{loc}, after which the strain is localized to the finite element. The value of ε_{loc} is generated automatically by the software as a function of the cube concrete strength. For the given cube strength of the concrete used in the current study (48 MPa), the value of ε_{loc} in tension was almost equal to zero, while in compression it was equal to 0.00112. The post-peak localized strain is affected by the L/L_{ch} ratio, where L = crushing band size for the compression behavior or crack band size for the tension behavior and L_{ch} = characteristic length having a default value generated by the software of 0.1 for the compression behavior and 0.03 for the tension behavior. It

is recommended to manually change the value of characteristic length in tension to be equal to the mesh size [47]. To examine the effect of the characteristic length value on FE models prediction, three alternatives were developed for the USER model. In the first alternative, the value of characteristic length in compression and tension were kept as generated by the software, whereas in the other two alternatives, the value of characteristic length in tension only or in tension and compression were changed to match the mesh size. Figure 7.4 shows the compressive behavior and the tensile softening relationships as generated by the software for the given cube concrete strength adopted in the current study.
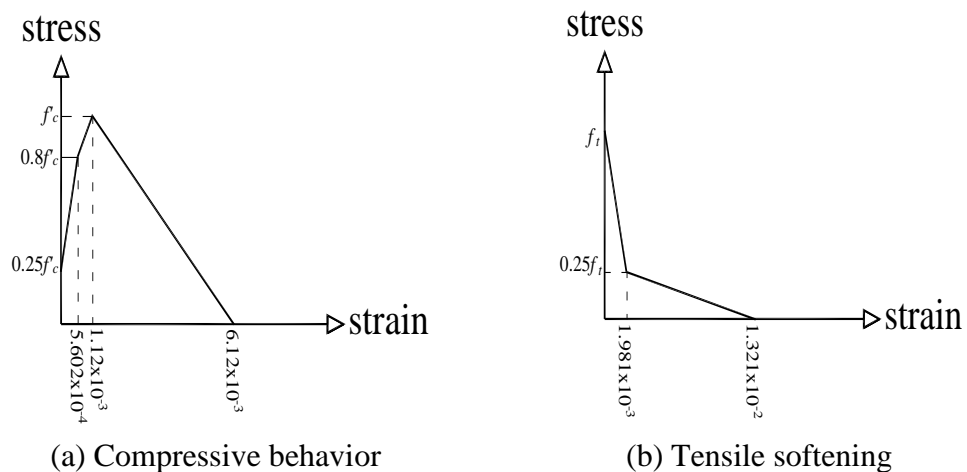

(a) Compressive behavior   (b) Tensile softening

Figure 7.4: USER concrete material model

The USER model considers a reduction in strength for cracked concrete. It assigns a reduction factor (r_c) for the compressive strength and (f_{sh}) for the shear strength. The compressive strength reduction factor is affected by the fracturing strain (ε_f) calculated from the strain tensor at the finite element integration points, whereas the shear strength reduction factor is affected by the fracturing strain after localization ($\tilde{\varepsilon}_f$) determined by Eq. (7.8). Figure 7.5 shows the change in the shear

and compressive strength reduction factors as per multilinear functions generated by the software.

$$\tilde{\varepsilon}_f = \varepsilon_{loc} + (\varepsilon_f - \varepsilon_{loc}) {}^L\!/_{L_{ch}} \qquad (7.8)$$

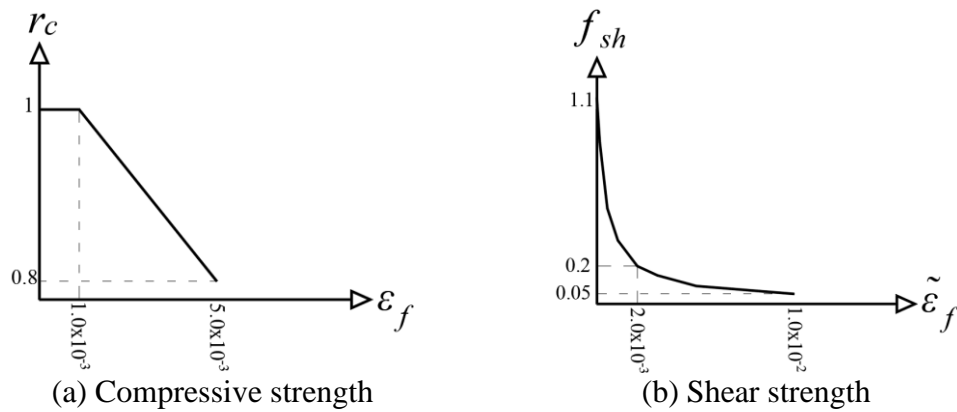(a) Compressive strength (b) Shear strength

Figure 7.5: Functions of reduction factors in the USER model

The displayed values of parameters of the USER concrete model by the software are presented in Table 7.2. The values of the cylinder compressive strength and the tensile strength were adjusted manually as done in the DEFAULT model to match the experimentally measured concrete properties. The characteristic length in tension and compression behavior were either kept unchanged as generated by the software or changed to be equal to the mesh size. Each option was tested in a separate run.

Table 7.2: Concrete properties of USER model

Parameter	Description	Value
f_{cu}	Cube compressive strength	-48 MPa
f'_c	Cylinder compressive strength	-40 MPa
f_t	Tensile strength	1.7 MPa
E_c	Elastic modulus	3.641×10^4 MPa
μ	Poisson's ratio	0.2
$\varepsilon_{loc, f}$	Localized fracturing strain	≈ 0
$L_{ch, t}$	Tensile characteristic length	0.03 m or mesh size
$\varepsilon_{loc, p}$	Localized plastic strain	-1.12×10^{-3}
$L_{ch, c}$	Compressive characteristic length	0.1 m or mesh size

7.2.2 Steel Stress-Strain Response

The stress-strain relation of the reinforcing steel bars was assumed to be bilinear. The stress started to increase linearly proportional to the strain with a slope equals to Young's modulus of steel (E_s) until yielding. Then, the stress was assumed to be constant and equal to the steel yield strength (f_y). The measured yield strength of the steel bars was 544 MPa, whereas the value of E_s was measured as 200 GPa. A linear-elastic behavior was assigned to the steel plates at the support and loading points.
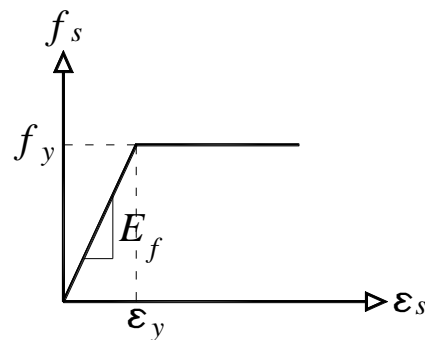

Figure 7.6: Bilinear stress-strain response of steel bars

7.2.3 CFRP Stress-Strain Response

The stress-strain relationship of CFRP was assumed to be linear elastic as shown in Figure 7.7, where f_f = stress in CFRP, ε_f = strain in CFRP, f_{fu} = ultimate strength (3100 MPa), ε_{fu} = ultimate strain (0.019) and E_f = Young's modulus of CFRP which is equal to 165 GPa.
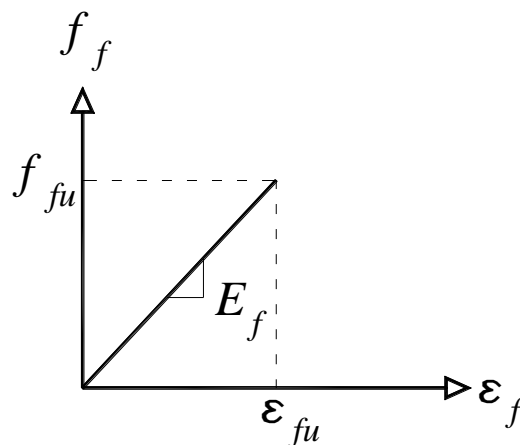

Figure 7.7: CFRP stress-strain response

7.2.4 Bond-Slip Model

The bond between the reinforcing steel bars and surrounding concrete was assumed as a perfect connection. To evaluate the effect of inclusion of a bond-slip model between the CFRP and the concrete on numerical results, two models were developed for each specimen strengthened with NSM-CFRP. In one model, a perfect bond was assumed between the CFRP and the concrete whereas in the other model an interfacial bond-slip model was adopted between the CFRP and the concrete. The bond-slip model developed by Ceroni et al. [53] for the same type of CFRP strips and bonding adhesive used in this research was adopted. This model is shown in Figure 7.8.
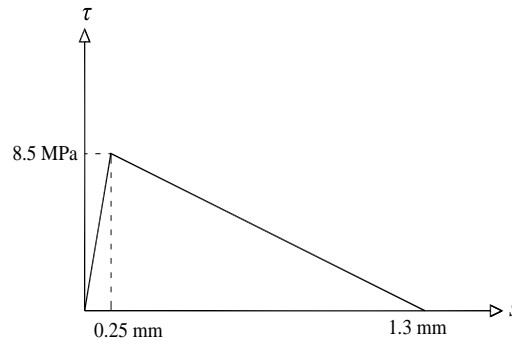
Figure 7.8: NSM-CFRP bond-slip model [53]

7.3 Element Types

The concrete beam and steel plates were modeled as solid 3D macro-elements. Openings were then generated in the desired beam models. Steel and NSM-CFRP reinforcement were modeled as discrete reinforcement embedded in the concrete beam. The reinforcements are active in one direction only which is the longitudinal direction of the reinforcements. In the software user's manual [47], it is recommended to model half of concrete beams to reduce the running time. However, a quarter of the beam was modeled as the beam is symmetric around the middle section along beam length and along the width. The planes of symmetry are demonstrated in Figure 7.9. Modeling of one quarter of the beam helped to shorten the processing time of the model and allowed to include a mesh size of 15 mm in the mesh sensitivity analysis. Figure 7.10 shows an example of FE model of deep beam with an opening strengthened by NSM-CFRP.
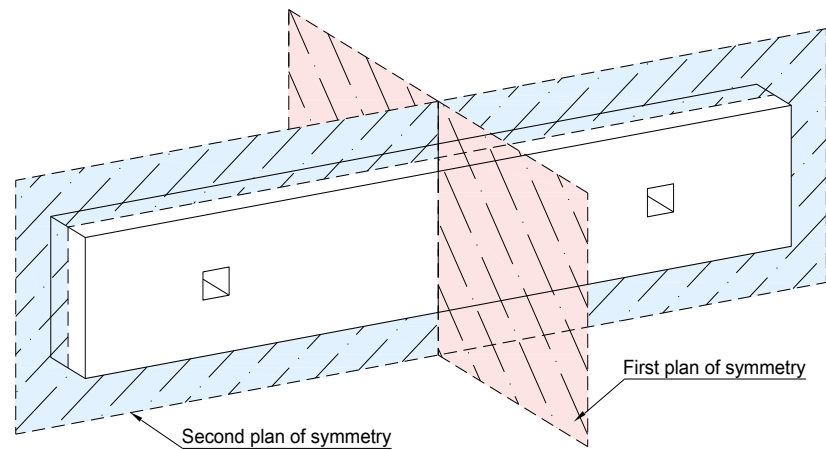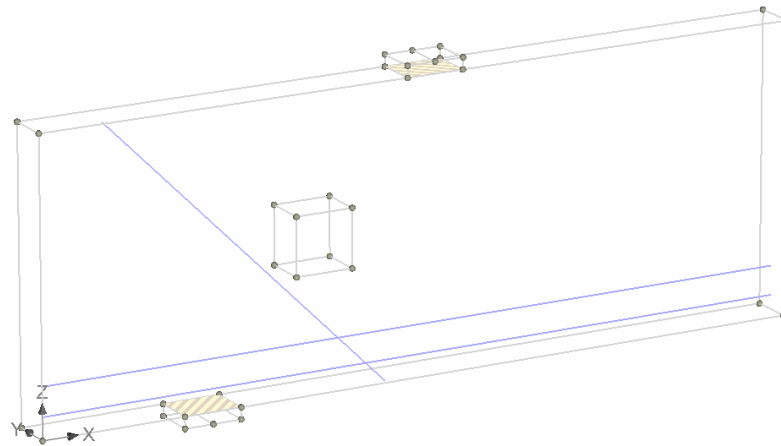
Figure 7.9: Planes of symmetry

Figure 7.10: Finite element model layout

7.4 Monitoring Points

Several monitoring points were added to the FE models to obtain a numerical data corresponding to the obtained data from experimental testing. Numerical values of the applied load, midspan deflection, and steel and CFRP strains values were obtained using the monitoring points. The input parameters for all types of monitoring points used in the FE models are shown in Table 7.3. The type and value specify the desired measurement that will be monitored closest to the coordinates

that are provided in monitor location inputs. The component number specifies the direction of the monitored value. Components1, 2, and 3 represent directions in X, Y, and Z, respectively. Figure 7.11 shows an example of the locations of monitoring points in FE model.

Table 7.3: Input parameters of monitoring points

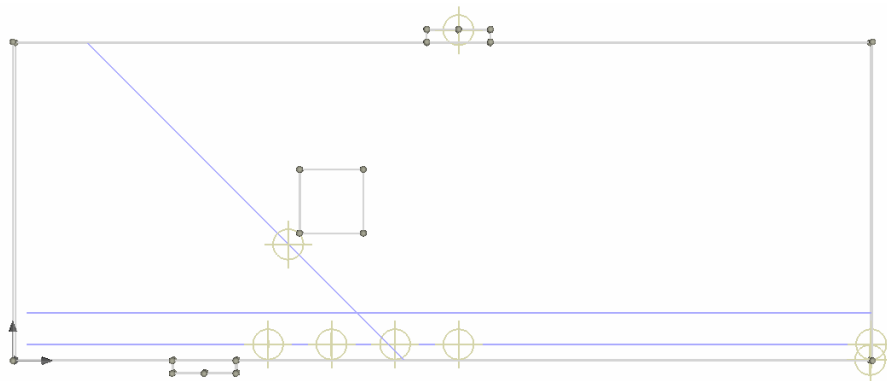| Title	Type	Value	Item
Load	Value at node	Reaction	Component 3
Deflection	Value at node	Displacement	Component 3
Steel strain	Value at integration point	Strain	Component 1
CFRP strain	Value at integration point	Strain	Component 1

Figure 7.11: Locations of monitoring points

7.5 Boundary Conditions and Loading

The defined boundary conditions were employed to simulate the real experiment and provide the stability of the structure. The support plate was restricted from movement in transverse and vertical directions (Y and Z axis, respectively). These restrictions were applied at a midline of the bottom surface of the steel plate. As a quarter of the beam was modeled, the surfaces at plans of symmetry were

restrained from the movement in the direction toward the other symmetrical part of the beam through using surface supports as shown in Figure 7.12. The applied load was displacement-controlled loading defined as prescribed vertical displacement at midpoint of the top surface of loading plate. The change in displacement for each step was 0.1 mm. The predefined standard Newton-Raphson iterative solution method was adopted in the FE analysis.
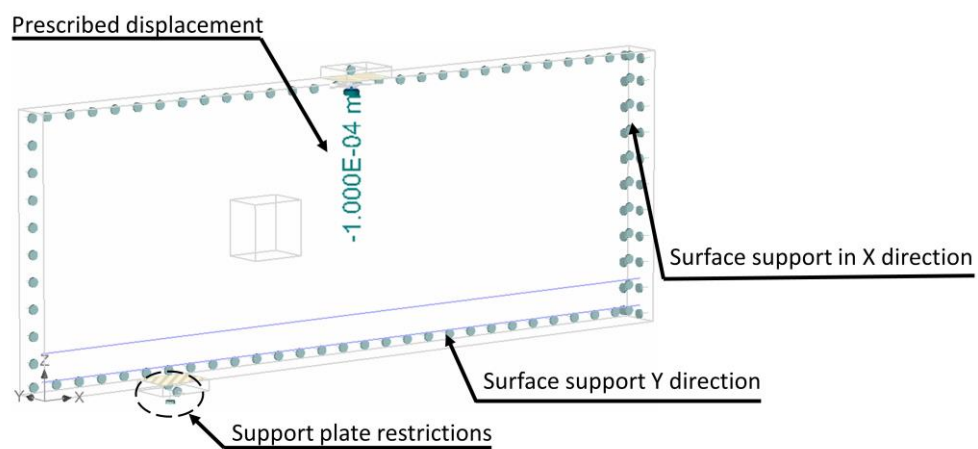

Figure 7.12: Supports and prescribed displacement

7.6 Mesh Sensitivity Analysis

Brick mesh type was not applicable for all models, even though the beams are considered as regular shape. The generation of brick mesh requires macro-elements that have six boundary surfaces. This is applicable for a solid deep beam. Installation of an opening added four surfaces to the model which prevented the generation of a brick mesh. As such, a tetrahedral mesh was used in all FE models.

In the User's Manual of ATENA 3D [47], it is recommended to have a minimum of 4 to 6 elements per thickness of the beam which corresponds to a mesh size in the range of 37.5 to 25 mm. Preliminary models were developed using the

DEFAULT concrete material model to conduct a mesh sensitivity analysis, and hence, decide the mesh size. In fact, as the mesh size becomes smaller, the software computational time becomes significantly longer. As a first trial, models have been run using mesh sizes of 25 and 20 mm on half beam models. Adopting a mesh size smaller than 20 mm was not possible in half beam models because the software did not function. Table 7.4 shows the predicted load capacities by the half beam models with 20 and 25 mm mesh size. Models with a mesh size of 20 mm exhibited lower load capacities than those of the models with 25 mm mesh size. The difference was on average 5% with minimum of 2% and maximum of 9%.

Table 7.4: Load capacity of half beam models with different mesh sizes

Specimen	F_{25}	F_{20}	$\dfrac{F_{20}}{F_{25}}$
	(kN)	(kN)	
Solid	748	718	0.96
D-NS	516	468	0.91
D-I-1S	578	528	0.91
D-I-2S	654	600	0.92
D-II-1S	588	564	0.96
D-II-2S	646	624	0.97
D-III-1S	626	614	0.98
D-III-2S	740	712	0.96
Average			0.95
Standard deviation			0.03
Coefficient of variation			0.03

F_{25} = load capacity when mesh size was 25 mm
F_{20} = load capacity when mesh size was 20 mm

To run the models with a 15 mm mesh size, quarter beam models were developed. Predictions of the quarter models were compared to those of the half models in Figure 7.13. The results of quarter models were almost identical to those of the half model counterparts irrespective of the mesh size. Quarter beam models

were run using 25, 20, and 15 mm mesh sizes. Table 7.5 shows the load capacities of the quarter beam models. It can be seen that the load capacity tended to decrease as the mesh size decreased. Based on the results of the mesh sensitivity analysis, it was decided to use quarter beam model with a mesh size of 15 mm.
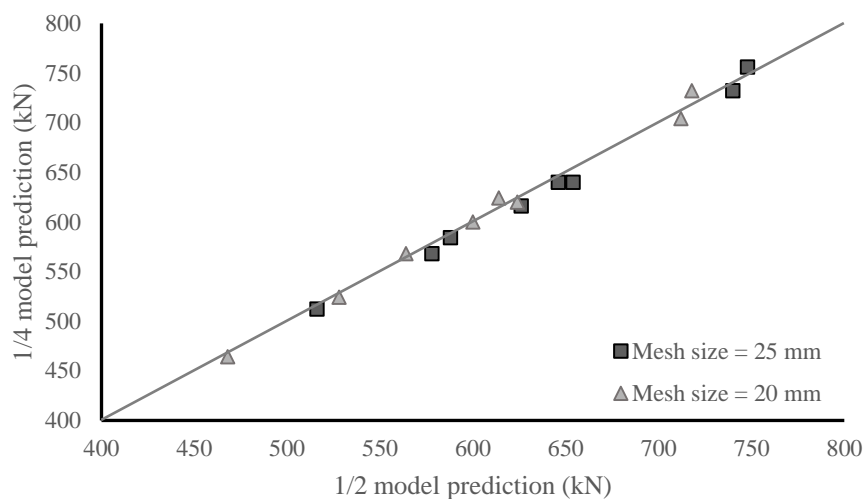

Figure 7.13: Predictions of quarter beam model vs predictions of half beam model

Table 7.5: Load capacity of quarter beam models with different mesh sizes

Specimen	F_{25} (kN)	F_{20} (kN)	F_{15} (kN)	$\dfrac{F_{20}}{F_{25}}$	$\dfrac{F_{15}}{F_{20}}$	$\dfrac{F_{15}}{F_{25}}$
Solid	756	732	664	0.97	0.91	0.88
D-NS	512	464	440	0.91	0.95	0.86
D-I-1S	568	524	496	0.92	0.95	0.87
D-I-2S	640	600	560	0.94	0.93	0.88
D-II-1S	584	568	544	0.97	0.96	0.93
D-II-2S	640	620	620	0.97	1.00	0.97
D-III-1S	616	624	584	1.01	0.94	0.95
D-III-2S	732	704	696	0.96	0.99	0.95
Average				0.96	0.95	0.91
Standard deviation				0.03	0.03	0.04
Coefficient of variation				0.03	0.03	0.03

F_{25} = load capacity when mesh size was 25 mm
F_{20} = load capacity when mesh size was 20 mm
F_{15} = load capacity when mesh size was 15 mm

7.7 Effect of Bond at CFRP-Concrete Interface

Table 7.6 presents the results of FE models with and without a bond-slip law at CFRP-concrete interface. The inclusion of the bond-slip law in the FE models was expected to reduce the predicted load capacity. Nevertheless, the load capacity of the models with and without a bond-slip law at CFRP-concrete interface were almost identical. Hence, it can be concluded that the inclusion of a bond-slip law for NSM-CFRP shear reinforcement has no effect on numerical prediction and the assumption of a perfect bond between the CFRP and concrete is valid for numerical modeling of such cases.

Table 7.6: Load capacities of models with and without bond-slip

Specimen	Concrete material model					
	DEFAULT			USER		
	$F_{prefect}$[1] (kN)	$F_{bond\text{-}slip}$[2] (kN)	$\frac{F_{bond-slip}}{F_{prefect}}$	$F_{prefect}$[1] (kN)	$F_{bond\text{-}slip}$[2] (kN)	$\frac{F_{bond-slip}}{F_{prefect}}$
D-I-1S	496	496	1.00	476	452	0.95
D-I-2S	560	546	0.98	512	496	0.97
D-II-1S	544	536	0.99	484	484	1.00
D-II-2S	620	621	1.00	584	576	0.99
D-III-1S	584	599	1.03	564	548	0.97
D-III-2S	696	726	1.04	632	644	1.02
Average			1.01			0.98
Standard deviation			0.03			0.02
Coefficient of variation			0.03			0.03

[1] perfect bond between CFRP and concrete
[2] the cohesion strength is a function of bond-slip model

7.8 Comparative Analysis

The numerical and experimental results are compared in this section. As mentioned earlier, several numerical models were developed to examine the effect of

input parameters on the accuracy of the models' predictions. Table 7.7 reports the load capacity predictions for the deep beam specimens using the DEFAULT and USER material models. There are three predictions values under USER material model for each specimen. They differ based on the input value of the characteristic length in tension ($L_{ch,t}$) and compression ($L_{ch,c}$). The use of the DEFAULT concrete material model overestimates the load capacity of specimens Solid, D-NS, and D-III-2 by 18%, 30%, and 19%, respectively. The use of the USER model reduced the predicted load capacity, and hence, improved the accuracy of the numerical predictions. Overall, the use of the USER model with $L_{ch,t}$ equals mesh size (0.015 m) and $L_{ch,c}$ equals the default value (0.1 m) provided the most accurate prediction for the load capacity of the tested specimens. The difference between the numerical predictions and experimental readings did not exceed 10% except for two models D-I-2S and D-II-1S with P_{FE}/P_{EXP} ratio of 0.78 and 0.84, respectively. The ratio of P_{FE}/P_{EXP} was on average 0.97 with a corresponding standard deviation and coefficient of variation of 0.12. As such, the USER concrete material model with $L_{ch,t}$ equals mesh size (0.015 m) and $L_{ch,c}$ equals the default value (0.1 m) was adopted in the analysis to simulate the behavior of all the tested specimens. The results of comparative analysis are presented in the following subsections.

Table 7.7: Comparison between numerical and experimental loads

Specimen	Experimental results	Numerical concrete material model							
		DEFAULT		USER					
				$L_{ch,t} = 0.03$ $L_{ch,c} = 0.1$		$L_{ch,t} = 0.015$ $L_{ch,c} = 0.1$		$L_{ch,t} = 0.015$ $L_{ch,c} = 0.015$	
	P_{Exp}	P_{FE}	$\dfrac{P_{FE}}{P_{Exp}}$	P_{FE}	$\dfrac{P_{FE}}{P_{Exp}}$	P_{FE}	$\dfrac{P_{FE}}{P_{Exp}}$	P_{FE}	$\dfrac{P_{FE}}{P_{Exp}}$
	(kN)	(kN)		(kN)		(kN)		(kN)	
Solid	565	664	1.18	568	1.01	544	0.96	536	0.95
D-NS	338	440	1.30	412	1.22	370	1.09	349	1.03
D-I-1S	528	496	0.94	460	0.87	476	0.90	468	0.89
D-I-2S	658	560	0.85	520	0.79	512	0.78	512	0.78
D-II-1S	573	544	0.95	488	0.85	484	0.84	428	0.75
D-II-2S	572	620	1.08	568	0.99	584	1.02	492	0.86
D-III-1S	531	584	1.10	548	1.03	564	1.06	512	0.96
D-III-2S	586	696	1.19	648	1.11	632	1.08	584	1.00
Average			1.07		0.98		0.97		0.90
Standard deviation			0.15		0.14		0.12		0.10
Coefficient of variation			0.14		0.15		0.12		0.11

P_{Exp} = Experimental load capacity
P_{FE} = Predicted load capacity by numerical model
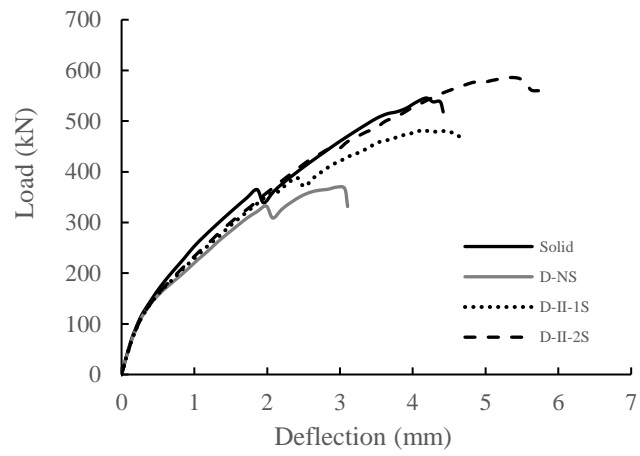
7.8.1 Load-Deflection Response

Figure 7.14 presents predicted load-deflection behavior of all specimens. The deep beam models with openings had identical responses to that of solid deep beam model unlit load decay or failure happened. The model of specimens solid, D-NS, and D-II-1S experienced a minor load decay at 62%, 83%, and 76% of the peak load, respectively. Then, the load continued to increase at the same rate up to failure. The load-deflection responses that predicted numerically are compared to those obtained from the experimental tests in Figure 7.15. The change in slope occurred at almost

the same load value recorded experimentally. The response predicted numerically tended to be stiffer than that obtained from the experiment which is typically expected in FE models. This happens probably due to the perfect bond between concrete and longitudinal steel reinforcement in the numerical models, while in the real behavior slippage could occur. In addition, the existence of microcracks generated by drying shrinkage and beam handling reduces the stiffness in actual beams behavior [39, 54, 55]. However, the predicted load-deflation responses are generally comparable to those measured experimentally.

The numerical and experimental values of the midspan deflection at ultimate load are compared in Table 7.8. The predicted deflections at ultimate load are generally in good agreement with those measured experimentally except for specimens D-NS, D-I-2S, and D-II-1S where the deflection was underestimated by 25%, 39%, and 33%, respectively. For all other specimens, the predicted deflections were within a 15% error band. It is worth noting that the deflection values of the tested specimens at the ultimate load were very small. The maximum deflection recorded experimentally was 6.1 mm. For such small values, the predicted deflections are considered in good agreement with experimental results.
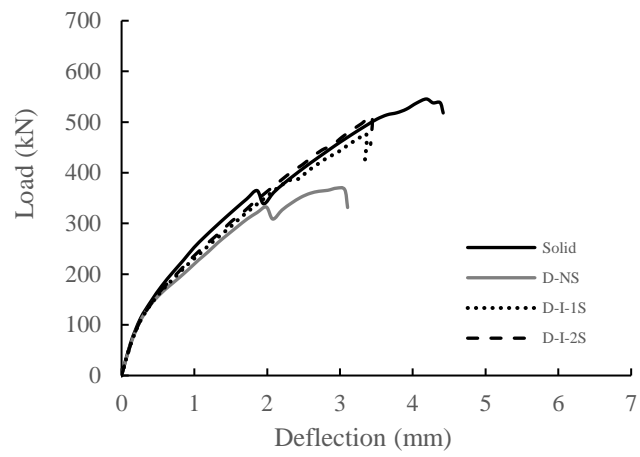
(a) STM I

(b) STM II
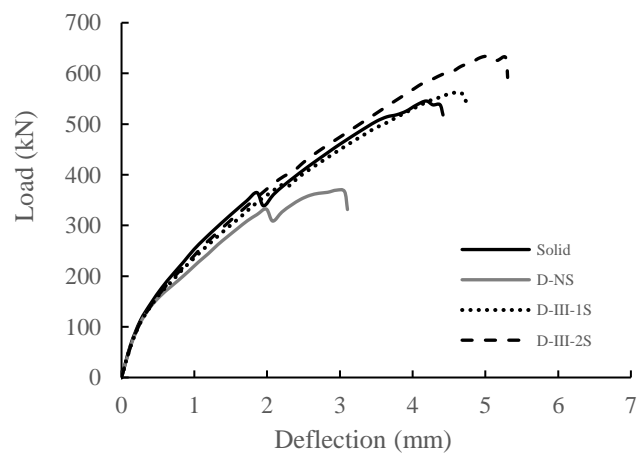
(c) STM III

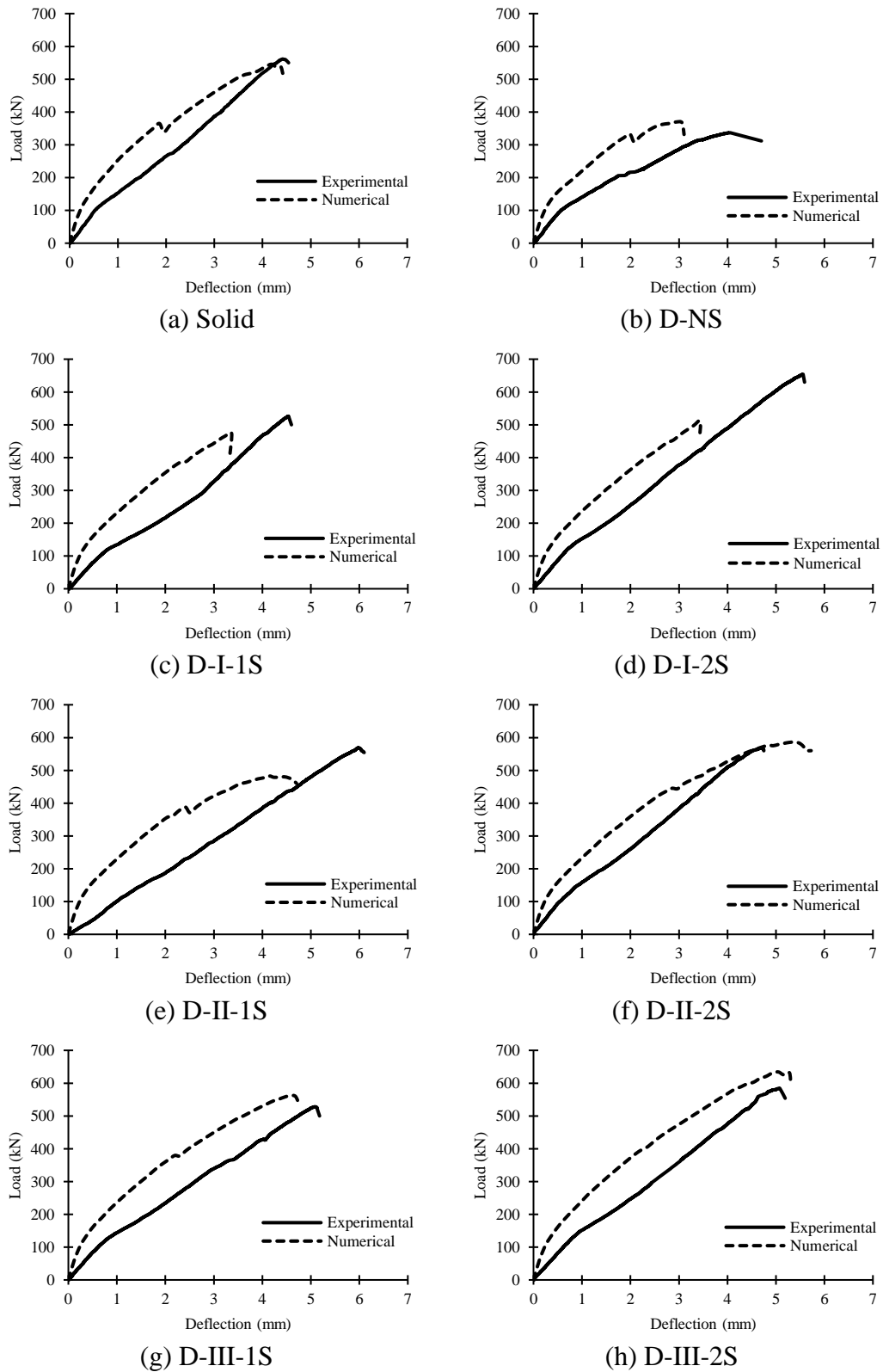Figure 7.14: Numerical load-deflection response

Figure 7.15: Numerical and experimental load-deflection responses

Table 7.8: Comparison between numerical and experimental deflections

Specimen	Δ_{Exp}	Δ_{FE}	$\dfrac{\Delta_{FE}}{\Delta_{Exp}}$
	(mm)	(mm)	
Solid	4.4	4.2	0.95
D-NS	4.0	3.0	0.75
D-I-1S	3.9	3.4	0.87
D-I-2S	5.6	3.4	0.61
D-II-1S	6.1	4.1	0.67
D-II-2S	4.7	5.4	1.15
D-III-1S	5.1	4.6	0.9
D-III-2S	5.0	5.1	1.02

Δ_{Exp} = Experimental midspan deflection at failure
Δ_{FE} = Numerical midspan deflection at failure

7.8.2 Tensile Steel Strain Response

The numerical and experimental strain responses of the tensile steel reinforcement are presented in Figure 7.16. The numerical and experimental steel strain responses showed a similar trend. In agreement with experimental findings, minimal or no steel strains were recorded numerically before cracking. In the post-cracking stage, the steel strain increased at a constant rate until failure. The solid specimen was an exception where a minor load decay occurred at 47% of the peak load. This is possibly due to initiation of a new crack. The strain values at all locations were insignificantly different which was in agreement with experimental results. It can be concluded that the FE models were able to provide realistic predictions for the reinforcement steel strains.
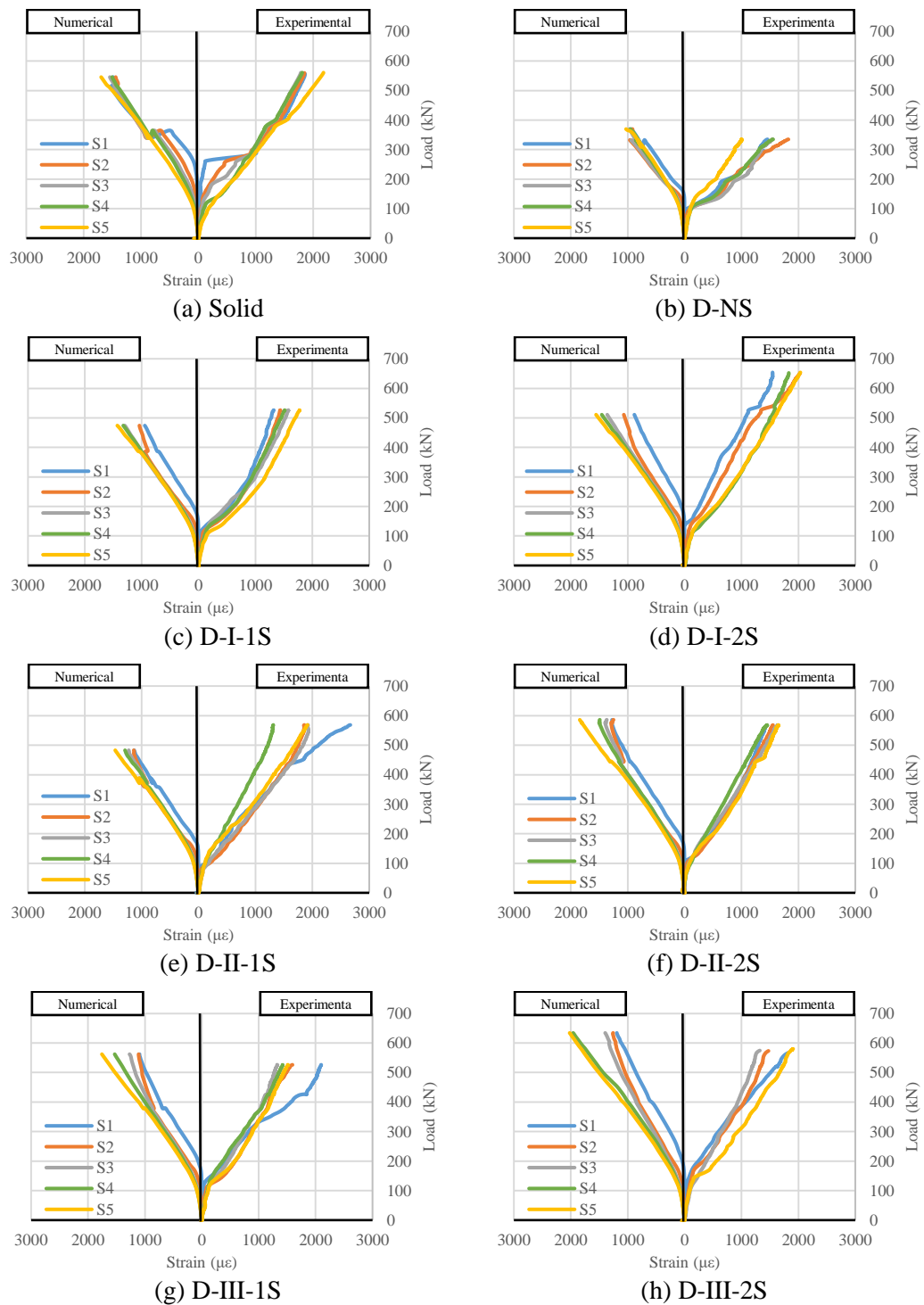
Figure 7.16: Numerical and experimental tensile steel strain responses

7.8.3 CFRP Strain Response

Figure 7.17 compares the CFRP strain responses predicted numerically with those obtained experimentally. As a quarter of the deep beam was modeled, CFRP strain values were captured in one shear span only. Using the letters "E" and "W" as an abbreviation for east and west was not applicable for the FE models. All CFRP monitoring points in the FE models were assumed to be in the east shear span just for the purpose comparison with the experimental data. In general, the numerical CFRP strain response matched the experimental response. No strain or minimal strain values were captured in the pre-cracking stage. The CFRP strain values increased at a higher rate after initiation of cracking. The numerical predictions for the strain in the CFRP reinforcement were generally in good agreement with those experimentally measured.
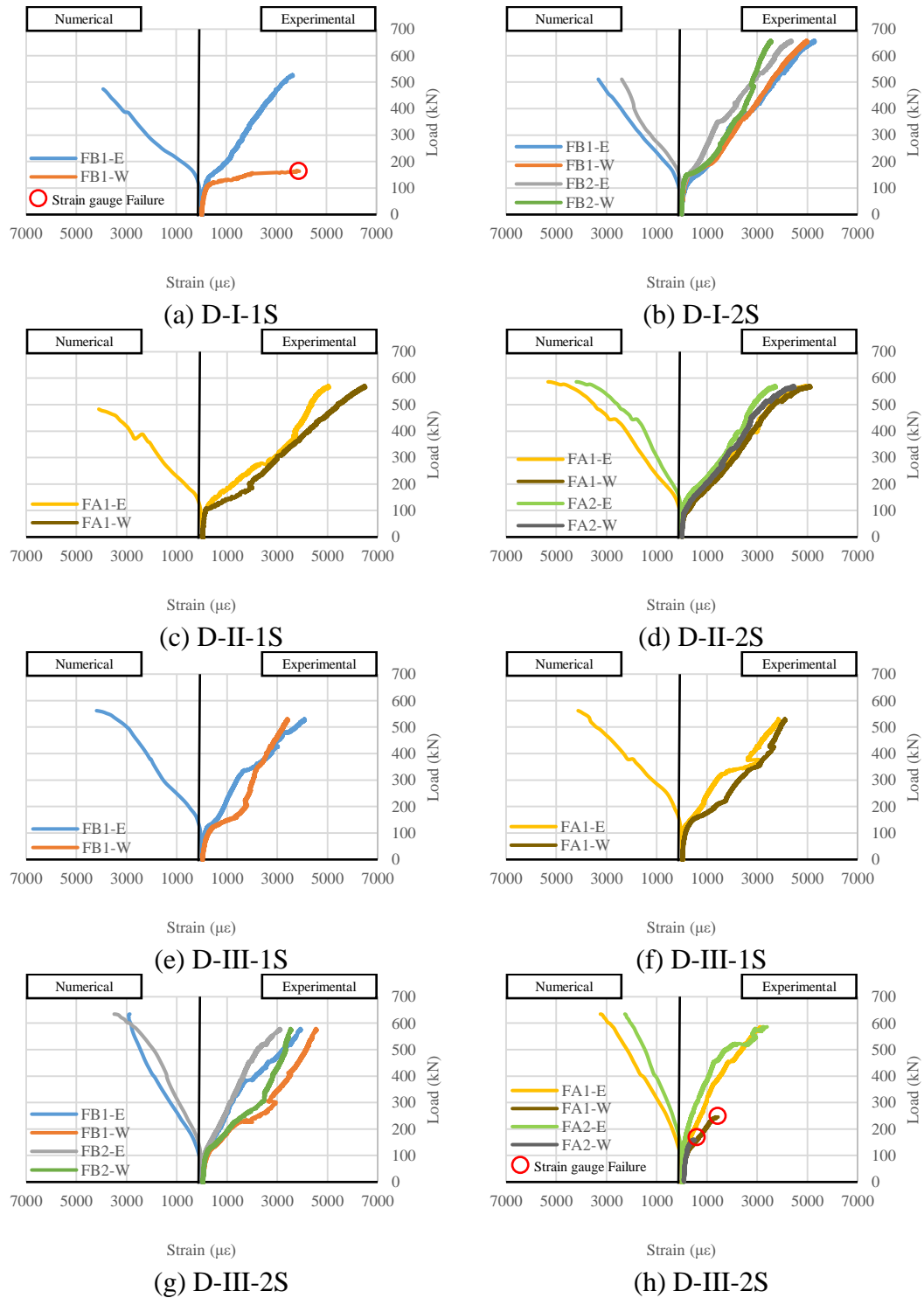
Figure 7.17: Numerical and experimental CFRP strain responses

7.8.4 Crack Pattern

The crack patterns captured numerically at failure are compared to those obtained from the tests in Figure 7.18. The photos in these figures present the crack pattern on one side of the beam where the failure occurred. The minimum width of the displayed crack in FE models was set to be 0.05 mm. It can be seen that the numerically predicted crack patterns adequately matched those captured experimentally. The FE modeling captured both shear and flexural cracks. Interestingly, the numerical model for specimen D-NS did not show any cracks in the constant moment region which was validated experimentally.
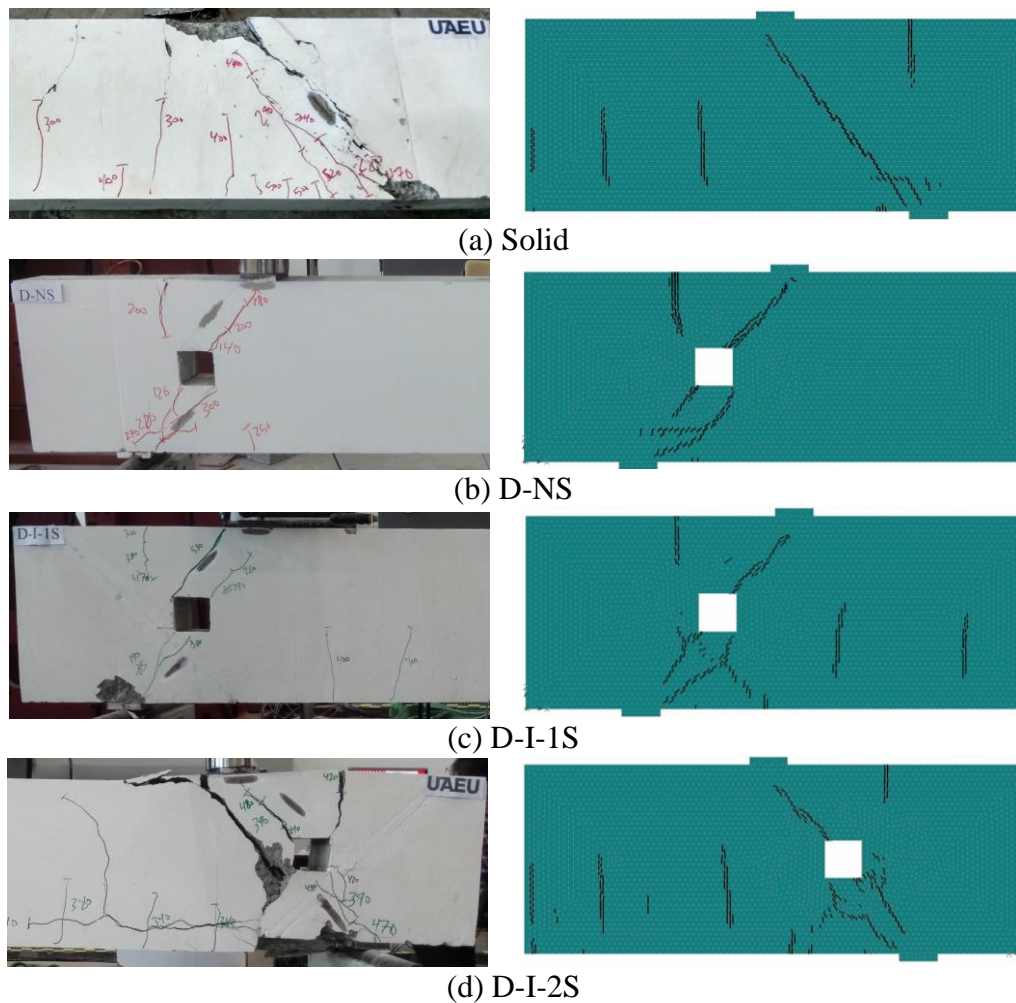
(a) Solid

(b) D-NS

(c) D-I-1S

(d) D-I-2S

Figure 7.18: Numerical versus experimental crack patterns

(e) D-II-1S

(f) D-II-2S

(g) D-III-1S

(h) D-III-2S
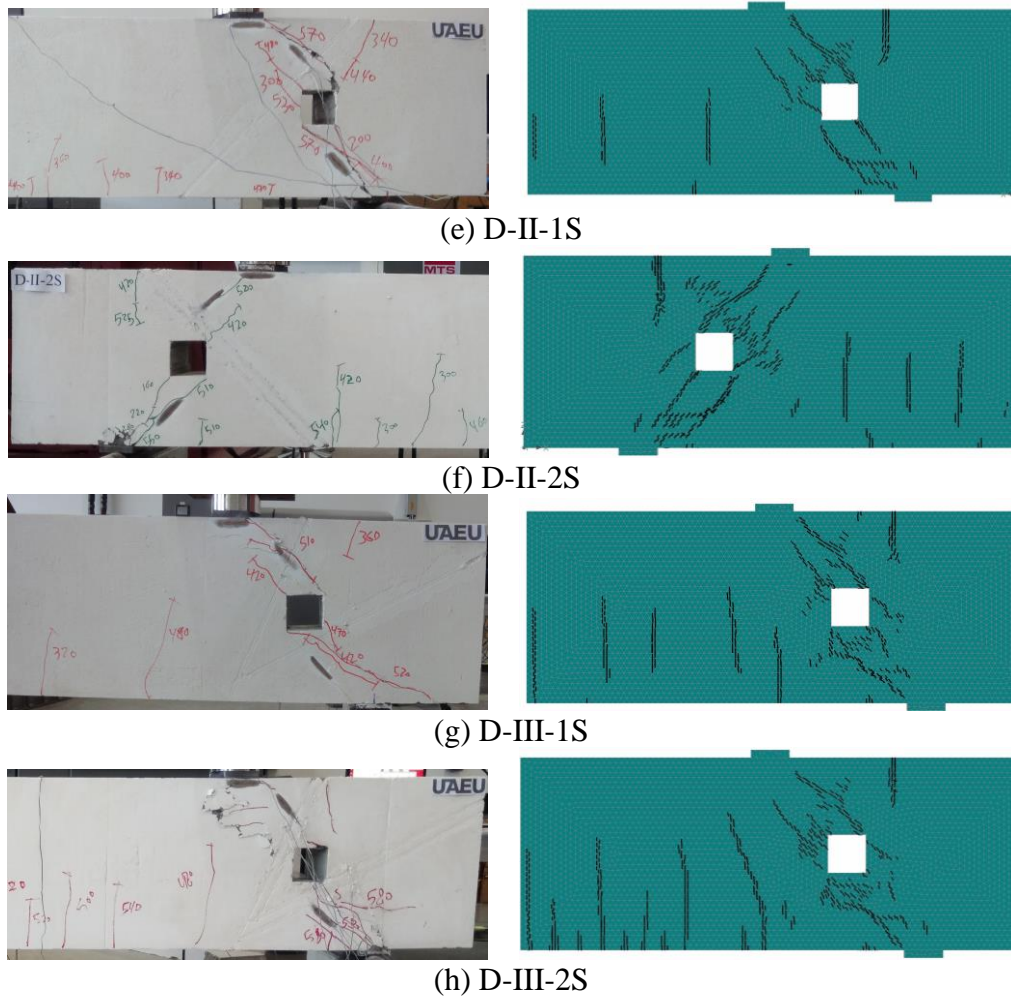
Figure 7.18: Numerical versus experimental crack patterns (Continued)

7.9 Summary

Throughout this chapter, the characteristics of the developed numerical models and the results provided by the models were presented. Multiple parameters of the numerical models were examined by developing alternative models. The model that provided the most accurate predictions for load capacity was adopted for further analysis. The adopted model accurately simulated the load deflection response, steel and CFRP strains, and crack pattern. Therefore, the objective to develop numerical model capable of predicting the nonlinear behavior of the studied deep beams was achieved.

Chapter 8: Conclusions and Recommendations

8.1 Introduction

In this thesis, the potential use of NSM-CFRP reinforcement as a strengthening solution around regions of discontinuity in RC deep beams was investigated. All the objectives of this thesis were met throughout the following:

- The STM approach was employed to design three different NSM-CFRP strengthening schemes around the discontinuity regions.

- To examine the effectiveness of the proposed strengthening methodology, laboratory tests were conducted on eight RC deep beam specimens. Two specimens were not strengthened to serve as control beams; one was solid and the other one had an opening in each shear span. The remaining six specimens were strengthened with different NSM-CFRP strengthening schemes around the regions of discontinuity.

- Numerical FE models were developed to predict the nonlinear behavior of the tested specimens. A comprehensive sensitivity analysis was conducted to examine the effect of using different mesh sizes and concrete constitutive laws on the numerical predictions.

- Laboratory test results were compared to predictions of the STM and the FE models to examine their accuracy and validity.

8.2 Limitations of the Current Study

Findings of the present study are limited to the specimens' configurations of adopted in this study such as dimensions, reinforcement ratio, and properties of the used materials. Any variation in the size of specimen, arrangement and amount of NSM-CFRP reinforcement, or loading condition might result in changing the structural behavior of the deep beams. However, the FE models developed in this study were capable of predicting the structural response of the tested specimens with good accuracy. As such, they can be used as a tool in practical applications to predict nonlinear structural behavior of similar RC deep beams with different configurations and strengthening schemes.

8.3 Conclusions

The structural behavior of RC deep beam specimens strengthened with NSM-CFRP reinforcement around regions of discontinuities was studied, experimentally, analytically, and numerically. Conclusions of the work are summarized below:

- Installation of a square opening with $h_o/h = 0.2$ in the shear spans of a deep beam resulted in a 40% reduction in the load capacity.

- The NSM-CFRP strengthening solutions developed in the present study fully restored the original load capacity of the tested specimens, except two beams, where only 93% and 94% of the capacity was restored.

- The solid specimen exhibited a shear-compression mode of failure. The unstrengthened specimen with opening exhibited a diagonal tension mode of

failure. The NSM-CFRP strengthening changed the mode of failure from a diagonal tension to a diagonal splitting or a strut crushing.

- STM I and STM II with a single inclined tie in each shear span crossing either the bottom or top chords were more efficient than STM III having two inclined ties in each shear span (one in the top chord and one in the bottom chord). Doubling the amount of the NSM-CFRP reinforcements increased the capacity of the STM I and STM III specimens by 23% and 10%, respectively. For the STM II specimens having a tie in the top chord, doubling the amount of CFRP did not provide any additional strength gain, possibly because of the mode of failure that was governed by a diagonal splitting of the bottom chord.

- The STM predictions based on provisions of the ACI 318-14 [1] were realistic and accurate. The predicted-to-measured strength ratio based on provisions of the ACI 318-14 [1] was on average 1.01 with a minimum of 0.89 and a maximum of 1.12. The standard deviation was 0.09 and the coefficient of variation was 0.09. Nevertheless, there were discrepancies between the failure mode predicted by the STM and those observed experimentally.

- The STM predictions based on provisions of the CSA S806 [5] were conservative except for the solid deep beam where the predicted strength was 31% higher than that recorded experimentally. The predicted-to-measured strength ratio was on average 0.71 with a minimum of 0.41 and a maximum of 1.31. The standard deviation was 0.29 and the coefficient of variation was 0.41. To obtain realistic STM solutions, it is recommended to minimize the

number of ties in the shear spans and avoid using small angles between a strut and adjoining ties.

- Predictions of the FE model were sensitive to the mesh size and the concrete material constitutive law adopted in the analysis. The accuracy of the numerical analysis improved when the smallest mesh size of 15 mm was adopted. The use of a "user-defined" concrete material constitutive law rather than a "default" concrete constitutive law provided more accurate numerical results.

- The inclusion of a bond-slip law for the NSM-CFRP shear reinforcement resulted in no or up to a 5% reduction in the load capacity. As such, the assumption of a perfect bond between the CFRP and concrete is valid for numerical modeling of RC elements strengthened with NSM-CFRP reinforcement.

- The ratio of the load capacity predicted numerically to that obtained from the tests was on average 0.97. The standard deviation and the coefficient of variation were 0.12. The FE models were capable of predicting the nonlinear deflection response, strains, and failure modes of the tested specimens with good accuracy.

8.4 Recommendations for Future Studies

The current research work provided new knowledge on the behavior of RC deep beams strengthened with NSM-CFRP composites around regions of discontinuity. The followings are recommendations for future research work related to this topic:

- Study the behavior of RC deep beams strengthened with fabric-reinforced cementitious matrix (FRCM).

- Investigate the use of alternative strengthening solutions incorporating the use sustainable materials such as geopolymers and/or recycled aggregates.

- Carry out a parametric study using the developed FE models to investigate the effect of a wider range of parameters such as concrete compressive strength, size, and location of the opening, and shear span-to-depth ratio (a/h).

- Investigate the performance of continuous RC deep beams with discontinuity regions in the shear spans strengthened by NSM-CFRP reinforcement.

References

[1] ACI Committee 318, *Building Code Requirements for Structural Concrete (ACI 318-14)*. Farmington Hills, MI: American Concrete Institute, 2014.

[2] Z. Zhang, C.-T. T. Hsu, and J. Moren, "Shear strengthening of reinforced concrete deep beams using carbon fiber reinforced polymer laminates," *J. Compos. Constr.*, vol. 8, no. 5, pp. 403–414, 2004.

[3] K. A. Mohamed, "Performance and strut efficiency factor of concrete deep beams reinforced with GFRP bars," PhD dissertation, Université de Sherbrooke, 2015.

[4] J. Schlaich, K. Schäfer, and M. Jennewein, "Toward a consistent design of structural concrete," *PCI J.*, vol. 32, no. 3, pp. 74–150, 1987.

[5] Canadian Standards Association, *Design and construction of building structures with fibre-reinforced polymers (CSA S806)*. Mississauga, Ontario, Canada: Canadian Standards Association, 2012.

[6] Q. Hussain and A. Pimanmas, "Shear strengthening of RC deep beams with sprayed fibre-reinforced polymer composites (SFRP) and anchoring systems: part 1. Experimental study," *Eur. J. Environ. Civ. Eng.*, vol. 20, no. 1, pp. 79–107, 2016.

[7] W. Li and C. K. Leung, "Effect of shear span-depth ratio on mechanical performance of RC beams strengthened in shear with U-wrapping FRP strips," *Compos. Struct.*, vol. 177, pp. 141–157, 2017.

[8] B. H. Osman, E. Wu, B. Ji, and S. S. Abdulhameed, "Repair of pre-cracked reinforced concrete (RC) Beams with openings strengthened using FRP sheets under sustained load," *Int. J. Concr. Struct. Mater.*, vol. 11, no. 1, pp. 171–183, 2017.

[9] A. Godat and O. Chaallal, "Strut-and-tie method for externally bonded FRP shear-strengthened large-scale RC beams," *Compos. Struct.*, vol. 99, pp. 327–338, 2013.

[10] J. A. Barros and S. J. Dias, "Near surface mounted CFRP laminates for shear strengthening of concrete beams," *Cem. Concr. Compos.*, vol. 28, no. 3, pp. 276–292, 2006.

[11] M. A. Mansur, K.-H. Tan, and W. Wei, "Effects of creating an opening in existing beams," *Struct. J.*, vol. 96, no. 6, pp. 899–905, 1999.

[12] M. A. Mansur and K.-H. Tan, *Concrete beams with openings: Analysis and design*, vol. 20. CRC Press, 1999.

[13] H. A. Abdalla, A. M. Torkey, H. A. Haggag, and A. F. Abu-Amira, "Design against cracking at openings in reinforced concrete beams strengthened with composite sheets," *Compos. Struct.*, vol. 60, no. 2, pp. 197–204, 2003.

[14] F. K. Kong, *Reinforced concrete deep beams*. CRC Press, 2006.

[15] K.-H. Yang, H.-C. Eun, and H.-S. Chung, "The influence of web openings on the structural behavior of reinforced high-strength concrete deep beams," *Eng. Struct.*, vol. 28, no. 13, pp. 1825–1834, 2006.

[16] T. El Maaddawy and S. Sherif, "FRP composites for shear strengthening of reinforced concrete deep beams with openings," *Compos. Struct.*, vol. 89, no. 1, pp. 60–69, 2009.

[17] A. Pimanmas, "Strengthening R/C beams with opening by externally installed FRP rods: Behavior and analysis," *Compos. Struct.*, vol. 92, no. 8, pp. 1957–1976, 2010.

[18] S. C. Chin, N. Shafiq, and M. F. Nuruddin, "Strengthening of RC beams containing large opening at flexure with CFRP Laminates," *World Acad. Sci. Technol.*, vol. 60, pp. 12–25, 2011.

[19] G. Campione and G. Minafò, "Behaviour of concrete deep beams with openings and low shear span-to-depth ratio," *Eng. Struct.*, vol. 41, pp. 294–306, 2012.

[20] M. R. Islam, M. A. Mansur, and M. Maalej, "Shear strengthening of RC deep beams using externally bonded FRP systems," *Cem. Concr. Compos.*, vol. 27, no. 3, pp. 413–420, 2005.

[21] A. Bousselham and O. Chaallal, "Effect of transverse steel and shear span on the performance of RC beams strengthened in shear with CFRP," *Compos. Part B Eng.*, vol. 37, no. 1, pp. 37–46, 2006.

[22] H. K. Lee, S. H. Cheong, S. K. Ha, and C. G. Lee, "Behavior and performance of RC T-section deep beams externally strengthened in shear with CFRP sheets," *Compos. Struct.*, vol. 93, no. 2, pp. 911–922, 2011.

[23] M. Panjehpour, H. K. Chai, and Y. L. Voo, "Strut deformation in CFRP-strengthened reinforced concrete deep beams," *Sci. World J.*, vol. 2014, 2014.

[24] W. Li and C. K. Leung, "Shear Span–Depth Ratio Effect on Behavior of RC Beam Shear Strengthened with Full-Wrapping FRP Strip," *J. Compos. Constr.*, vol. 20, no. 3, p. 04015067, 2015.

[25] T. El-Maaddawy and B. El-Ariss, "Behavior of concrete beams with short shear span and web opening strengthened in shear with CFRP composites," *J. Compos. Constr.*, vol. 16, no. 1, pp. 47–59, 2012.

[26] S. Vuggumudi, "Experimental study on shear strengthening of RC T-beams with web openings using FRP composites," PhD dissertation, 2013.

[27] A. Ahmed A, S. Naganathan, K. Nasharuddin, and M. M. Fayyadh, "Repair effectiveness of CFRP and steel plates in RC beams with web opening: effect of plate thickness," *IJCE*, vol. 13, no. 2, pp. 234–244, Jun. 2015.

[28] S. M. Allam, "Strengthening of RC beams with large openings in the shear zone," *Alex. Eng. J.*, vol. 44, no. 1, pp. 59–78, 2005.

[29] S. Mondal, J. N. Bandyapadhya, and C. P. Gautam, "Strengthening and rehabilitation of reinforced concrete beams with opening," *Int. J. Civ. Struct. Eng.*, vol. 2, no. 1, p. 359–369, 2011.

[30] R. Diggikar, S. Mangalgi, and R. Harsoor, "Behavior of RCC Beam with Rectangular opening Strengthened by CFRP and GFRP sheets," in *International conference on recent innovations in civil engineering*, pp. 25–27, 2013.

[31] K. Fawzy, "Strengthening of Opening RC Beams in Shear Using Bonded External Reinforcements," *Int. J. Eng. Sci. Innov. Technol. IJESIT Vol.*, vol. 4, pp. 11–23, 2015.

[32] W. Ritter, "Die Bauweise Hennebique," *Schweiz. Bauztg.*, vol. 33, no. 7, pp. 59–61, 1899.

[33] E. Mörsch and E. P. Goodrich, *Concrete-steel Construction:(Der Eisenbetonbau)*. Engineering News Publishing Company, 1910.

[34] J. Schlaich and K. Schafer, "Design and detailing of structural concrete using strut-and-tie models," *Struct. Eng.*, vol. 69, no. 6, pp. 113–125, 1991.

[35] D. Kuchma, S. Yindeesuk, T. Nagle, J. Hart, and H. H. Lee, "Experimental validation of strut-and-tie method for complex regions," *ACI Struct. J.*, vol. 105, no. 5, p. 578, 2008.

[36] M. T. Ley, K. A. Riding, S. Bae, and J. E. Breen, "Experimental verification of strut-and-tie model design method," *ACI Struct. J.*, vol. 104, no. 6, pp. 749–755, 2007.

[37] ACI Committee 440, "Guide for the Design and Construction of Externally Bonded FRP Systems for Strengthening Concrete Structures," American Concrete Institute, Framington Hills, Michigan, Report No. 440 2R-08, 2008.

[38] T. Lobsang, "Assessment of Building Code Provisions and Numerical Models for Predicting the Response of Deep Reinforced Concrete Beams with an Opening," PhD dissertation, Tufts University, 2017.

[39] S. C. Chin, N. Shafiq, and M. F. Nuruddin, "Strengthening of RC beams with large openings in shear by CFRP laminates: 2D nonlinear FE analysis," *World Acad. Sci. Eng. Technol. Int. J. Civ. Environ. Struct. Constr. Archit. Eng.*, vol. 6, no. 2, pp. 153–158, 2012.

[40] S. C. Chin, N. Shafiq, M. F. Nuruddin, and S. A. Farhan, "Strengthening of RC beams with large openings in shear by CFRP laminates: Test results," in *International Conference on Civil, Offshore and Environmental Engineering*, 2012.

[41] R. A. Hawileh, T. A. El-Maaddawy, and M. Z. Naser, "Nonlinear finite element modeling of concrete deep beams with openings strengthened with externally-bonded composites," *Mater. Des.*, vol. 42, pp. 378–387, 2012.

[42] A. Muttoni, J. Schwartz, and B. Thürlimann, *Design of concrete structures with stress fields*. Springer Science & Business Media, 1997.

[43] M. F. Andermatt and A. S. Lubell, "Concrete deep beams reinforced with internal FRP," 2010.

[44] Q. Q. Liang, Y. M. Xie, and G. P. Steven, "Topology optimization of strut-and-tie models in reinforced concrete structures using an evolutionary procedure," PhD dissertation, American Concrete Institute, 2000.

[45] D. B. Garber, J. M. Gallardo, G. D. Huaco, V. A. Samaras, and J. E. Breen, "Experimental evaluation of strut-and-tie model of indeterminate deep beam," *ACI Struct. J.*, vol. 111, no. 4, pp. 873–880, 2014.

[46] B. S. Chen, M. J. Hagenberger, and J. E. Breen, "Evaluation of strut-and-tie modeling applied to dapped beam with opening," *Struct. J.*, vol. 99, no. 4, pp. 445–450, 2002.

[47] Červenka Consulting s.r.o., *ATENA [Computer software]*. Prague, Czech Republic.

[48] P. Menetrey and K. J. Willam, "Triaxial failure criterion for concrete and its generalization," *Struct. J.*, vol. 92, no. 3, pp. 311–318, 1995.

[49] J. G. van Mier, "Multiaxial strain-softening of concrete," *Mater. Struct.*, vol. 19, no. 3, pp. 190–200, 1986.

[50] F. J. Vecchio and M. P. Collins, "The modified compression-field theory for reinforced concrete elements subjected to shear.," *ACI J*, vol. 83, no. 2, pp. 219–231, 1986.

[51] T. Dyngeland, "Behaviour of reinforced concrete panels," PhD dissertation, Norway: Trondheim University, 1989.

[52] A. H. Nilson, D. Darwin, and C. W. Dolan, *"Design of Concrete Structures "[14]^ th edition in SI units*. McGraw Hill, ISBN-13, 2010.

[53] F. Ceroni, M. Pecce, A. Bilotta, and E. Nigro, "Bond behavior of FRP NSM systems in concrete elements," *Compos. Part B Eng.*, vol. 43, no. 2, pp. 99–109, 2012.

[54] A. M. Ibrahim and M. S. Mahmood, "Finite element modeling of reinforced concrete beams strengthened with FRP laminates," *Eur. J. Sci. Res.*, vol. 30, no. 4, pp. 526–541, 2009.

[55] Y. T. Obaidat, S. Heyden, and O. Dahlblom, "The effect of CFRP and CFRP/concrete interface models when modelling retrofitted RC beams with FEM," *Compos. Struct.*, vol. 92, no. 6, pp. 1391–1398, 2010.

List of Publications

Moustafa Mansour, and Tamer El-Maaddawy. "Development of Numerical Models for Deep Beams with Discontinuity Regions Strengthened by NSM-CFRP." In SMAR 2019–Fifth International Conference on Smart Monitoring, Assessment and Rehabilitation of Civil Structures, 2019

Appendix
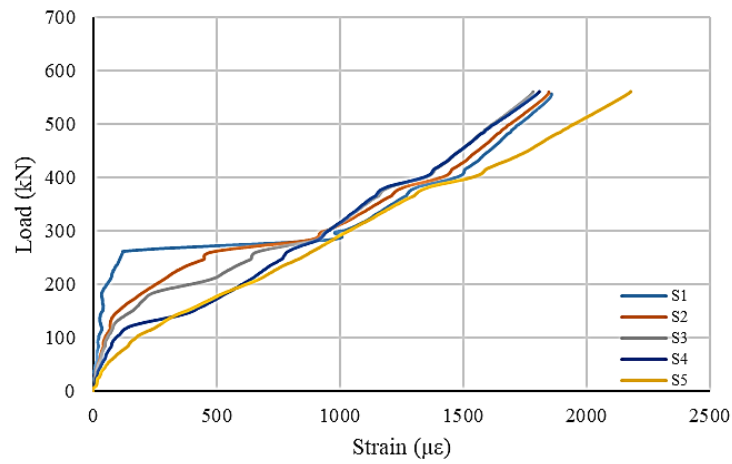
Figure 1: Tensile steel strain response for the solid specimen
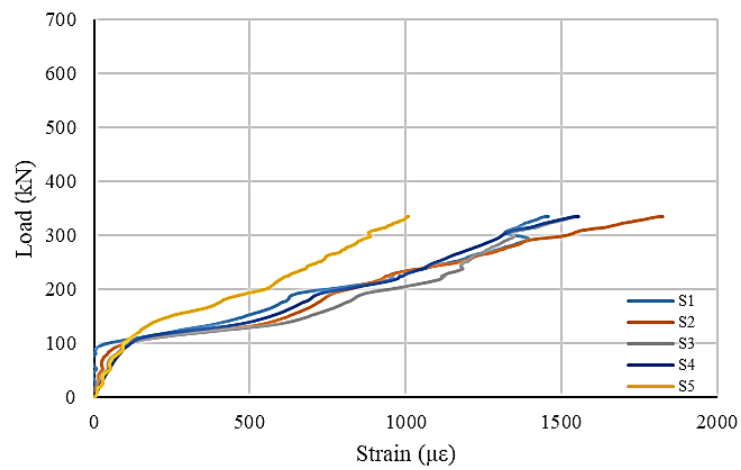
Figure 2: Tensile steel strain response for specimen D-NS
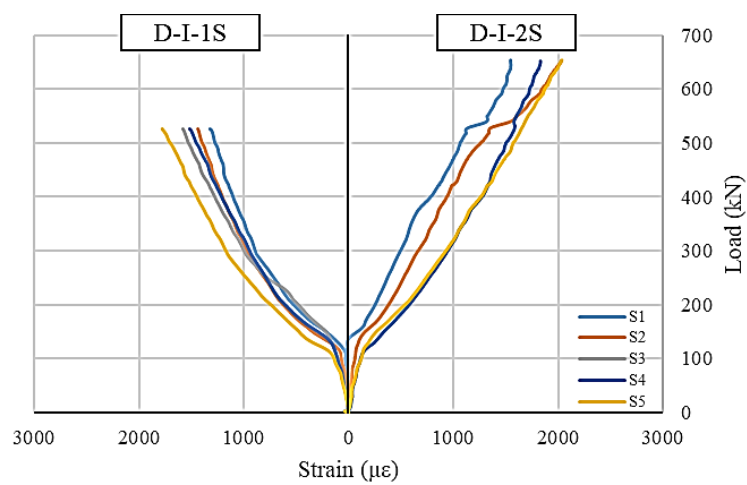
Figure 3: Tensile steel strain response for STM I specimens
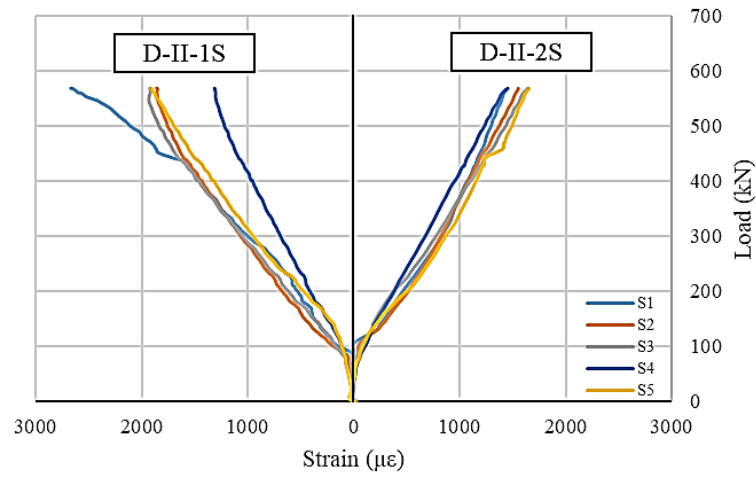
Figure 4: Tensile steel strain response for STM II specimens
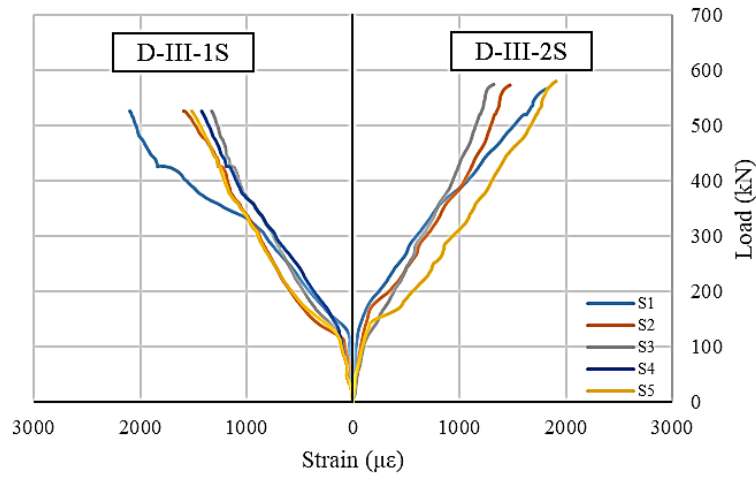
Figure 5: Tensile steel strain response for STM III specimens
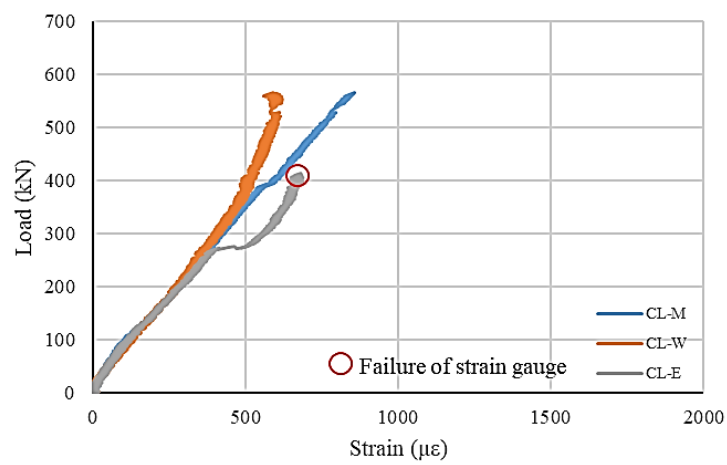
Figure 6: Load-longitudinal concrete strain for the solid specimen
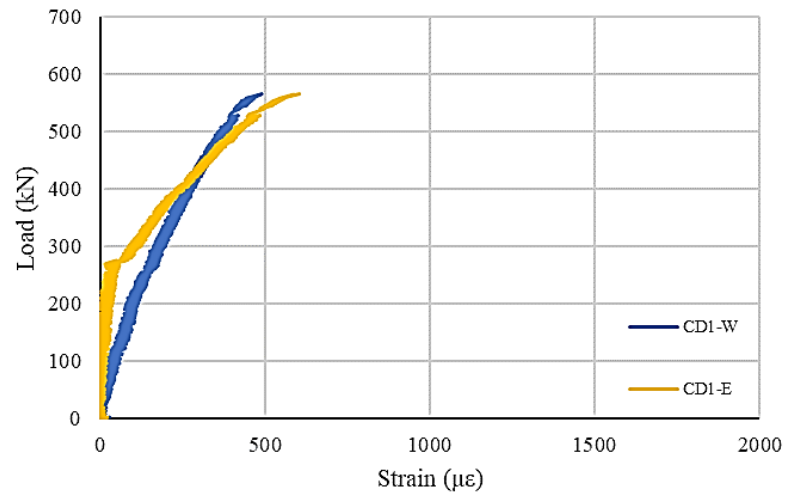
Figure 7: Load-diagonal concrete strain for the solid specimen
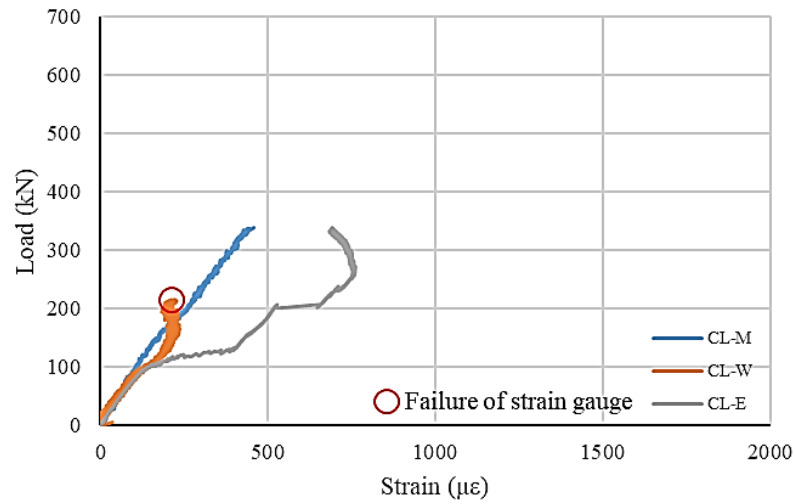
Figure 8: Load-longitudinal concrete strain for specimen D-NS
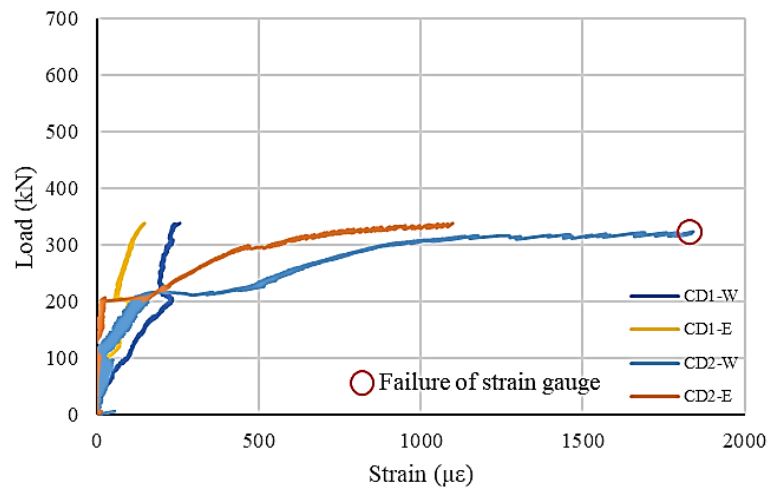
Figure 9: Load-diagonal concrete strain for specimen D-NS
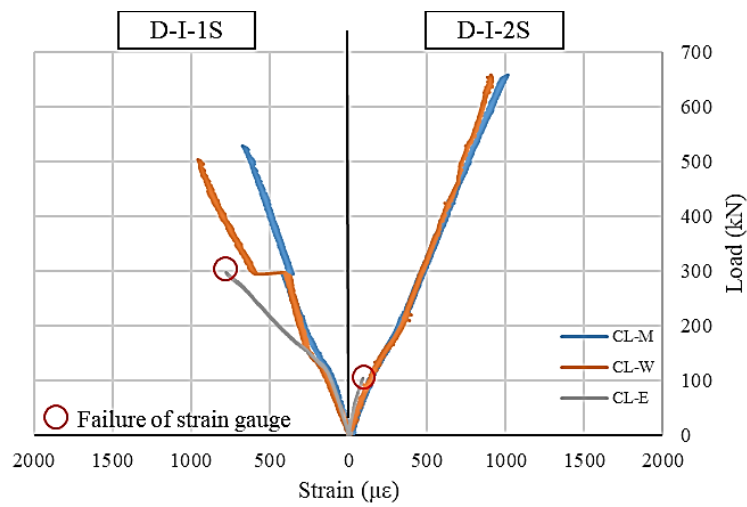
Figure 10: Load-longitudinal concrete strain for STM I specimens
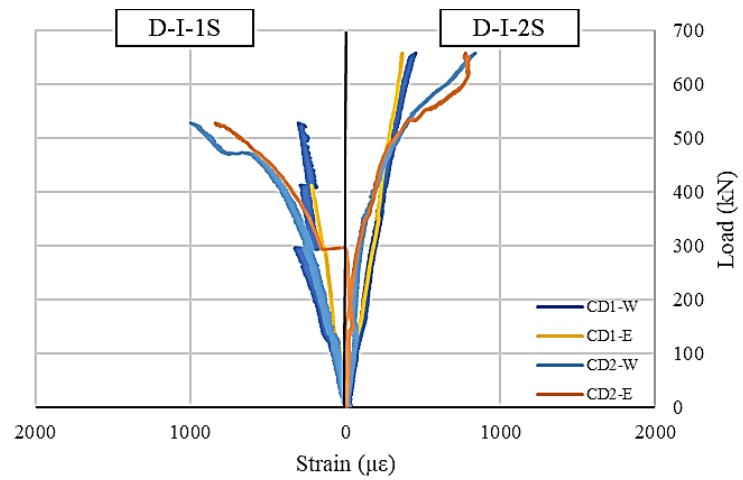
Figure 11: Load-diagonal concrete strain for STM I specimens
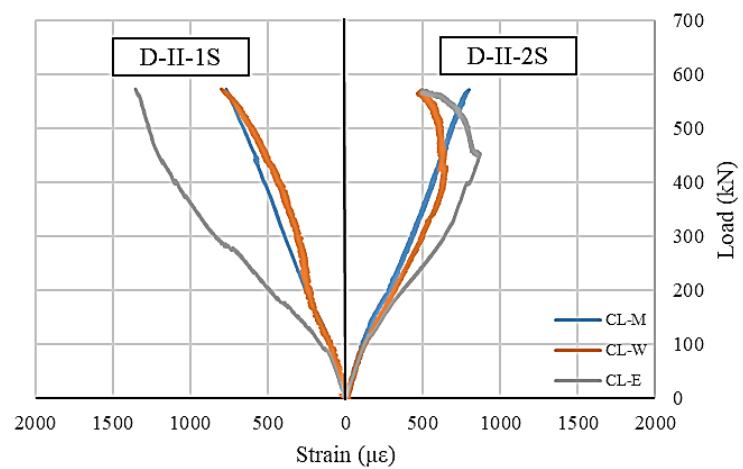
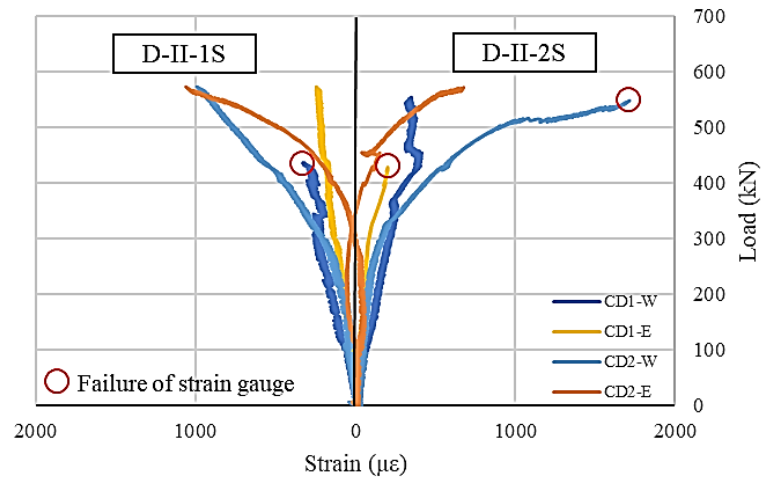Figure 12: Load-longitudinal concrete strain for STM II specimens

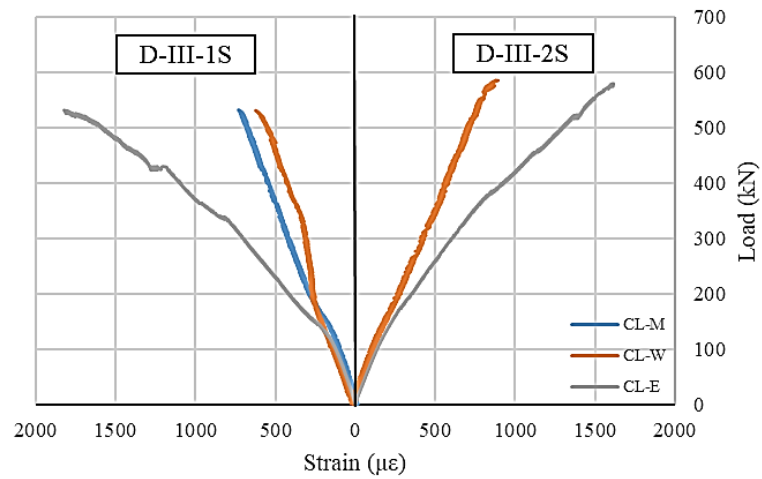Figure 13: Load-diagonal concrete strain for STM II specimens
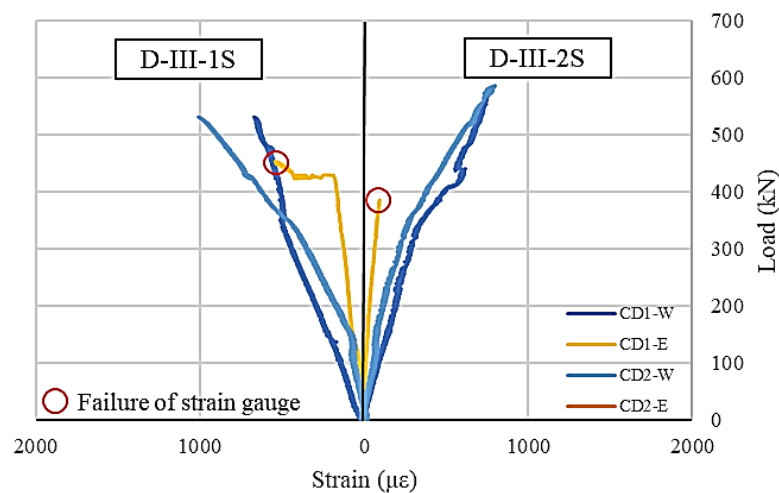

Figure 14: Load-longitudinal concrete strain for STM III specimens

Figure 15: Load-diagonal concrete strain for STM III specimens